UNIVERSITY OF SOUTHAMPTON

Development and Characterization of a Fibre Laser Driven High-Harmonic Source

James Steven Feehan

A thesis submitted for the degree of
Doctor of Philosophy

Faculty of Physical Sciences and Engineering
Optoelectronics Research Centre

February 2016

Declaration of Authorship

I, James Feehan, declare that this thesis entitled 'Development and Characterization of a Fibre Laser Driven High-Harmonic Source' and the work presented in the thesis are my own. I confirm that:

- This work was done wholly or mainly while in candidature for a research degree at the University of Southampton.
- Where any part of this report has previously been submitted for a degree or any other qualification at the University of Southampton or any other institution, this has been clearly stated.
- Where I have consulted the published work of others, this is always clearly attributed.
- Where I have quoted from the work of others, the source is always given. With the exception of such quotations, this report is entirely my own work.
- I have acknowledged all main sources of help.
- Where the report is based on work done by myself jointly with others, I have made clear exactly what was done by others and what I have contributed myself.

Signed: _____

Date: _____

UNIVERSITY OF SOUTHAMPTON

ABSTRACT

FACULTY OF PHYSICAL SCIENCES AND ENGINEERING
OPTOELECTRONICS RESEARCH CENTRE

Doctor of Philosphy

DEVELOPMENT AND CHARACTERIZATION OF A FIBRE LASER DRIVEN HIGH-HARMONIC SOURCE

James Steven Feehan

Table-top high-harmonic sources of extreme ultraviolet (XUV) light are very attractive for applications in coherent diffractive imaging, spectroscopy, and lithography. When compared with synchrotrons and free electron lasers they have greatly reduced size and cost, so beam time would be more readily available to users. Increasing the repetition rate of table-top XUV sources is of interest as it enables faster data acquisition, but this cannot be achieved easily using traditional solid state sources, which require cryogenic cooling for average powers beyond ∼5 W. The demonstrated ability of fibre chirped-pulse amplification (CPA) systems for average power and repetition rate scaling enabled by their inherent thermal stability and readily available, low-cost pump lasers will allow high average power high-harmonic generation systems to become widely available. A prototype fibre CPA system was developed by a previous student at the Optoelectronics Research Centre, and was subsequently demonstrated as a high-harmonic source. However, the system could not be power scaled beyond ∼1 W because of a mismatch between the seed wavelength (1055 nm) and gain peak of the final amplifier (1040 nm). This thesis reports the development of a new, power scalable version with excellent stability due to a reduction in operating wavelength, an optimized amplification chain with grating stabilized pump diodes, and a realigned bulk stretcher and compressor. The system is shown to be capable of state of the art XUV generation efficiency, improving on previously reported values for equivalent systems by a factor of two.

A new seed laser was required for the upgraded fibre CPA system, and during its development a novel multi-wavelength modelocking state was observed. New vectorial simulations of the cavity dynamics definitively identify the cause of this modelocking state and represent the first detailed theoretical description of the onset of multi-wavelength cavity dynamics in breathing pulse Yb-fibre lasers operated below the threshold for multi-pulsing. A novel XUV characterization method was also developed by extending a spatially resolved spectrometry technique to include radius of curvature measurements for full spatial XUV beam profiling from a single exposure. The method was used with the fibre CPA system, allowing for the spatial properties of a fibre laser high-harmonic source to be measured for the first time.

A more exploratory, unrelated supercontinuum experiment was also performed, initially to exploit optical wavebreaking of picosecond pulses in all-normal dispersion photonic crystal fibre to generate octave-spanning coherent spectra. Unexpectedly, cascaded Raman scattering was observed for the first time under these conditions. An experimental and numerical investigation of the coherence properties of Raman-dominated supercontinuum in the normal dispersion regime was performed, and the mechanism causing supercontinua to become incoherent is conclusively identified for this dispersion regime.

Acknowledgements

I would like to thank my supervisors Jonathan Price and Bill Brocklesby for their patience, enthusiasm, help and support throughout my Ph.D., for involving me in the ICAN meetings, organising the trip to Ankara, and for excellent advice about tea, coffee, and guitars.

I would also like to thank David Richardson, Jeremy Frey, and Shaiful Alam for cheerful advice and support during the project, as well as Alexander Heidt for involving me in the supercontinuum work, and for pointing me in the right direction whenever I had a question about nonlinear optics simulations. I am grateful to Russell Minns for involving me in the early stages of his project. I thank Phillip Gorman for letting me borrow lab equipment for the ANDi supercontinuum experiments, Peter Horak for friendly advice on simulations, Robin Head for help with FROG measurements, and Dr. Tom Bradley and Dr. Marco Petrovich for measuring the ANDi fibre dispersion profile. I am also grateful to Simon Butler, Nick Gilbert, and Jamie Cook for machining parts for the lab, and Trevor Austin for help with electrical equipment.

I am also very grateful to the following people who worked at Bilkent University between 3–4/2013 for their hospitality, help in the lab, and for giving me a tour of Ankara: F. Ömer Ilday, Andrey Rybak, Ihor Pavlov, Parviz Elahi, Hamit Kalaycıoğlu, Daniel Press, Burak Eldeniz.

I thank past and present students of the Ultrafast X-Ray and Pulsed Fibre Lasers groups: Tom Butcher, Patrick Anderson, Aaron Parsons, Richard Chapman, Hannah Watts, Pete Baksh, Michal Odstrčil, Simon Teh (especially for all the help with tapering and endcapping), Zhihong Li, Ho Yin Chan, Lin Xu, Martin Berendt, Yongmin Jung, and Richard Lewis. I was made to feel very welcome when I first started, and I am grateful to the past members for answering all of my questions, and to the newer members for asking the same questions a few years later and making me realize which bits of information I had actually taken on board. Above all, I thank these people for their support throughout the Ph.D. process, and for being great company. For the same reasons I am also grateful to housemates Dave Wu and Chris Esprey, as well as Peter Shardlow, Jaclyn Chan, and Edgar Wright for the fibre processing tutorials and Tring beer, chillies, and programming advice, respectively. I also thank Jae Daniel, Matt Eckold, Matthias Feinäugle, and Victor Rancaño. Although each provided help with programming, experiments, or both at one point or another, its the friendly – and occasionally revolutionary – office atmosphere that I will remember most.

Most of all I would like to thank Clare Rumsey, Tonie Bower, Peter Gurney, Danielle Feehan and Shirley Bower for their unconditional support, encouragement, and care, as well as for occasionally dragging me out of the thesis cave for visits. I would not have been able to finish the past four years' worth of work without them.

Contents

List of Figures

Abbreviations

ANDi	All-Normal Dispersion
AOM	Acousto-Optic Modulator
ASE	Amplified Spontaneous Emission
ASM	Angular Spectrum Method
BNC	Bayonet Neill-Concelman
CCD	Charge-Coupled Device
CFBG	Chirped Fibre Bragg Grating
CPA	Chirped-Pulse Amplification
CQE	Conservation Quantity Error
DC	Double Clad
DDL	Dispersive Delay Line
DFT	Dispersive Fourier Transform
DM	Dichroic Mirror
EOM	Eletro-Optic Modulator
FCPA	Fibre Chirped-Pulse Amplification
FROG	Frequency Resolved Optical Gating
FWHM	Full Width at Half Maximum
GDD	Group Delay Dispersion
GNLSE	Generalized Nonlinear Schrödinger Equation
GVM	Group Velocity Mismatch
HHG	High-Harmonic Generation
HR	High Reflector
HWP	Half Wave Plate
LMA	Large Mode Area
MFD	Mode Field Diameter
MI	Modulation Instability
MOPA	Master Oscillator Power Amplifier
NA	Numerical Aperture
NPE	Nonlinear Polarization Evolution
ORC	Optoelectronics Research Centre
OSNR	Optical Signal to Noise Ratio
PBS	Polarizing Beam Splitter
PCF	Photonic Crystal Fibre
PICASO	Phase and Intensity from Cross Correlation And Spectrum Only
PM	Polarization Maintaining
QWP	Quarter Wave Plate
RF	Radio Frequency
RK4IP	Runge-Kutta Fourth-Order Interaction Picture
RMS	Root Mean Square

SCG	Supercontinuum Generation
SHG	Second Harmonic Generation
SPM	Self-Phase Modulation
SRS	Stimulated Raman Scattering
SS	Self Steepening
SSFM	Split-Step Fourier Method
TDSE	Time-Dependent Schrödinger Equation
TEM	Transmission Electron Microscopy
UFOLAB	Ultrafast Optics and Lasers Laboratory
WDM	Wavelength Division Multiplexer
XPM	Cross-Phase Modulation
XUV	Extreme Ultraviolet
YDF	Ytterbium-Doped Fibre

Chapter 1

Introduction

The observation of nonlinear electromagnetic responses from optical materials swiftly followed the invention of the laser as, for the first time, intensities which induce an anharmonic electronic response could be reached [1, 2]. Since then a wide range of nonlinear effects have been identified, with the efficient generation of new frequencies being central to research. Motivation for frequency conversion is provided by a number of fields which require coherent light sources at wavelengths which cannot be produced through lasing. Wavelength regions of particular relevance to this thesis work are the extreme ultraviolet (XUV, 10–100 nm) and the soft X-ray (1–10 nm), and have seen applications in fundamental physics and chemistry [3, 4], materials science and optical component manufacture [5, 6, 7], and lensless high resolution imaging [8]. Free electron lasers and synchrotrons have been used for these purposes, but the scale and high cost of such facilities severely limits their availability, and beam time can be difficult to secure. As a result, nonlinear frequency conversion into the XUV using high-harmonic generation (HHG) [9] has been the focus of extensive research with the aim of creating an efficient, cost-effective, and compact table-top source as a widely available alternative.

To generate high harmonics, a laser pulse with visible or infrared wavelength is focussed to an intensity of 10^{14} W/cm^2 in a target medium of, most commonly, a noble gas. The first experimental demonstration of HHG came in the 1980s when technology capable of producing such a high intensity first became available. By focussing a pulsed Nd:YAG laser into an argon gas jet, emission of the 33rd harmonic of 1064 nm (32 nm) was observed by Ferray et al. [9]. Following this discovery, the experimental development of HHG has been focussed on generating shorter wavelengths, increasing the XUV flux, and on attosecond metrology [10, 11, 12]. These developments were made using Ti:Sapphire seed lasers, which have a broad emission spectrum allowing for milli-Joule energy pulses with just 6 fs duration [13]. Many applications of high-harmonic

generation would benefit from an enhanced repetition rate due to the potential for increased flux that this offers but, despite the impressive performance of Ti:Sapphire laser systems, ytterbium-doped fibre lasers, with their near ideal geometry for thermal management and low quantum defect, present an attractive alternative for average power and repetition rate scaling. The development of cladding pumped fibre technology and the availability of low-cost 976 nm diode pump lasers over the past two decades [14] has allowed for continuous wave output powers above a kilowatt from single-mode Yb-doped fibre lasers [15] and peak powers in excess of a gigawatt when used with the CPA architecture [16].

The fibre geometry also allows for high efficiency, as well as average power and repetition rate scaling with diffraction limited beam quality due to the guided mode. The tight mode confinement does, however, mean that nonlinear distortion poses the biggest challenge when developing pulsed fibre laser systems. Self- and cross-phase modulation can cause significant distortion to the pulse phase as it is being amplified which can increase the dispersion mismatch between the CPA stretcher and compressor, leading to pulse break up and severely reduced peak power. Large mode area flexible and rod-type fibres can reduce the peak intensity in the amplifier and hence minimize nonlinear effects, allowing pulses of sub-picosecond duration and energy of order 100 μJ–1 mJ [17, 18] to be generated at repetition rates in excess of 100 kHz. To produce pulse energies above that possible from a single rod-type amplifier, parallel amplifier geometries have also been explored which spatially divide the pulses to seed a tiled parallel array of Yb-doped large mode area amplifiers. The output pulses are then recombined to give a total energy which is much higher than could be achieved with a single fibre. This process is known as coherent combination [19, 20].

Using these techniques it has been possible to generate high harmonics with microwatt average powers [21, 22] which have subsequently been used for real-time XUV coherent diffractive imaging [23]. XUV continua up to the water window have also been observed [24, 25]. It should be noted that these results have required two-stage nonlinear compression to reduce the pulse duration from $\sim$0.8 ps to approximately 30 fs [26].

In spite of the excellent progress, these systems are still predominantly formed using bulk optics, and are therefore susceptible to environmental instability which is not seen with more fully fiberized systems. In addition, transverse modal instability restricts the power scaling of the rod-type amplifiers used to the $\sim$200 W level [27, 28]. As such, research carried out at the Optoelectronics Research Centre (ORC) has focussed on using flexible, single mode fibres to mitigate these instabilities, maintain purely single-mode operation, and simplify the laser architecture to one which may be easily packaged and commercialized.

In previous work a fibre CPA system was developed at the ORC [29, 30]. The system emitted 100 μJ, 300 fs pulses at a repetition rate of 16.7 kHz, and was capable of

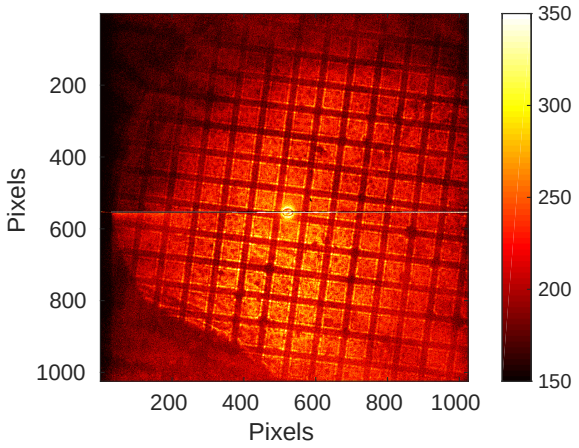

FIGURE 1.1: Near-field diffraction pattern created by XUV generated by a fibre CPA system after passing through a wire mesh, recorded as part of a preliminary characterization experiment at the start of this thesis work. The colourmap indicates CCD pixel counts on a linear scale.

producing XUV radiation via high-harmonic generation [31], as shown by the near-field scattering pattern produced by a wire mesh placed in the XUV beam in figure 1.1 during a preliminary characterization experiment performed in the first few months of this project. This system, however, was unsuitable for average power and repetition rate scaling at high pulse energy due to a large mismatch between the operating wavelength of 1055 nm and the gain peak of the final amplifier at approximately 1035–1040 nm. Additionally, instabilities such as self-Q-switching were observed due to insufficient energy extraction from the gain fibre. However, the results showed that the overall architecture was capable of producing a high pulse energy and performed as expected, providing a platform for optimization. In addition, a low pulse energy, high repetition rate variant of the system had been shown to produce >100 W of average power [32], enabled by the dielectric compressor grating which again supported a strategy of continuing to refine the performance level of the system.

This thesis documents the development of this fibre CPA design to operate at 1045 nm, which led to improved system stability, optical signal-to-noise ratio, and XUV flux. The majority of the new system was fiberized and as a result excellent long-term and shot-to-shot stability were demonstrated and diffraction limited beam quality for 100 μJ, 350 fs pulses emitted at a repetition rate of 16.7 kHz was achieved. The system was used to generate XUV via HHG in a xenon-filled gas cell. The average output XUV power of 400 nW corresponds to a state of the art conversion efficiency for both linearly and nonlinearly compressed fibre CPA systems which do not involve the complexity of coherent combination. The XUV was characterized using a newly developed extension to an existing spatially resolved spectrometry technique, and wavelengths down to 27 nm were detected. The characterization technique allowed for the radius of curvature and

spatial intensity distributions of the harmonics generated from a fibre CPA system to be resolved for the first time.

During this work I was also involved in a supercontinuum generation project as I had developed a suitable pump laser for the experiments. Motivated to produce a low-cost octave spanning optical frequency comb for applications in metrology and attosecond pulse generation an amplifier emitting chirped picosecond, broad bandwidth pulses was used as a pump for supercontinuum generation in all-normal dispersion (ANDi) photonic crystal fibre (PCF), with the aim of producing coherent spectral broadening through optical wavebreaking. Unexpectedly, cascaded Raman scattering was observed for the first time in this dispersion regime, and a numerical and experimental investigation into the effect that this process has on the resulting coherence was carried out. The coherence was found to degrade quickly as Raman scattering became the dominant broadening process, and the mechanism through which this occurs is described for the first time in this work.

This thesis is separated into three parts. In part I, chapter 2 the relevant fibre technology, Yb^{3+}-doped silica spectroscopy, and nonlinear fibre optics are introduced before a description of the pulse propagation algorithm used for the nonlinear fibre optics simulations included in this thesis. Chapter 3 of this part documents the modelocked Yb-doped fibre oscillator built as part of this project for seeding the new fibre CPA system, which is described in part I, chapter 4. Part II starts with an introduction to high-harmonic generation in chapter 5, which is followed by a description of the single exposure characterization technique in part II, chapter 6. A proof-of-principle demonstration of the technique using a capillary high-harmonic source driven by a Ti:Sapphire laser is also described. Part II is finalized in chapter 7, which includes the performance and characterization of the fibre CPA as a high-harmonic source. Part III, chapter 8 documents a separate but related experiment in which cascaded Raman scattering is recorded for the first time in the all-normal dispersion regime. The thesis is then concluded in part IV, chapter 9.

Part I

Fibre CPA development

Chapter 2

Theory of pulse propagation in silica optical fibre

The optical fibre propagation theory, technology, and relevant numerical methods for simulating pulse propagation in silica are introduced in this chapter. Section 2.1 describes step-index fibre technology and the condition for single mode operation, as well as the group delay experienced by single mode signals propagating in step-index fibre. Section 2.2 introduces Yb-doped silica fibre as a gain medium, starting with the spectroscopy of Yb^{3+} ions in an aluminosilicate host in subsection 2.2.1, then outlining the Yb-doped fibre designs used for high peak and average power applications in subsection 2.2.2. Section 2.3 introduces nonlinearity, dispersion, and the generalized nonlinear time-dependent Schrödinger equation (GNLSE). Section 2.4 introduces the Runge-Kutta Fourth-Order Interaction Picture (RK4IP) and Conservation Quantity Error (CQE) methods used for simulating pulse propagation, and describes how quantum noise was included in these simulations. The chapter is concluded with a summary in section 2.5.

2.1 Single mode step-index optical fibre

Generally, step-index optical fibre is constructed of a core with refractive index n_{core} surrounded by a cladding with refractive index $n_{\text{clad}} < n_{\text{core}}$, with a discontinuity in refractive index at the boundary between the two. Under single mode operation, step-index fibre supports only one transverse propagation mode per polarization state for a given wavelength. This is the case under the condition that the V-number (or normalized frequency parameter), given in equation 2.1, has a value which is less than 2.405 [33, 34]

$$V = \frac{2\pi}{\lambda} a (n_{\text{core}}^2 - n_{\text{clad}}^2)^{\frac{1}{2}} \tag{2.1}$$

where λ and a are the wavelength and core radius, respectively. There exists both a short and long wavelength limit to single mode operation. The short wavelength limit defines the point at which the fibre is able to guide more than one transverse mode for a given core radius and refractive index difference between the core and cladding. Conversely, the long wavelength limit defines the point at which the fibre stops guiding due to material absorption or bend-induced loss. The latter is determined by the numerical aperture (NA) of the fibre, which is defined as follows:

$$\mathrm{NA} = \sin(\theta_{\max}) \approx (n_{\mathrm{core}}^2 - n_{\mathrm{clad}}^2)^{\frac{1}{2}} \tag{2.2}$$

Here, $\theta_{\max}$ is the maximum incidence angle measured with respect to the core tangent that will allow for an input optical ray to be guided in the core. Equivalently, the NA may also be defined as the sine of the solid half angle through which a guided optical beam will diverge when emitted from the core to free space. Fibres with a high NA are more resilient against bend loss in general [35, 36]. Standard single mode fibre used at a wavelength of 1 μm (e.g., PM980 or HI1060) have minimum bend radii of approximately 1 cm for NA $\approx$ 0.14. As shown by equation 2.1 the fibre V-number also depends on NA. This has important consequences for maintaining diffraction limited beam quality whilst scaling peak power in pulsed fibre laser systems and will be discussed in subsection 2.2.2.

A broadband optical signal propagating in step-index fibre will also be subject to chromatic dispersion, which may in part be controlled by the fibre parameters represented by the V-number and NA. Under the condition that the difference between the core and cladding refractive indices is small (known as the weakly guiding condition, expressed in equation 2.3), it has been shown [37] that the propagation constant for light guided in optical fibre can be written as shown in equation 2.4.

$$\Delta = \frac{n_{\mathrm{core}} - n_{\mathrm{clad}}}{n_{\mathrm{clad}}} \ll 1 \tag{2.3}$$

$$kn_{\mathrm{clad}} < \beta < kn_{\mathrm{core}} \tag{2.4}$$

where β is the signal propagation constant and k the vacuum wavenumber. Using equation 2.5 simplifies the propagation constant to the form given in equation 2.6.

$$b = \frac{(\beta^2/k^2) - n_{\mathrm{clad}}^2}{n_{\mathrm{core}}^2 - n_{\mathrm{clad}}^2} \tag{2.5}$$

$$0 < b < 1 \tag{2.6}$$

Parameter b is referred to as the normalized propagation constant, and may be used to relate β to n_{clad}, k, and Δ through the following:

$$\beta = n_{\text{clad}} k(b\Delta + 1) \tag{2.7}$$

Taking the derivative of the propagation constant with respect to vacuum wavenumber gives the group index for the signal:

$$n_{\text{group}} = \frac{d\beta}{dk} \tag{2.8}$$

Due to the material dispersion of the silica glass core and the wavelength dependence of the V-number, the group index will also have a wavelength dependence. Multiplying by fibre length, L, and dividing by the speed of light in vacuum, c, the group delay experienced by an optical signal of wavelength λ may be expressed as:

$$\tau_{\text{group}} = \frac{L}{c} n_{\text{group}} \tag{2.9}$$

The group delay shares its wavelength dependence with the group index, and this dependence may be expressed intuitively by assuming that Δ is not wavelength dependent (i.e., that the material dispersion of the core and cladding is equal), and that $k(dn/dk) \ll n$. As shown in Ref. [38], this yields:

$$\tau_{\text{group}} = \frac{L}{c}\left[\frac{d(kn_{\text{core}})}{dk} + n_{\text{core}}\Delta\frac{d(Vb)}{dV}\right] \tag{2.10}$$

The first term in equation 2.10 accounts for the effect of the core material, and the second for the fibre geometry. From this relationship it is clear that Δ and the V-number may determine the group delay as a function of wavelength experienced by a wide bandwidth signal guided in the core of an optical fibre. This relationship is used extensively in the work presented in chapter 8.

2.2 Yb^{3+}-doped fibre

2.2.1 Spectroscopy of Yb^{3+}-doped silica

The Yb^{3+} energy level structure is shown in figure 2.1 [39]. The ground state manifold ($^2F_{7/2}$) has four Stark levels (labels a–d), and the excited state manifold ($^2F_{5/2}$) has three Stark levels (labels e–g), and is separated from the ground state by $\sim 10^4$ cm^{-1}. Due to its simplicity, this structure mitigates detrimental processes such as concentration quenching by energy transfer between ions, and excited state absorption of the pump

and signal light. Additionally, the large energy gap between manifolds prevents non-radiative transitions by multi-phonon emission. Cooperative up-conversion does occur, but is a very weak process and is therefore neglected.

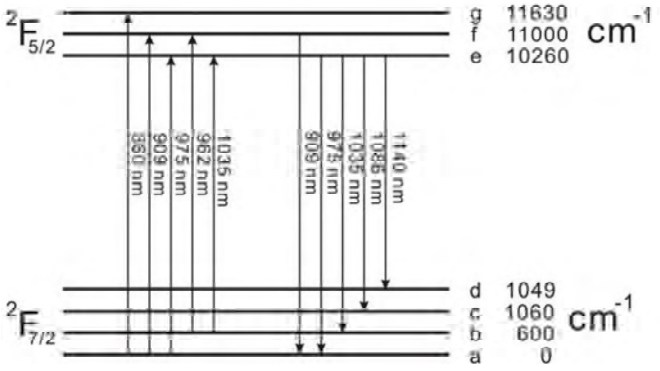

FIGURE 2.1: Yb-doped silica energy level diagram (from [39]).

The sublevels shown in figure 2.1 are not fully resolved in Yb-doped silica fibres. The resulting absorption and emission cross sections, shown in figure 2.2, are therefore broad and lack discrete features [39, 40]. This is due to the strong homogeneous and inhomogeneous broadening mechanisms acting on the Yb^{3+} ions in the silica host, including the effect on linewidth from the uncertainty in decay time (~ 0.8 ms), phonon interactions between the ions and the silica fibre, and the anisotropic structure of fused silica, which has the effect of randomizing the Stark splitting experienced by each ion. Although the host composition has a significant effect on the cross-sections and fluorescence time (reportedly as high as 30% [41, 42]), only aluminosilicate hosts are relevant to the work presented in this thesis.

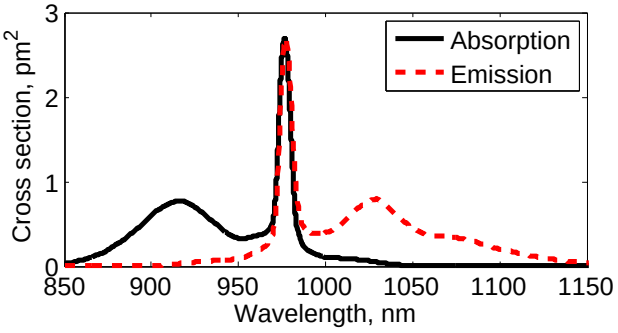

FIGURE 2.2: Absorption and emission cross sections for Yb-doped aluminosilicate glass.

The main features of the Yb-doped aluminosilicate fibre cross-sections are [39]: The strong emission and absorption peaks at 975 nm; the absorption band around 915 nm; the emission band around 1030 nm; the absorption and emission tails starting at 1030 nm and 925 nm, respectively. Due to the high absorption cross sections, shorter fibre lengths may be used by pumping at the 975 nm absorption peak, which also avoids strong ASE

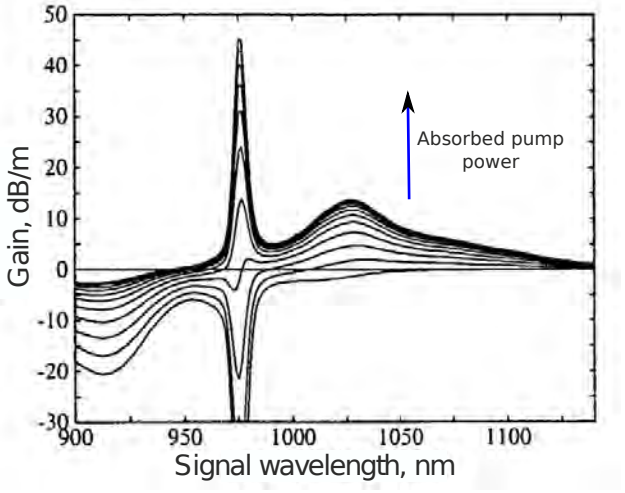

FIGURE 2.3: Simulation showing the gain profile as a function of inversion for a typical Yb-doped fibre amplifier pumped with 910 nm light as the pump power is increased from 0–30 mW in intervals of 3 mW (adapted from [40]).

from the emission peak at the same wavelength. Pumping in the 915 nm band does not share this advantage, and the reduced absorption at this pump wavelength necessitates longer fibre lengths. The broad emission band from 1030–1100 nm corresponds to transitions from level e to levels b–d in figure 2.1, and emission becomes quasi four-level in character at longer wavelengths due to the small thermal populations of the Stark split sublevels.

Transitions in the Yb^{3+} ion spectroscopy may be considered three-level for gain in the 975–1050 nm band. This is demonstrated in figure 2.3, which shows the gain per unit length for a typical Yb-doped fibre amplifier as a function of pump power. For low pump powers there is strong absorption below 1050 nm, meaning that the Yb-doped fibre length must be optimized to avoid loss in an unpumped section. As the operating wavelength is increased, the dynamics tend towards four-level behaviour as absorption becomes weaker. Increasing the fibre length for a given pump power therefore extends the gain peak to longer wavelengths. However, as the emission cross section for shorter wavelengths is significantly larger, short gain fibre lengths and high inversion moves the gain peak closer to 1030 nm. The three-level dynamics also lead to a requirement for high brightness pump diodes and low loss fibres. As these are now commercially available, Yb-doped fibre lasers and amplifiers have become a standard tool for applications which require high average and peak power optical systems with diffraction limited beam quality [15, 16, 43], owing to the low quantum defect ($\sim 10\%$), lack of excited state absorption, broadened emission spectrum, and availability of high power pump diodes at the wavelength of the absorption peaks.

2.2.2 Fibre technology for high peak power applications

While single-mode, single-clad fibres are useful for applications where diffraction limited beam quality and high gain are required, population inversion is usually achieved by propagating the pump light in the core with the signal. Single-mode pump diodes must therefore be used, limiting the available output average power to < 1 W.

The development of double-clad fibre technology [44, 45, 46, 47] allows for high power pump diodes to be used, enabling average power scaling from the Watt level to multiple kilo-Watts [15]. The structure of double-clad fibres is similar to that of the single-mode fibres discussed in section 2.1, with the addition of a reduced-index inner cladding surrounding the single-mode core. The inner cladding has a high NA and usually supports a large number of modes, so that output from multi-mode pump diodes can be coupled efficiently. As the multi-mode pump light propagates in the inner cladding, it passes into and is absorbed by the Yb-doped signal core, allowing for the single-mode signal to be amplified.

As a result of the reduced overlap between the pump light and Yb-doping, double-clad fibres have a relatively low pump absorption per unit length, necessitating longer device lengths. This effect is mitigated in the double-clad fibre amplifiers used in this work by increasing the NA and reducing the diameter of the inner cladding, which results in a greater pump overlap with the Yb-doped signal core without requiring higher pump brightness.

Amplifying pulses with a high peak power requires that nonlinear effects are negated to prevent pulse distortions. Large mode area (LMA) fibres which maintain a single spatial mode may be used for this purpose. Whereas a typical single-mode fibre has a mode area of < 50 μm^2 (MFD of 5–6 μm), LMA fibres can support mode areas up to a few thousands of μm^2 [48, 49], thus reducing the optical intensity in the amplifier by factors of > 10 and increasing the threshold of nonlinear distortion.

There are a number of ways in which the mode area of a fibre may be increased whilst maintaining single-mode operation. The first is to increase the core radius and decrease the NA to maintain $V < 2.405$. However, this decreases the threshold for bend induced loss, until mechanical strain increases the core index which has the effect of compressing the mode to smaller areas. In step-index fibre, the minimum achievable core NA is limited to approximately 0.06 by the error in the concentration of dopants (e.g., germanium) used to control the core refractive index. Solid-core photonic crystal fibres (PCF) allow for lower NA values as the air-clad structure may be adjusted with greater accuracy than chemical doping. Larger mode areas are therefore achieved when using PCF in comparison with step-index fibres, but bend loss [50] and mode compression remain the limiting factors. In order to reduce this constraint, it is possible to use few-moded fibres in a 'quasi-single-mode' configuration. Beam quality close to the diffraction

limit can be achieved this way by exploiting bend loss, which is higher for the higher order modes. Both quasi-single-mode operation of step-index fibres and PCF designs are used in the amplifiers described in this thesis.

In addition to nonlinear pulse distortion, damage to the fiber facets may also occur for high optical intensities. This is avoided by splicing an endcap formed of coreless silica rod to the fibre facets. The mode expands in the silica rod once it has left the fibre core, and the intensity is reduced at the air-silica interface, where the damage threshold is lower with respect to the bulk silica [51, 52]. The endcap facet is then polished, further increasing the damage threshold [52, 53].

2.3 Nonlinearity and dispersion in optical fibre

This section briefly introduces the effects that nonlinearity and chromatic dispersion have on a pulse propagating in a single mode optical fibre. The amorphous structure and low nonlinear refractive index of silica glass [54] mean that only third order nonlinear effects need to be considered, and as such this discussion is limited to self-steepening, self- and cross-phase modulation, and Raman scattering. Due to the broadband optical signals used throughout this work, Brillouin scattering is negligible and is not taken into account.

An electric field polarized along the transverse x-axis of an optical fibre and propagating along a z-axis along the fibre length is given by equation 2.11:

$$\vec{E}(x,y,z,t) = \frac{1}{2}\vec{x}(E(x,y,z,t)e^{i(\beta_0 z-\omega_0 t)} + \text{c.c}) \tag{2.11}$$

Here, $\vec{E}$ is the complex electric field with amplitude profile E, carrier frequency ω_0, and propagation constant β_0. Taking the Fourier transform of this field gives the distribution in the frequency domain:

$$\tilde{E}(x,y,z,\omega) = F(x,y,\omega)\tilde{A}(z,\omega-\omega_0)e^{i\beta_0 z} \tag{2.12}$$

$\tilde{E}$ denotes the Fourier transform of the electric field defined in equation 2.11, F is the transverse mode profile, and $\tilde{A}$ is the complex spectral envelope. The transverse mode profile of the signal in the fibre core determines the optical intensity for a given on axis peak power. As such, an effective mode field area, A_{eff}, is defined in equation 2.13, and is used in determining the strength of the nonlinear response of the fibre material.

$$A_{\text{eff}}(\omega) = \frac{\left(\iint_{-\infty}^{\infty}|F(x,y,\omega)|^2 dxdy\right)^2}{\iint_{-\infty}^{\infty}|F(x,y,\omega)|^4 dxdy} \approx \pi\left(\frac{\text{MFD}}{2}\right)^2 \tag{2.13}$$

Here, MFD denotes the mode field diameter. The time domain representation of the spectral envelope is derived by taking the Fourier transform of $\tilde{A}(z, \omega - \omega_0)$:

$$A(z,t) = \frac{1}{2\pi} \int_{-\infty}^{\infty} \tilde{A}(z, \omega - \omega_0) e^{-i(\omega-\omega_0)t} d\omega \tag{2.14}$$

$A(z,t)$ is normalized such that its square modulus gives the instantaneous power in Watts.

The effect of chromatic dispersion and nonlinearity on the time domain envelope is in general calculated by finding numerical solutions to the following GNLSE:

$$\frac{\partial A(z,T)}{\partial z} = \left(\hat{D} + \hat{N}\right) A(z,T) \tag{2.15}$$

$\hat{D}$ and $\hat{N}$ denote the dispersive and nonlinear operators which act together on envelope $A(z,T)$, and the time axis has been centred about the envelope by a change of variable $T = t - z/v_{\text{group}}$. The fibre loss and dispersion information is included through the linear parameter:

$$L = -\frac{\alpha}{2} - \sum_{n \geq 2}^{\infty} \beta_n \frac{i^{n-1}}{n!} \frac{\partial^n}{\partial T^n} \tag{2.16}$$

which is then used to define the dispersive operator through $\hat{D} = \exp(Ldz/2)$. In equation 2.16, β_n denotes a set of Taylor coefficients which approximate the propagation constant $\beta(\omega)$ for the fibre about the central angular frequency of the signal, ω_0. These have units of s^n/m, and may be measured experimentally [55, 56, 57]. Where the higher order dispersion coefficients are not known, the Taylor expansion may be truncated at the second order, β_2, albeit with reduced accuracy. It is often useful to consider second order dispersion in units of picoseconds of temporal broadening per nanometre of bandwidth and per kilometre of propagation. The dispersion parameter is defined for this purpose as [58]:

$$D(\lambda) = \frac{-2\pi c \beta_2}{\lambda^2} \tag{2.17}$$

Additionally, the length of fibre over which the spectral phase of the optical signal increases by π radians due to chromatic dispersion is of practical interest. This parameter is known as the dispersion length, and is given by equation 2.18.

$$L_D = \frac{T_0^2}{|\beta_2|} \tag{2.18}$$

where T_0 is the duration at the half-width at $1/e$ intensity point [58]. The second order dispersive phase parameter, β_2, is significant in determining the propagation dynamics of envelope $A(z,T)$. The envelope may take the form of dispersive solutions for the normal dispersion regime where $\beta_2 > 0$, or soliton solutions for the anomalous dispersion regime, where $\beta_2 < 0$. All fibres considered in this thesis are normally dispersive

at wavelengths below 1.3 μm, and the anomalous dispersion regime is not considered in further detail.

The nonlinear operator in equation 2.15 approximates both the instantaneous and delayed intensity dependent response of the optical fibre, and may be represented in the time domain as follows:

$$\hat{N} = i\gamma \frac{1}{A_m}\left(1 + \frac{1}{\omega_0}\frac{\partial}{\partial T}\right)\left[(1-f_R)\left(|A_m|^2 + \frac{2}{3}|A_n|^2\right)A_m \right. \\ \left. + f_R A_m \int_0^\infty h_R(\tau)|A_m(z,T-\tau)|^2 d\tau + i\Gamma_R(z,T)A_m\right] \quad (2.19)$$

where $\gamma = (2\pi n_2)/(A_{\text{eff}}\lambda)$ is the nonlinear parameter in units of rad(Wm)$^{-1}$, and scales the nonlinear response according to the nonlinear refractive index, n_2 (2.74×10^{-20} m^2/W for silica around 1 μm [59]), and the effective mode field area.

The Raman fraction, f_R, determines the fraction of the nonlinear material response which is delayed, and has a value of 0.18 for silica [60]. The coefficient $(1-f_R)$ therefore determines the strength of the nonlinear contribution from the instantaneous material response. Self-steepening (SS), self-phase modulation (SPM), and cross-phase modulation (XPM) between orthogonally polarized field components belong to the instantaneous category, and will be discussed first. Both stimulated and spontaneous Raman scattering belong to the delayed category, and will be discussed second.

The term involving the temporal derivative accounts for SS, in which the peak of the envelope travels at a reduced group velocity due to the intensity-dependent increase in refractive index [61]. Following this, SPM is included through the term in $|A_m|^2$ [62], and accounts for the shift in instantaneous frequency experienced by envelope A_m according to the negative gradient of $|A_m|^2$. Similarly, the term in $(2/3)|A_n|^2$ accounts for XPM between orthogonal polarization states, where subscripts m and n indicate the orthogonal polarization components of the complex electric field envelope. This term is responsible for a number of nonlinear effects, including a shift in the instantaneous frequency of envelope A_m according to the negative gradient of $|A_n|^2$, as well as an intensity dependent rotation (or evolution) of the polarization state. The latter has been used to form a fast saturable absorption mechanism for self-start modelocking of fibre lasers [63, 64, 65], and is responsible for the modelocked fibre oscillator dynamics presented in chapter 3.

As with dispersion, it is often useful to calculate the length of fibre over which SPM increases the signal phase by π radians. The so-called nonlinear length is defined as follows:

$$L_N = \frac{1}{\gamma P_0} \quad (2.20)$$

where P_0 is the peak power of the pulse. Similarly, it is frequently useful to calculate the total phase increase from SPM along a fibre length using the B-integral:

$$B = \frac{2\pi}{\lambda} \int_0^L n_2 I(z) dz \tag{2.21}$$

Relations 2.20 and 2.21 are useful for approximating the accumulated nonlinear phase shift in supercontinuum experiments, modelocked fibre oscillators and amplifiers, and are used for analysing the nonlinear dynamics of the modelocked fibre oscillator and fibre CPA system in chapters 3 and 4, respectively.

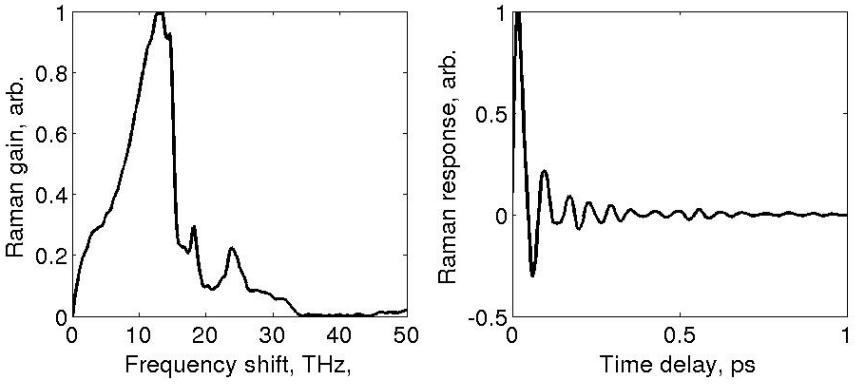

FIGURE 2.4: Left: Raman gain spectrum, $g_R(\Omega)$, and right: Raman response, $h_R(\tau)$, for silica.

The delayed nonlinear response is expressed by the convolution integral in equation 2.19, which accounts for Raman scattering. This effect involves a coupling between incident signal photons and optical phonons in the fibre. Photons may be absorbed by the silica lattice, leading to an unstable virtual excited state. A fraction of the original (pump) photon energy may be retained when the virtual state relaxes spontaneously, leading to an emitted (Stokes) photon with a reduced frequency, and a phonon with energy $\hbar(\omega_{\text{pump}} - \omega_{\text{Stokes}})$. An increase in photon energy is also possible, and occurs when a propagating phonon and pump photon produce a virtual excited state which then decays into a single anti-Stokes photon. However, anti-Stokes radiation is emitted less frequently than Stokes as this process is less favourable.

Function $h_R(\tau)$ in the convolution integral accounts for the material Raman response. The real part of $h_R(\tau)$ and the corresponding Raman gain spectrum are given for silica in figure 2.4 [66]. As the gain spectrum shows, the Stokes photon is most likely to have a frequency which is 13.2 THz lower than the incident pump photon (for anti-Stokes photons, the frequency is most commonly increased by the same amount). The broad Raman gain bandwidth for silica is the result of its amorphous structure. As the emission of Stokes and anti-Stokes radiation can also be stimulated, the Raman effect is

amplified exponentially once fibre losses are overcome:

$$\frac{dI_{\mathrm{S}}}{dz} = g_R(\Omega) I_{\mathrm{pump}} I_{\mathrm{S}} - \alpha_{\mathrm{S}} I_{\mathrm{S}} \tag{2.22}$$

where I_{pump} is the intensity of the propagating Raman pump light, I_{S} is the intensity of the Stokes radiation. and α_{S} is the fibre loss for the Stokes radiation.

In a pulsed system with high peak power, Raman amplification of quantum noise occurs and a critical pump peak power for stimulated Raman scattering is given in Ref. [67] as:

$$P_0^{\mathrm{cr}} \approx \frac{16 A_{\mathrm{eff}}}{g_R(\Omega) L_{\mathrm{eff}}} \tag{2.23}$$

where $L_{\mathrm{eff}} = (1 - e^{-\alpha L})/\alpha$. P_0^{cr} provides an approximate output pump power which will give an equal output Stokes power. Beyond this limit the Raman effect transfers energy from the pump light rapidly, such that most of the pump is depleted over a short propagation distance [68].

The final term in the nonlinear operator (equation 2.19) accounts for spontaneous Raman scattering noise [60], where Γ_R is a stochastic variable with frequency domain correlations given by:

$$\langle \Gamma_R(\Omega, z) \Gamma_R^*(\Omega', z') \rangle = \frac{2 f_R \hbar \omega_0}{\gamma} |Im[h_R(\Omega)]| [n_{th}(|\Omega|) + U(-\Omega)] \delta(z - z') \delta(\Omega - \Omega') \tag{2.24}$$

As before, $\Omega = \omega - \omega_0$. Function $n_{\mathrm{th}} = [e^{\hbar\Omega/k_B T} - 1]^{-1}$ is the thermal Bose distribution, which scales the anti-Stokes and Stokes contribution according to the increase in phonon density with temperature [69], and U is the Heaviside step function.

2.4 Numerical methods

This section introduces the numerical methods used throughout this work for simulating pulse propagation in optical fibre. A fourth-order Runge-Kutta integrator was used to propagate the field in the interaction picture (the RK4IP method) [70]. Advantages for implementing a frequency domain formulation of the RK4IP method have been reported [71], and are described here. The frequency domain formulation also allowed for the Conservation Quantity Error (CQE) method to be used in conjunction with the RK4IP method for adaptive step sizing, leading to improved computational efficiency [72]. Python functions for solving both the scalar and vector GNLSE (i.e., with and without polarization effects) using these methods are given in Appendix D, and were adapted by the author from Ref. [70], as well as through useful discussions

with Dr. Alexander Heidt. The scripts which used the functions to simulate the pulse propagation were entirely the author's work.

2.4.1 The RK4IP algorithm

In the literature, approximate solutions to the GNLSE have been found using the symmetric split-step Fourier method (SSFM) [73], which operates under the assumption that dispersion and nonlinearity act independently and consecutively over short propagation distances. In reality, the operators act together, and as such this approximation generates numerical errors as the field envelope is propagated from one longitudinal position (z) to the next ($z+h$). This propagation error is generally of order $O(h^2)$ [58, 74].

It has been shown that a Runge-Kutta in the interaction picture (RK4IP) method can be applied to nonlinear pulse propagation problems [70] with a propagation error of order $O(h^5)$. The dispersive and non-dispersive operators are separated by transforming the field into the interaction picture, which is done by multiplying the field envelope by a factor of $\exp((h/2)L)$. In contrast to the SSFM, this distributes the effect of dispersion over both the field and the nonlinear operator, resulting in better integration of the nonlinearity and dispersion. Solutions to the GNLSE may then be found by propagating the field using the Runge-Kutta integration method. The RK4IP method was chosen over SSFM due to the improved propagation error. This not only provides high accuracy when simulating nonlinear pulse propagation, but also allows for greater flexibility when optimizing accuracy and computation time. The relative propagation error of order $O(h^3)$ between the two methods implies that greater accuracy can be achieved for the same computation time for the RK4IP method, or that equal accuracy can be achieved in greatly reduced computation time.

The algorithm for advancing the field envelope from position z to $z+h$ is demonstrated by equation set 2.25, in which A_I is the field in the ineraction picture, h is the step size, and all other parameters have their usual meanings [70].

$$\left.\begin{aligned}
A_I &= \exp\left(\frac{h}{2}L\right)A(z,T),\\
k_1 &= \exp\left(\frac{h}{2}L\right)\left[h\hat{N}A(z,T)\right]A(z,T),\\
k_2 &= h\hat{N}\left(A_I+\frac{k_1}{2}\right)\left[A_I+\frac{k_1}{2}\right],\\
k_3 &= h\hat{N}\left(A_I+\frac{k_2}{2}\right)\left[A_I+\frac{k_2}{2}\right],\\
k_4 &= h\hat{N}\left(\exp\left(\frac{h}{2}L\right)(A_I+k_3)\right)\left[\exp\left(\frac{h}{2}L\right)(A_I+k_3)\right],\\
A(z+h,T) &\approx \exp\left(\frac{h}{2}L\right)\left[A_I+\frac{k_1}{6}+\frac{k_2}{3}+\frac{k_3}{3}\right]+\frac{k_4}{6}
\end{aligned}\right\} \tag{2.25}$$

The first line of equation set 2.25 defines the interaction picture representation of the field, before the first nonlinear step is defined by intermediary parameter k_1. Following this, consecutive nonlinear operations act on A_I (defined by $k_{2\text{–}4}$), before the dispersive step is finalized in the Runge-Kutta integration step in the final line. For each consecutive nonlinear operation k_1 to k_4, the operator is redefined using the latest intermediary version of the interaction picture field (i.e., $A_I + k_i/2$). For the definition of k_i and $\hat{N}$, large curved and square brackets denote the interaction picture field used to define the operator and that which the operator acts on, respectively. This process is repeated for n consecutive longitudinal steps until $\sum_n h_n = L_{\text{fibre}}$.

In the SSFM and RK4IP approaches described above, the dispersive and nonlinear operators are applied in the frequency and time domains, respectively. Considering numerical accuracy and efficiency, a formulation involving only the frequency domain may be used with the following advantages:

1. The Raman convolution in equation 2.19 is transformed to a multiplication of the Raman gain spectrum with $|A(z, \omega-\omega_0)|^2$ through the convolution theorem, which greatly reduces computation time.

2. Numerical error from the time domain derivatives shown in both equations 2.16 and 2.19 may be avoided. Transferring to the frequency domain replaces the derivatives with a multiplication by $-i(\omega - \omega_0)$, where ω_0 is the central frequency of the pulse envelope. Thus SS is included without approximation, increasing accuracy.

3. Wavelength dependence of fibre loss, gain, nonlinear parameter γ (and therefore MFD) may also be taken into account [75].

Consequently, the frequency domain formulation of the RK4IP method was adopted. The dispersive parameter and nonlinear operator defined in equations 2.16 and 2.19 have frequency domain formulations as follows:

$$\tilde{L}(\Omega) = -\frac{\alpha(\Omega)}{2} + i\sum_{n\geq 2}^{\infty} \beta_n \frac{\Omega^n}{n!} \tag{2.26}$$

$$\hat{N}(\Omega) = -i\gamma \frac{1}{A_m(z,\Omega)} \left(1 + \frac{\Omega}{\omega_0}\right) \left(F\left[(1-f_R)\left(|A_m(z,T)|^2 + \frac{2}{3}|A_n(z,T)|^2\right)A_m(z,T) \right.\right.$$
$$\left.\left. + f_R A_m(z,T) F^{-1}\left[\tilde{h}_R F\left[|A_m(z,T)|^2\right]\right] + i\Gamma(z,T)\right]\right) \tag{2.27}$$

Again, $\Omega = \omega - \omega_0$. F and F^{-1} denote the Fourier transform and its inverse, respectively, and $\tilde{h}_R$ is the Fourier transform of the Raman response function. As before, subscripts m and n denote orthogonally polarized field components.

2.4.2 The conservation quantity error method

Setting the propagation step size is crucial for retrieving accurate computational data. If the step size is too large then the propagation error will become intolerable, leading to artefacts in the simulated field envelope. However, overcompensating for this effect by setting a very small step size can lead to computational inefficiency. It is therefore often useful to implement an adaptive step sizing algorithm which monitors a defined error parameter as the field is being propagated and adjusts the step size accordingly.

For the majority of nonlinear pulse propagation simulations in this thesis, the CQE method is adopted for adaptive step sizing [72, 74]. This method is based on the fact that, neglecting fibre loss, the GNLSE conserves the optical photon number, P, during propagation:

$$\frac{\partial P}{\partial z} = \frac{\partial}{\partial z}\left(\int S(\omega)\frac{|\tilde{A}(z,\omega)|^2}{\omega}d\omega\right) = 0 \tag{2.28}$$

where $S(\omega) = n_{\text{eff}}(\omega)A_{\text{eff}}(\omega)$ [76]. $S(\omega)$ can be taken out of the integral assuming that the frequency dependence is negligible, which reduces P to the photon number of the field.

The CQE method uses the photon number and the conservation property of the GNLSE to define an error parameter associated with the propagation step size. Ideally, it should be the case that $P(z+h) = P(z)$. However, after each advance in longitudinal position z, there will exist a difference in photon number on the order of $O(h^5)$. This is calculated by taking the absolute difference between the photon numbers before and after the propagation step. Converting from photon number to intensity, one obtains:

$$|\tilde{A}(z+h,\omega)|^2 = |\tilde{A}(z,\omega)|^2 + \Delta I(h,\omega) \tag{2.29}$$

where $\Delta I(h,\omega) = \eta(\omega)h^5 + O(h^6)$ for the RK4IP method. Here, η is a scaling parameter for each frequency grid point. Substituting equation 2.29 into 2.28 gives:

$$\Delta_{\text{Photon}}(h) = \left|\int \Delta I(h,\omega)\frac{S(\omega)}{\omega}d\omega\right| \tag{2.30}$$

Therefore the photon number error is given by the integral of ΔI over the frequency window. An estimate of the local error from propagation step z to $z+h$ can therefore be reached by comparing $\Delta_{\text{Photon}}(z)$ and $\Delta_{\text{Photon}}(z+h)$. As the photon number is a function of h^5, it may be controlled with a high degree of accuracy by adjusting h.

By normalizing the difference $|\Delta_{\text{Photon}}(z) - \Delta_{\text{Photon}}(z+h)|$ by $\Delta_{\text{Photon}}(z)$, a relative measure of the photon error is obtained, δ. This parameter is then compared with a user-defined input tolerace, δ_{tol}, which determines how h is scaled using the following rules:

1. If $\delta > 2\delta_{\text{tol}}$: Solution is discarded, and the step is repeated with $h/2$ step size.
2. If $\delta_{\text{tol}} < \delta < 2\delta_{\text{tol}}$: Divide h by $2^{1/5}$ for the next step.
3. If $\delta < 0.1\delta_{\text{tol}}$: Multiply h by $2^{1/5}$ for the next step.

The powers of 1/5 have been chosen due to the $O(h^5)$ propagation error for the RK4IP method. This value was also found to dampen oscillations in the adjusted value of h which would otherwise appear when $\Delta I(h,\omega) < 0$ for some frequency values [74]. Typically, $\delta_{\text{tol}} = 10^{-9}$ to 10^{-13} for Fourier grid sizes between 2^{11} and 2^{14}. In conjunction with the CQE method, it has recently been shown that the RK4IP method is the fastest nonlinear pulse propagator to date for a given propagation error [70, 71].

2.4.3 Quantum noise and coherence

In fibre CPA and supercontinuum arrangements, the random amplitude and phase fluctuations exhibited by the seed laser can be amplified by nonlinearity, and therefore strongly determine the coherence of the system output [60, 77, 78, 79]. It is possible to simulate the effect of noise in nonlinear fibre optics applications using the GNLSE, and to characterize the resulting coherence of the system output using the spectral phase stability over an ensemble of simulations. This subsection describes how this was done for this thesis work.

Shot noise was included by adding one photon with random phase to each frequency bin to model the effects of spontaneous emission [67]. This was done before the propagation step while the pulse was being defined. Spontaneous Raman noise (as discussed in section 2.3) was included using a randomized function with frequency domain correlations given by equation 2.24. Unlike the shot noise, this was added with each iteration of the RK4IP algorithm to simulate the effect of spontaneous Raman scattering for each increase in propagation distance from z to $z+h$.

The noise sensitivity of the simulated output was characterized as a relative measure over a large ensemble of independently generated pairs of spectra, and was calculated using the modulus of the complex first order degree of coherence at each wavelength [60]:

$$\left|g_{12}^{(1)}(\lambda, t_1 - t_2)\right| = \left|\frac{\langle E_1^*(\lambda,t_1)E_2(\lambda,t_2)\rangle}{\sqrt{\langle|E_1(\lambda,t_1)|^2\rangle\langle|E_2(\lambda,t_2)|^2\rangle}}\right| \tag{2.31}$$

Angular brackets denote the ensemble average over independently generated pairs of spectra, and t is the time measured at the scale of the temporal resolution of the spectrometer used to resolve these spectra. The function is normalized such that it is real valued over the interval $[0; 1]$, with a value of 1 indicating perfect coherence. The wavelength dependence of $\left|g_{12}^{(1)}\right|$ is of interest for characterizing spectral phase stability, and is calculated for time $t_1 - t_2 = 0$ s. As $\left|g_{12}^{(1)}\right|$ is defined to compare phase stability between independently generated pairs of spectra, it is possible to compute equation 2.31 using a relatively small number of simulations and, in this thesis, 20 individual spectra are used to generate an ensemble of 190 unique pairs, which is typically accepted in the literature as being sufficient for the averaging.

2.5 Summary

This chapter provided details of the optical fibre technology relevant to this thesis. A brief introduction to single-mode optical fibre was given, before the concept of material and waveguide dispersion was introduced in section 2.1. Following this, the spectroscopy of Yb^{3+}-doped silica was discussed in subsection 2.2.1, with reference to the mechanisms by which the emission spectra of this ion are broadened in the silica host, and the implications that this has for high peak power Yb-doped fibre lasers. Subsection 2.2.2 included details of double-clad optical fibre and cladding pumping for high peak power applications, as well as how this technology can be implemented to mitigate unwanted nonlinear effects. Extension to higher peak powers by endcapping the fibre facets was also discussed.

The relevant equations for describing the dispersive and nonlinear characteristics of optical fibre and the relevant optical effects were included in section 2.3. The definition of the field envelope was first introduced before the GNLSE. The dispersion parameter and length, used in later chapters to estimate the temporal broadening and increase in spectral phase due to second order dispersion, were also introduced. The nonlinear operator used to model both instantaneous and delayed intensity dependent scattering followed, with a discussion about SS, SPM, and XPM, the nonlinear length, and the B-integral. Both spontaneous and stimulated Raman scattering were then introduced as delayed nonlinear effects.

Section 2.4 introduced the RK4IP propagator used for all nonlinear simulations in this thesis. A brief description of the algorithm was given, and the improved propagation error over the SSFM technique and the benefits of employing the frequency domain formulation of the RK4IP method were described. Following this, the CQE adaptive step sizing algorithm was presented in subsection 2.4.2, and its integration with propagation simulations for improving computational efficiency for a user-defined error tolerance were

discussed. The chapter concluded with a brief description of how shot and spontaneous Raman noise were implemented in the simulations, and how the spectral phase stability was quantified.

Chapter 3

Multi-wavelength modelocked Yb^{3+}-doped fibre oscillator

3.1 Introduction

A modelocked fibre oscillator operating around 1045 nm was required to enable stable power scaling of the CPA system. A low-noise cavity with the potential for carrier-envelope phase locking was also desirable. In contrast, achieving high output power was not a requirement due to the low damage threshold of an electro-optic modulator positioned at the oscillator output in the CPA design. Given these requirements, a low nonlinearity stretched-pulse ring laser [80] modelocked using nonlinear polarization evolution (NPE) was selected based on the recommendation of Professor F. Ömer Ilday (director, UFOLAB, Bilkent University, Ankara, Turkey), a collaborator and leading researcher in the short pulse fibre laser field. Such a cavity design is expected to have low noise operation compared to soliton or similariton lasers [81].

The work started with my visit to the UFOLAB for four weeks in March 2013, where I built a breathing pulse oscillator using a design developed by Prof. Ilday. However, this laser operated at a wavelength of 1035 nm, which was unsuitable for the fibre CPA system due to a mismatch with the gain peak of the final amplifier (∼1040 nm) and the poor reflectivity of two curved dielectric mirrors in the CPA stretcher for wavelengths below 1038 nm. This cavity design was later adapted at the Optoelectronics Research Centre (ORC) by using a longer Yb-doped fibre to move the gain peak towards longer wavelengths. The final design demonstrated good stability, self-starting, and the correct average power around 1045 nm to seed the fibre CPA system. Due to the longer gain fibre and increased accumulated nonlinear phase per roundtrip, a novel multi-wavelength modelocking state was observed. Following this, I developed a detailed vectorial model

of the cavity which allowed for the multi-wavelength modelocking to be identified as the separation of a single circulated pulse by wavelength according to an inhomogeneous polarization state induced by overdriven NPE. Such analysis of the cavity dynamics is generally not seen in the literature, which is largely focussed on experimental observation alone.

This chapter is structured as follows. Section 3.2 introduces the development of breathing pulse Yb-doped fibre cavity designs, and compares the operation of Prof. Ilday's cavity design with that which was developed later at the ORC. Section 3.3 describes the performance of the cavity and the noise characteristics, as well as the multi-wavelength dynamics observed in the experiment. Section 3.4 first introduces a scalar cavity model which was used in the initial stages of the simulation development and describes how nonlinearity, dispersion, and polarization independent losses were incorporated. This model is then extended to include the polarization dependent (vector) cavity dynamics, which allows for the NPE fast saturable absorber to be modelled and for self-starting single- and multi-wavelength modelocking solutions to be found. The hypothesized cavity dynamics responsible for the multi-wavelength modelocking are confirmed in this section. Finally, the multi-wavelength oscillator developed in this work is compared with others reported in the literature in section 3.5 before the chapter is concluded in section 3.6.

3.2 Cavity design

The first demonstrations of modelocking in fibre lasers were based on soliton dynamics [82]. However, increasing the pulse energy for these cavities proved difficult due to the high peak power maintained throughout the cavity, which can eventually lead to pulse break-up as the energy is scaled [83]. A dispersive delay line (DDL) was incorporated into the cavity design to form a so-called breathing pulse cavity such that $\beta_2 \approx 0$ for quasi-soliton operation, which increased the energy threshold for pulse breakup by reducing the intracavity peak power. Ring cavity designs were also adopted instead of Fabry-Perot designs for a reduced B-integral per roundtrip, made possible by moving all of the gain to the final section of the cavity fibres. This reduces the roundtrip nonlinearity without changing the total fibre length, thus maintaining the cavity dispersion and the delay line for high pulse energy at a moderate average power, which is limited to <1 W by the availability of single-mode pump diodes.

Figure 3.1a) shows how this is achieved by controlling the fibre lengths in the breathing pulse ring cavity design constructed during my trip to Ankara. The figure shows the fibre section of the cavity only. Red arrows indicate the propagation direction, and the approximate pulse shape is included at the input and output of the fibre section,

where colourmap indicates pulse chirp. A dispersive delay line and the optics which close the cavity are omitted from the diagram for simplicity. A commercial Yb-doped fibre (nLight) with a high doping concentration enabled a short gain fibre length (35 cm), localising the gain to a specific part of the cavity. This enables segregation of the dispersion, gain, and nonlinearity, allowing for relatively high pulse energies (∼nJ) to be extracted with low nonlinear distortion from cross-phase modulation (XPM). A homogeneous polarization state was produced across the entire pulse duration (demonstrated by ellipses above the pulse shape in the figure), which resulted in self-starting, single-pulsing operation through the NPE-based saturable absorption mechanism.

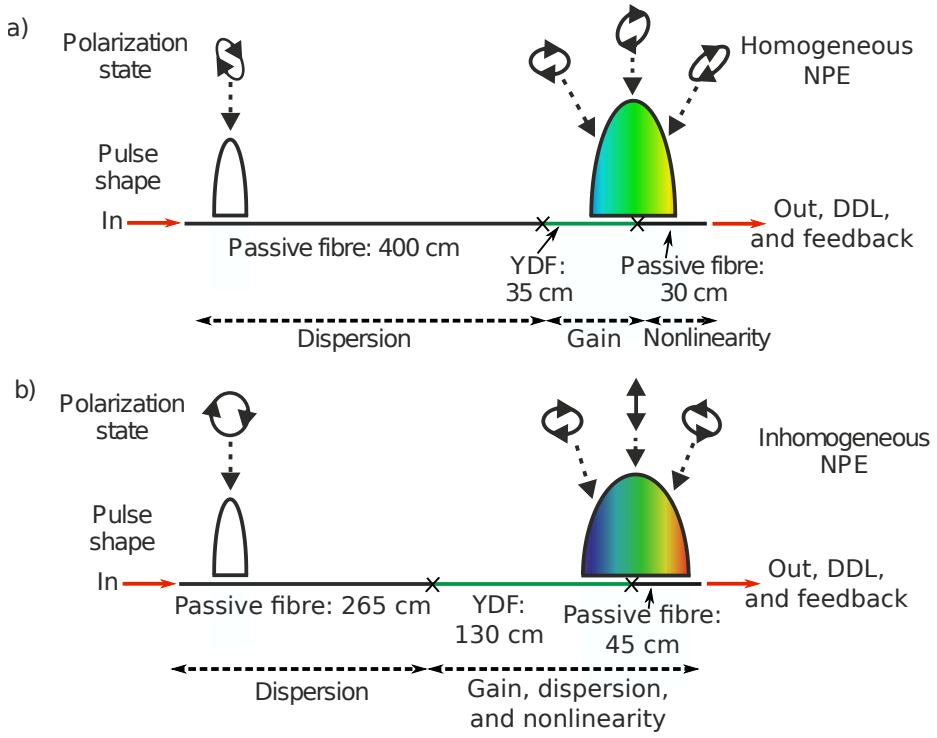

FIGURE 3.1: Simplified schematic of the pulse evolution along the fibre section of the two cavity designs. a) The cavity developed by Prof. Ilday with clearly delineated dispersive and nonlinear sections of fibre in the cavity. b) The cavity developed as part of this thesis work, with strong coupling between dispersion and nonlinearity. Considering the variation in polarization state across the pulse a polarization selection mechanism would lead to two separate pulses.

As described, this cavity operated at an unsuitable wavelength and so the design was adapted by uising a longer Yb-doped fibre to move the gain peak towards longer wavelengths. To reduce the cost of each iteration in the development stage, an ORC-fabricated Yb-doped fibre was used in place of the highly doped commercial fibre. This fibre had a lower doping concentration, necessitating a longer gain fibre length of 130 cm. As such, the dispersion, gain, and nonlinearity were no longer delineated for the fibre section of this cavity design, which is shown in figure 3.1b). The result was a stronger

coupling between dispersion and nonlinearity, which altered the cavity dynamics significantly by introducing an inhomogeneous polarization state across the pulse through XPM. Coupled with the pulse chirp, this led to a wavelength dependent polarization state as shown by the ellipses above the pulse at the end of the fibre section in the figure. The chirped pulse could then be divided into sections at the polarizing optics of the NPE-based saturable absorber, with each pulse section having a different central wavelength.

3.3 Experiment

The uni-directional breathing-pulse ring cavity configuration is shown in figure 3.2. A 400 mW single-mode fiberized diode (976 nm) was used to pump a 1.3 m length of Yb-doped aluminosilicate fibre, which was fabricated at the ORC. The total loss of the intra-cavity 980/1030 nm fused wavelength division multiplexer (WDM, Lightel) and the fiberized dichroic filter was measured to be 3 dB for the pump wavelength, giving a pump power of 200 mW at the splice point between the WDM and the Yb-fibre. The dichroic filter was formed of two WDMs, one with a pass/reject band of 980/1030 nm and the other 980/1060 nm to ensure effective pump protection from counter-propagating ASE. A 45 cm length of HI1060 (Corning, Inc.) was spliced onto the Yb-fibre to increase the accumulated nonlinear phase per roundtrip of the cavity which was found to make self-starting modelocking more likely. A quarter waveplate (QWP) and a half wave-

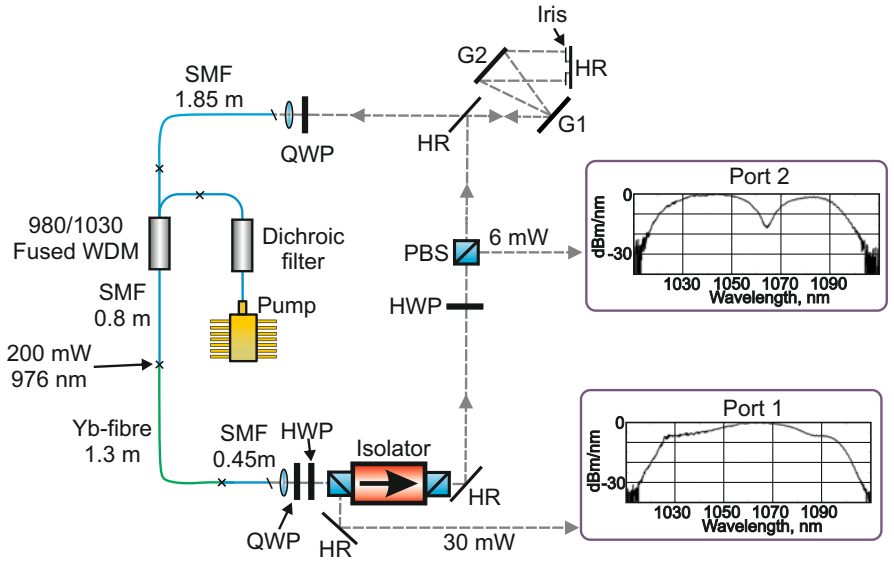

FIGURE 3.2: Schematic of the Yb-fibre oscillator. The insets show the spectra emitted simultaneously by the two output ports during multi-wavelength operation. Port 2 shows a spectral minimum at 1064 nm, corresponding to the central wavelength of the output from port 1.

plate (HWP) were used in conjunction with the first polarizing beam splitter (PBS) of

a free-space Faraday isolator to form the nonlinear polarization evolution optical switch which modelocked the laser [63]. The isolator ensured unidirectional circulation of the pulses within the cavity (anticlockwise in figure 3.2). The following HWP and PBS formed a variable output coupler, before a grating compressor (600 lines/mm, G1 and G2 in the diagram) provided approximately -1.3×10^5 fs^2 group delay dispersion (GDD) compensation for a grating separation of 8.5 cm. Taking a typical dispersion value of $D(\lambda) = -38$ ps/(nmkm) for the fibre and considering the total fibre length of 4.4 m, a total fibre dispersion of 1×10^5 fs^2 indicates that the net linear dispersion in the cavity is anomalous. An iris at the folding mirror of the compressor provided spectral filtering for control over both the central operating wavelength and the bandwidth. The QWP positioned after the compressor was used to control the polarization state of the pulses at the input to the fibre section of the cavity. It was found that a 2.65 m length of passive single-mode fibre was required for stable self-start modelocking, and was formed from a length of HI1060 and the WDM pigtails (OFS 980 fibre). The cavity roundtrip time was approximately 25 ns (∼40 MHz repetition rate) including the free-space section.

Typical output powers from ports 1 and 2 were 30 mW and 6 mW, giving output pulse energies of 0.75 nJ and 0.15 nJ, respectively. The pulse duration was estimated to be approximately 2 ps FWHM from autocorrelation data at ports 1 and 2, assuming a Gaussian intensity profile. The output coupling ratio was 41% at port 2 (this ratio was found to provide the most reliable self-start modelocking). Then adding the isolator, compressor, WDM, fibre launch, and iris insertion losses, the total output power was used to estimate a round-trip gain of approximately 19.7 dB, from 0.5 mW input signal power to the length of Yb-fibre, to 47.2 mW output power before the free-space isolator. It should be noted that increasing the circulated pulse energy (e.g. by increasing the pump power or decreasing cavity loss) led to the observation of pulse breakup into two discrete, temporally separated pulses as would be expected for this type of cavity [84]. The dynamics of the multi-wavelength operation with a single temporally circulating pulse reported here were observed below the cavity threshold for pulse breakup.

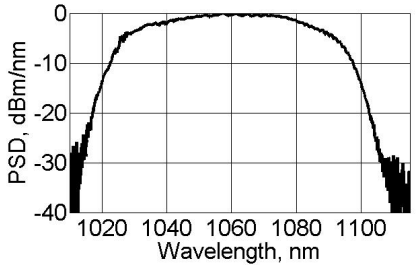

FIGURE 3.3: Spectrum at the output of the fibre section before port 1, calculated by scaling the spectra from ports 1 and 2 and summing them (see Fig. 3.2 and main text).

The insets in figure 3.2 show the spectra from ports 1 and 2. The -10 dB width of the output from port 1 is 72 nm, corresponding to a transform limited pulse duration

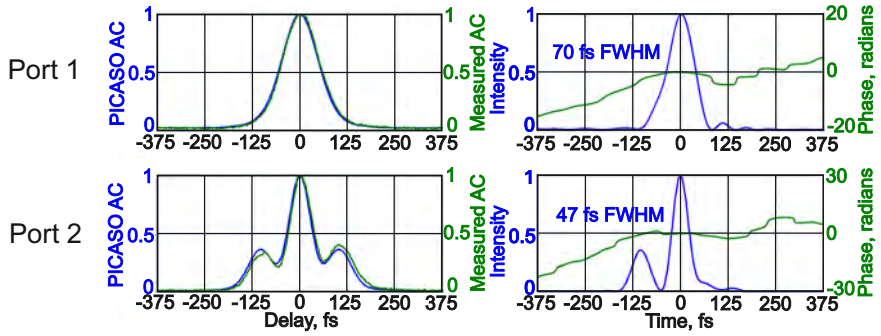

FIGURE 3.4: Left column: Measured and PICASO reconstructed autocorrelation data for ports 1 and 2. Right column: PICASO reconstructed intensity and phase for ports 1 and 2.

of approximately 48 fs at FWHM of the intensity. Port 2 exhibits a ∼15 dB spectral modulation at approximately 1064 nm. As a result, this port produces two pulses in the time domain, with the most energetic pulse having a transform limited duration of 39 fs at intensity FWHM, and a central wavelength of 1045 nm, corresponding to the main spectral peak. Normalising the spectra from ports 1 and 2 to their corresponding pulse energies and adding them together yields the spectrum before the first PBS of the Faraday isolator, shown in figure 3.3. The spectrum is flat, broad, and without strong modulation, indicating that a single pulse is emitted by the fibre section and is subsequently split at the first PBS of the isolator.

Figure 3.4 shows the time domain measurements of the output from both ports after the pulse chirp is removed by an external grating-based compressor (not shown in figure 3.2). The green line plots of the first column show the autocorrelations of the externally compressed output pulses from ports 1 and 2 (upper and lower, respectively). These were used alongside the spectra from figure 3.2 in a Phase and Intensity from Cross-Correlation and Spectrum Only (PICASO) algorithm [85] (program provided by Prof. F. Ö. Ilday) to give the temporal intensity and phase distributions of the pulse. Note that the signs of the time axis and phase are ambiguous for this retrieval as a balanced autocorrelation was used as opposed to a cross correlation. The output of this algorithm is shown in the second column of figure 3.4. The first plot in this column shows that the pulse from port 1 was compressed to a duration of 70 fs at the intensity FWHM (1.54 times transform limited). A significant amount of third order dispersion is predicted by the PICASO algorithm, so this duration may be reduced by using a better optimized compressor setup. The PICASO reconstruction of the pulse from port 2 shows a main (primary) pulse with near zero chirp compressed to 47 fs, and a satellite (secondary) pulse compressed to 63 fs FWHM intensity. The satellite pulse shows a clear linear chirp over its duration. The linear chirp indicates a difference in the amount of anomalous dispersion required to compress the secondary pulse with respect to that required for compression of the primary pulse. This is expected from

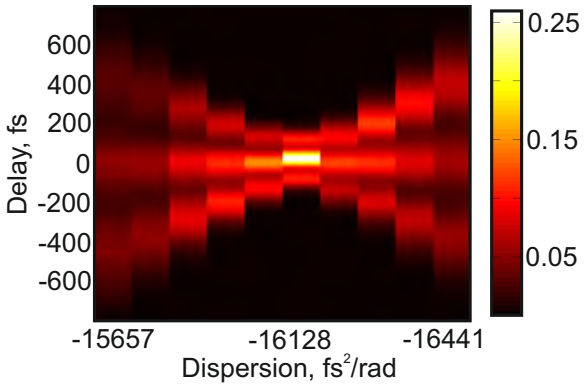

FIGURE 3.5: Autocorrelation of the output from port 2 as a function of dispersion applied by an extra-cavity compressor. The colourmap shows the autocorrelation signal.

the difference in $D(\lambda)$ of the fibres in the cavity for the two peak wavelengths in the port 2 output, and also from the differing amount of nonlinear chirp gained by the two pulses as they propagate in the fibre. Unfortunately, it is not possible for PICASO to quantify the relative chirp difference from this data set without an ambiguity in sign. The PICASO data does, however, indicate that port 2 produces two modelocked pulses with different central wavelengths to one-another (1045 nm and 1085 nm for the primary and secondary pulses, respectively), and the single pulse produced by port 1 (1064 nm).

By adjusting the external compressor grating separation it is possible to set the residual pulse chirp to non-zero values, allowing for time-of-flight measurements to be made for the output from port 2 as a function of wavelength and for the relative behaviour of the pulse peaks to be understood in more detail. Figure 3.5 shows how the autocorrelation function of the output from port 2 varies with applied compressor dispersion. The autocorrelation function is seen to maintain the triple-peaked structure, and the linear increase in temporal separation between the primary and secondary pulses either side of the autocorrelation minimum is shown. This indicates that the secondary pulse in the PICASO reconstructions for this port (Fig. 3.4) has a different central wavelength to the primary pulse. By examining the relative size of the peaks from the port 2 spectrum inset in Fig. 3.2 alongside those in the autocorrelation data in Fig. 3.5, it is deduced that the secondary pulse has the longer wavelength. This pulse will experience a longer path length through the external compressor than the main peak, causing the linear increase in separation between the primary autocorrelation peak and its satellite peaks.

Intra-cavity loss varies strongly with wavelength, and is very different for the 1045 nm peak in comparison with the 1080 nm peak. Figure 3.6 shows the transmission characteristics of the intra-cavity WDM for the common-to-1030 nm port, with the output from port 2 underlaid for reference. It is seen that a maximum loss of 21 dB is experienced by the 1080 nm secondary pulse at this component for each roundtrip of the

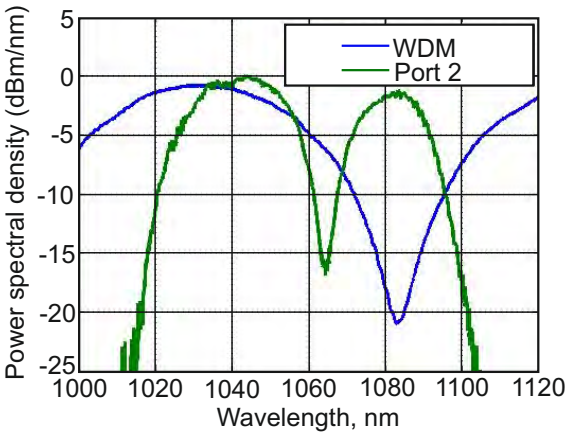

FIGURE 3.6: Intra-cavity WDM transmission (blue) in comparison to the port 2 output pulse (green). The WDM transmission characteristics show up to >21 dB loss is experienced at 1080 nm by the long wavelength part of the pulse. This acts in addition to the spectral filtering at the compressor, indicating that this pulse is regenerated from a low level for each pass of the Yb-fibre, positioned after the WDM.

cavity. This acts in addition to the spectral filtering at the iris in the compressor, which also has a loss in excess of 20 dB for this wavelength band. As this loss exceeds the estimated 19.7 dB gain provided by the Yb-doped fibre, the 1080 nm wavelength band must be regenerated each roundtrip through spectral broadening of the primary peak at 1045 nm, which does not undergo this high roundtrip loss. The loss for the 1080 nm peak also eliminates Raman scattering as a possible cause due to the correspondingly high roundtrip Raman gain required to amplify the 1080 nm peak from noise. In addition, the flat phase profile across this peak (indicated by its compressibility and the PICASO reconstructions) is not typical of Raman broadening.

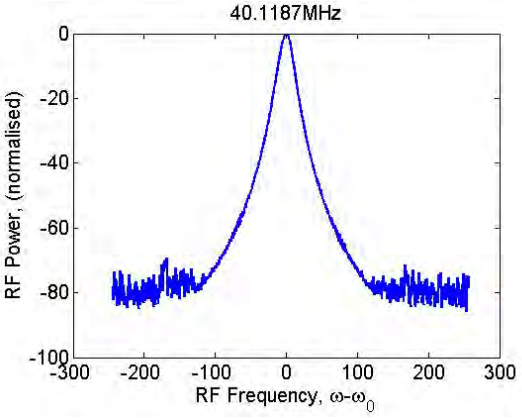

FIGURE 3.7: Fundamental (40 MHz) peak of the oscillator RF spectrum.

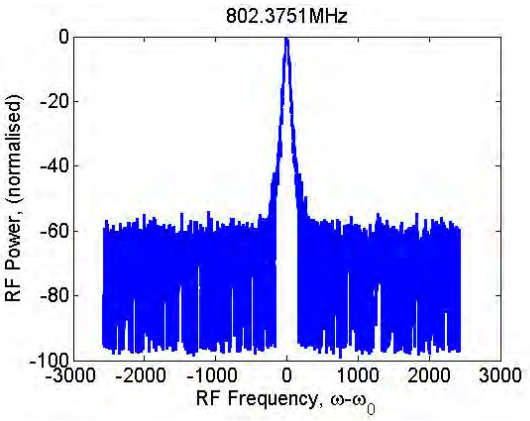

FIGURE 3.8: 20^{th} harmonic (800 MHz) of the oscillator RF spectrum.

As well as providing an accurate measure of the repetition frequency of the oscillator, the radio frequency (RF) spectrum of the cavity as measured by a photodiode may be used to calculate the RMS amplitude noise and timing jitter of the laser. Here,

the method proposed in ref. [86] and summarized in Appendix C was used to calculate the oscillator noise, and involves measuring the respective heights and widths of the RF spectral peaks, their pedestals, and the noise floor. The fundamental of the RF spectrum is shown in Fig. 3.7, and the repetition rate of the oscillator was 40.118 MHz. No pedestal is seen for this harmonic, so an upper bound must be calculated for the amplitude noise. Taking the pedestal amplitude to be 80 dB below the peak and the width at the base to be approximately 200 Hz, an amplitude noise of 0.04% is retrieved for a resolution of 10 Hz on the RF analyser. The timing jitter of the oscillator was estimated using a higher harmonic of the RF spectrum, exploiting the dependence of the peak-to-pedestal ratio on the square of the harmonic number to increase the accuracy of the calculation. Figure 3.8 shows the 20^{th} harmonic of the RF spectrum, and the ratio of peak to pedestal heights is approximately 45 dB. This, alongside the ratio of the frequency span at the pedestal (approximately 137 Hz) to the frequency resolution of the RF spectrum analyser, gives a timing jitter of 16.5×10^{-5} of the roundtrip time (4.12 ps).

Although the central wavelength from port 1 is 1064 nm the bandwidth is large and spans the wavelength region required to seed the fibre CPA system (1045±8 nm), and the output power is good. This port is therefore suitable as a source for the fibre amplifier chain.

3.4 Simulation

A script was written which included the approximate characteristics of all cavity components, and was solved using a vectorial adaptation of the RK4IP propagator (introduced in chapter 2). The relevant functions are documented in Appendix D. Although the Raman effect was included in the cavity simulations the Raman ASE term was neglected, and the simulation of quantum noise was simplified to the one photon per mode approach. The cavity development, vectorial nonlinear operator, and the results of the simulations are presented in this section.

Due to the complexity of the oscillator dynamics, it was necessary to separate the development of the simulation into a number of steps, starting with a scalar cavity which neglected polarization effects (subsection 3.4.1). This model cavity served as a test-bed for the gain, dispersion, scalar nonlinear and loss operators used in the cavity, and is shown to support stable pulses over multiple roundtrips for idealized input parameters. Subsection 3.4.2 documents an extension of the scalar cavity model to include a vectorial nonlinear operator, as well as the cavity birefringence. The simulated vectorial cavity exhibited self-starting dynamics from noise-like starting conditions for both the

single- and multi-wavelength modelocking regimes, and enabled a full understanding of the cavity dynamics to be obtained.

3.4.1 Scalar cavity model

This subsection describes the initial development of the modelocking model. A scalar form of the GNLSE is used in conjunction with a parabolic gain approximation and simulated cavity bulk optics, and is shown to support stable modelocked pulses. The fibre dispersion and gain were approximated using the following linear parameter [83]:

$$\tilde{L}_{\text{gain}} = \frac{g}{2} - \frac{g}{2\Omega_{\text{BW}}^2}\left(\Omega - \Omega_{\text{peak}}\right)^2 + i\sum_{n\geq 1}\beta_n\frac{\Omega^n}{n!} \tag{3.1}$$

in which g is the saturable gain of the fibre (units of m^{-1}). Ω_{BW} represents the gain bandwidth of the fibre, Ω and Ω_{peak} represent the angular frequency Fourier grid (centred at a user-selected central angular frequency, usually that of the starting pulse) and the angular frequency of the gain peak, respectively. The Taylor expansion in the third term on the right hand side accounts for the linear dispersion of the fibre, and β_n denote the Taylor coefficients for the dispersion orders. Gain saturation was taken into account using the following:

$$g = G\exp\left(-\frac{\int\left(|u|^2 + |\nu|^2\right)dt}{E_{\text{sat}}}\right) \tag{3.2}$$

Here, u and ν represent the complex field envelopes along the x and y birefringence axes of the fibre (ν has zero value for this scalar model, but will be complex valued for the vector model), E_{sat} is the maximum extractable energy (determined by the pump power), and G is the small signal gain coefficient in m^{-1}. For the lengths of passive single-mode fibre, the linear parameter had the usual form as given in equation 2.26.

Once the linear parameters were defined, the nonlinear operator was expressed in the same manner as in chapter 2, and the pulse was propagated using the RK4IP algorithm to integrate the following GNLSE[1]:

$$\frac{\partial\tilde{A}_m(z,\Omega)}{\partial z} = \left(\hat{D}_{\text{passive/gain}} + \hat{N}\right)\tilde{A}_m(z,\Omega) \tag{3.3}$$

where $\hat{D}$ is the linear operator defined as $\exp(hL/2)$.

When simulating the scalar cavity, only linear loss and anomalous dispersion were included in the bulk optics section. The compressor dispersion was set to approximately

[1]It should be noted that the CQE method described in chapter 2 is not appropriate for the length of gain fibre, where photon number is not conserved. It was, however, used for the two lengths of passive SMF (assumed lossless) either side of the gain fibre as shown in figure 3.2.

Parameter	**Value**
λ_c	1064 nm
$\Delta\lambda$	1 nm
C	-2
λ_g	1064 nm
$\Delta\lambda_g$	12 nm
Rep. rate, R	40 MHz
Average power, P_{av}	480 μW
Field	$(0.94P_{\mathrm{av}}/(RT_{\mathrm{FWHM}}))^{0.5}\exp\left[-((1+iC)/2)(t^2/t_0^2)\right]$

TABLE 3.1: Input pulse parameters for the stable scalar modelocking simulation.

-1×10^5 fs^2. G and E_{sat} were set iteratively, such that the steady-state output power from the fibre section of the cavity matched that calculated in section 3.3 at approximately 47 mW. G was set to 6 m^{-1}, and E_{sat} to 0.8 nJ to give 30 mW from port 1 and 6 mW from port 2 in the simulated scalar cavity, using the measured output coupling ratios for these ports. The cavity loss was accounted for in the scalar simulations by including a net loss term in the compressor, rather than considering each component individually. This approach is justified as the free-space section of the cavity is purely linear, so the order of the components may be neglected and their effect superimposed. The loss was set to 99% so that the power at the input to the Yb-fibre section was equal to $\sim$ 0.5 mW, as calculated in section 3.3. This loss value incorporated the insertion loss of the isolator, WDM, the throughput efficiency of the cavity compressor, and the free-space to fibre launch, as well as the loss at each output port. The value is commensurate with the estimated steady-state roundtrip gain of 19.7 dB.

The user-specified input pulse parameters for the scalar cavity model are given in Table 3.1, and define a Gaussian pulse which was injected into the input end of the fibre section, which was used as the starting point for the simulations. The central wavelength was chosen to match that of the single pulse from port 1 of the experimental setup. The narrow bandwidth was chosen in order to allow for some degree of pulse development during circulation, and the negative chirp was applied to simulate the initial spectral and temporal narrowing caused by SPM acting on a negatively chirped pulse in the normal dispersion regime, whilst also emulating the spectral phase of the circulated pulses at this point in the experimental cavity. It was assumed that the gain peak of the active fibre was centred at the spectral peak of the pulses, and that the gain bandwidth was 12 nm. The repetition rate and average power at the input to the fibre section of the cavity were chosen to match the experimental values.

In this configuration, a pulse evolved into a stable solution for a single polarization state, as shown in the time domain by figure 3.9. As there is no saturable absorption in this model, it is not possible for this cavity to self-start from arbitrary input parameters. The figure shows the pulse evolution over 200 roundtrips of the cavity, and it is

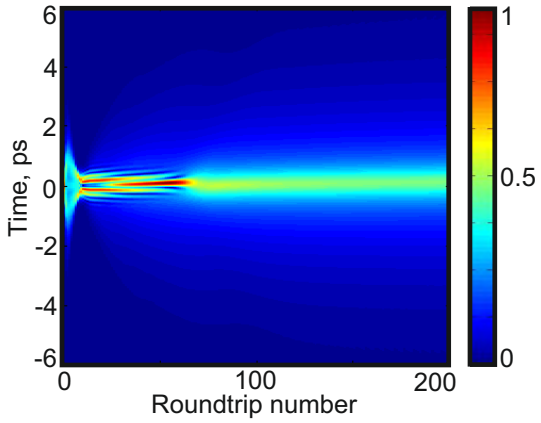

FIGURE 3.9: Simulation showing a stable scalar modelocking solution for the cavity.

seen to stabilize after roundtrip number 75. The stabilization is the result of the linear loss, gain bandwidth, and dispersion management acting with self-phase modulation to restrict the pulse bandwidth to within a certain range, indicating that the linear and nonlinear operators are working correctly.

3.4.2 Vector cavity model

Having confirmed that the simulated cavity can support stable pulses for many roundtrips, the model was then extended to a vectorial form. This subsection details this developmental step and how birefringence was simulated. The vector cavity is shown to self-start from noise-like starting conditions for both single- and multi-wavelength operation using NPE as the fast saturable absorption mechanism.

The RK4IP propagator was modified to include the effects of nonlinear polarization mixing through cross-phase modulation (XPM, chapter 2) between orthogonal polarization modes using the nonlinear operator given in equation 2.27. As shown in Appendix D.2, the field is represented by a $[2, 2^N]$ array. The two polarization components are stored along the rows, and the columns give the complex field envelope in the time domain. The fibre birefringence was included in the simulations by adding an extra Taylor expansion coefficient in the dispersion profile of one of the fibre axes to account for the group velocity mismatch between the polarization modes (β_1 in the notation of equations 3.1 and 2.26). The dispersion information of the fibre was otherwise assumed to be independent of the orientation of the fibre axes. Single-pass propagation of arbitrary pulse shapes through the fibre section of the simulated cavity allowed for asymmetric spectral broadening to be observed as a function of group velocity mismatch and the relative peak powers of the pulse polarization components, confirming that the XPM term was working correctly.

Additional components were added to the model cavity to account for the polarization control that makes up the NPE-based fast saturable abosrber. This was done using the Jones matrix formalism for the waveplates. The Jones matrices for half and quarter waveplates at arbitrary angular orientation to the x-axis are given in equations 3.4 and 3.5 below.

$$\mathrm{HWP} = \begin{pmatrix} \cos(2\theta) & \sin(2\theta) \\ \sin(2\theta) & \cos(2\theta) \end{pmatrix} \tag{3.4}$$

$$\mathrm{QWP} = \begin{pmatrix} \cos^2(\theta) + i\sin^2(\theta) & \cos(\theta)\sin(\theta) - i\cos(\theta)\sin(\theta) \\ \sin(\theta)\cos(\theta) - i\sin(\theta)\cos(\theta) & \sin^2(\theta) + i\cos^2(\theta) \end{pmatrix} \tag{3.5}$$

The circulated polarization state determines cavity loss for this design, and so must be considered carefully. The polarizing beam splitters used in the experimental setup transmitted light polarized along the horizontal axis, and so all light reflected at ports 1 and 2 was removed from the cavity in the simulations. Unlike port 1, the output coupling optics of port 2 were simulated using a more simple method which did not involve Jones matrices, permitted by the fact that the Farady isolator used in the experimental cavity transmitted only the horizontally polarized field component. The vertical component of the polarization was set to zero as this port produces output from the reflection of a PBS, and the loss seen by the circulating power was set to approximately 40%, mirroring the experimental design. Additional loss was included at the compressor so that the diffraction efficiency was taken into account, and any remaining vertical component was set to zero at the compressor in the simulations to account for the compressor being much higher for one polarization state. The vertical polarization component of the field was in general reset to a non-zero complex value by the quarter waveplate at the input to the fibre section, which allowed for a larger accumulated nonlinear phase through XPM, thus increasing the likelihood of finding a stable modelocked solution.

Due to the polarization dependent cavity loss, both the waveplate angles and gain characteristics must be balanced in order to match the output powers from ports 1 and 2 seen in the experimental setup. As with the scalar simulation, this cavity was found to support stable modelocking solutions when the process was initiated by user-defined starting pulse characteristics for particular sets of waveplate angles and gain parameters.

It was found that the vectorial cavity simulations were also capable of demonstrating self-starting dynamics for noise-like input parameters, finalising the model development. The starting pulse was defined as quantum noise using the one photon per mode per polarization state approach, with a 25 fJ pulse nested within it in order to reduce by an order of magnitude the required number of roundtrips for a modelocked solution to stabilise.

Table 3.2 details the user-defined input parameters which were common for all vectorial modelocking simulations in this chapter. The central wavelength (λ_c) was set to

Parameter	**Value**
λ_c	1060 nm
$\Delta\lambda$	1 nm
C	0
λ_g	1060 nm
$\Delta\lambda_g$	100 nm
G	2.9 m^{-1}
E_{sat}	0.8 nJ
$\mathrm{GVM_y}$ ($\beta_{1,y}$)	-5 fs/m
Rep. rate, R	40 MHz
Average power, P_{ave}	1 μW (25 fJ pulse energy)
Field	$(0.94P_{\mathrm{ave}}/(RT_{\mathrm{FWHM}}))^{0.5}\exp\left[-((1+iC)/2)(t^2/t_0^2)\right]$

TABLE 3.2: Common input pulse parameters for the stable vector modelocking simulations.

Paramter	**Single wavelength value**	**Multi-wavelength value**
$\mathrm{QWP_{NPE}}$	$-1.7\pi/3$	$-1.8\pi/3$
$\mathrm{HWP_{NPE}}$	$1.37\pi/3$	$1.55\pi/3$
$\mathrm{QWP_{IN}}$	$1.2\pi/4$	$\pi/4$

TABLE 3.3: Waveplate angles for the stable single and multi-wavelength operation of the vector cavity model.

1060 nm, and the bandwidth ($\Delta\lambda$) was chosen to be 1 nm as the corresponding time-domain pulse width matched other peaks in the noise-like starting field. This initial field had no chirp ($C = 0$) to minimize the influence of the starting pulse, which was included only to reduce computation time. For simplicity, the gain peak (λ_g) was again centred at the central wavelength of the pulse, and the bandwidth ($\Delta\lambda_g$) was set to be large enough to include the experimental pulse spectrum. The small signal gain coefficient, G, and the maximum extractable energy, E_{sat}, were chosen so that the output powers of the experimental and simulated cavities were similar. A relative group velocity mismatch (GVM) between the polarization axes was used to simulate the fibre birefringence, and was set to -5 fs/m for the fibre y-axis. The repetition rate (R) was set to match the experimental cavity, and the average power of the starting pulse was set to 1 μW, corresponding to a pulse energy of 25 fJ. Again, the input field was assumed to be Gaussian. Starting pulses in the atto-Joule range were found to produce similar results, but the pulse stability degraded with increasing roundtrip number due to vector modulation instability [87, 88], indicating a smaller margin of error in the choice of waveplate angles.

The waveplate angles for single and multi-wavelength operation of the simulated cavity are given in Table 3.3. No other parameters were changed when moving from one stable modelocking regime to another. These angles do not correspond to those used experimentally as the effect of the fibre birefringence was truncated to a group velocity

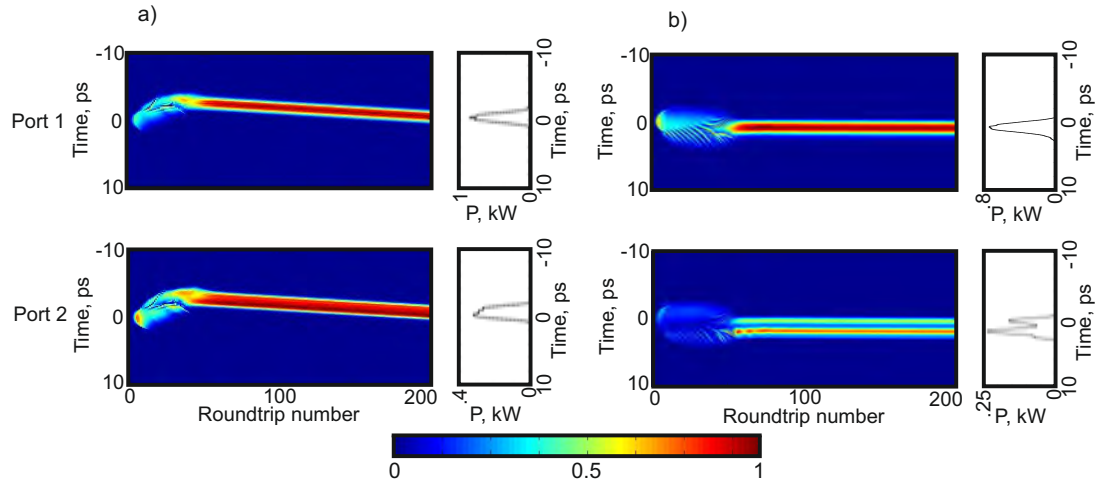

FIGURE 3.10: Simulations showing the initiation of stable modelocking solutions for the simulated breathing pulse cavity. a) Single-wavelength dynamics from both ports 1 (upper) and 2 (lower). b) Single- (port 1, upper) and multi-wavelength (port 2, lower) operation, as seen for the experimental cavity.

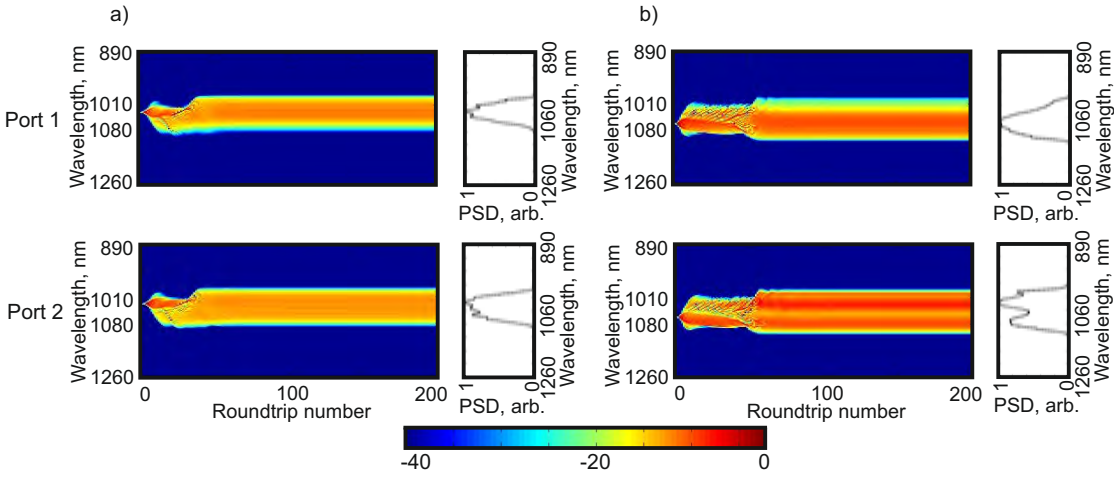

FIGURE 3.11: Simulations showing the initiation of stable modelocking solutions for the simulated cavity, expressed in the wavelength domain. a) single-wavelength, and b) multi-wavelength operation. The two pulses present in the output from port 2 correspond to a double-peaked spectrum similar to that in figure 3.2. The colourmap corresponds to the normalized power spectral density in dBm/nm.

mismatch in the simulations. The birefringence and the orientation of the fibre axes with respect to the waveplates, the discontinuities in the birefringence at each splice of the non-PM fibre, and the dispersion of the birefringence were not known for the experimental cavity. As such, these characteristics could not be taken into account in the simulations. This, however, allowed for the effect of XPM on the pulses to be isolated from other effects such as linear Lyot filtering, and prevented extra calculation to remove the linear polarization evolution when examining the effect of XPM on the polarization state. For the case of multi-wavelength operation it is important to note that full circular polarization was required at the input to the fibre section to maximize XPM between

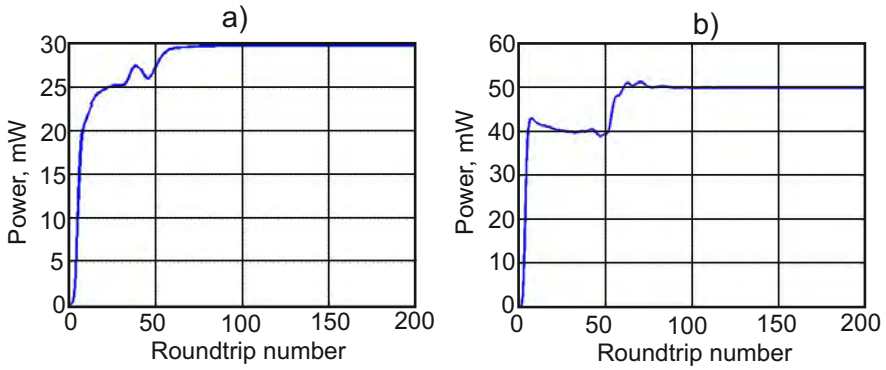

FIGURE 3.12: Simulations showing a) Power evolution as a function of roundtrip for the single-wavelength operation of the simulated cavity directly after the fibre section (before the polarization selective optics). b) The same, but for the multi-wavelength operation.

the two polarization components as they propagate through the fibre. Reducing the ellipticity of the field at this point in the cavity causes the pulses to remain intact in both the spectral and the time domain.

The evolution of the time domain traces at ports 1 and 2 as a function of roundtrip number are shown in figures 3.10a and 3.10b for single and multi-wavelength operation, respectively. Self-starting from noise-like starting pulses is observed for both modelocking solutions. The single-wavelength operation results show that the pulses emitted from ports 1 and 2 are very similar, with a single peak in the time domain. The negative linear gradient is the result of a linear phase delay imparted by the waveplates. For the multi-wavelength case (Fig. 3.10b), the model reproduces the dynamics observed in the experimental cavity design, and the time-domain traces show a chirped equivalent of the PICASO pulse reconstructions in figure 3.4. The line-outs to the right of each density plot show the optical intensity in the time domain for the 200^{th} roundtrip, and are included for clarity. The simulations also reproduce the stability observed for the experimental cavity, indicating that the pulses remain coherent over many cavity roundtrips.

Figures 3.11a and b show the development of stable modelocking in the wavelength domain, for the same simulation and input parameters which produced the data shown in figures 3.10a and b. As expected, the single-peak pulses emitted from ports 1 and 2 in the time domain traces correspond to smooth spectra (Fig. 3.11a), whereas the single- and multi-wavelength time domain solutions correspond to single- and multi-peaked spectra, respectively (Fig. 3.11b). The two pulses seen in the output from port 2 in the simulated time domain traces therefore correspond to different central wavelengths, as was seen in the experimental data presented in section 3.3. These simulations suggest that the increased ellipticity of the pulse at the input to the cavity fibre section is responsible for the spectral modulation, giving the multi-wavelength modelocking state.

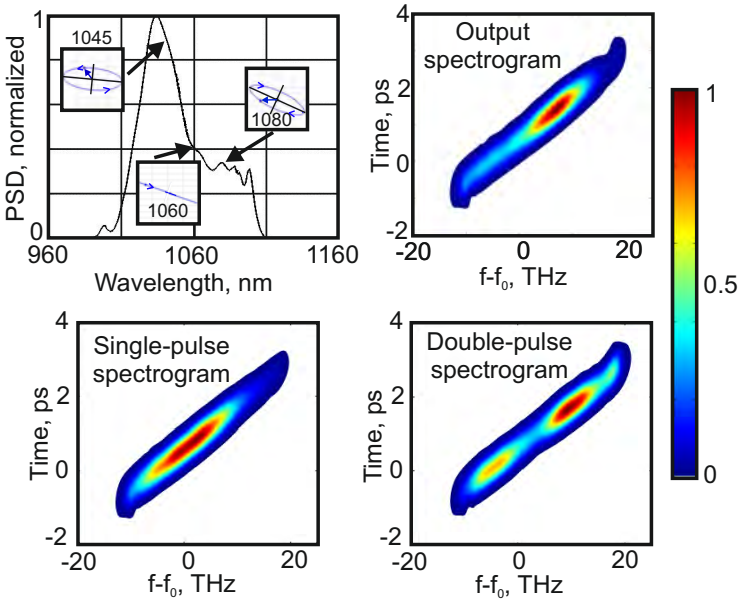

FIGURE 3.13: Top left: Simulated spectrum of the multi-wavelength modelocked pulse after the QWP and HWP before port 1 for the 200$^{\text{th}}$ cavity roundtrip. The insets show the polarization state for three different wavelengths. The fibre propagation axis is directed out of the page. Top right: Spectrogram of the same pulse on a linear scale, showing the wavelength to time mapping for the pulse. Bottom left: Spectrogram of the single-pulse emitted from port 1. Bottom right: Spectrogram of the double-pulse emitted from port 2. The colourmap is normalized to the maximum value for the spectrograms ($\Delta f = 42$ GHz, and $\Delta t = 7$ fs).

The output power as a function of roundtrip number during the onset of modelocking for the single- and multi-wavelength states is shown in figures 3.12a and b. This power was taken at the output of the cavity fibres before the waveplates at port 1. The circulated power stabilizes for both solutions after approximately 80 roundtrips, with the multi-wavelength case showing a higher circulated power of 50 mW, close to the calculated value of 47.2 mW for the same point in the experimental cavity. This indicates that the roundtrip nonlinear phase will be higher for the multi-wavelength case which, in conjunction with the increased ellipticity of the pulse at the input to the cavity fibres, confirms that the effect of XPM between the two polarization states is higher for the multi-wavelength modelocking solution.

It is necessary to examine how XPM acts in conjunction with chirp to split the circulated pulse into two along one polarization axis. The spectrogram in the top right of Fig. 3.13 shows the wavelength to time mapping for the pulse, as measured at the fibre section output. A strong linear up-chirp is seen, and maps frequency (or equivalently, wavelength) to the time domain. Through this map, the intensity distribution, and therefore the accumulated nonlinear phase, may be viewed as a function of wavelength rather than time. This results in a wavelength dependent nonlinear polarization evolution, which is shown in the top left plot of figure 3.13. The increased cross-phase modulation acting in conjunction with the pulse chirp and the waveplates has resulted

in a linear polarization state around the central wavelength of 1060 nm. This section of the spectrum can be ejected from the cavity at port 1, leaving the minimum in both the time and spectral domains around 1060 nm at port 2 (figures 3.10b and 3.11b). After the waveplates, the field is elliptically polarized at the extremes of the spectrum with short wavelengths having counter-clockwise elliptical polarization and long wavelengths having clockwise. It is not possible to achieve 100% output coupling of an elliptical state with a PBS, so some of the power continues on to port 2 to form the two spectral peaks. This is demonstrated by the spectrograms in the bottom row of figure 3.13. The port 1 spectrogram is formed of a positively chirped single spectral peak, and the port 2 multi-wavelength spectrogram is formed of a positively chirped spectrum with two peaks.

Considering the polarization state at the input to the fibre section, intra-cavity power, and pulse chirp required for the multi-wavelength modelocking state, it is therefore concluded that it is the result of over-driven cross-phase modulation acting on a normally dispersed pulse to induce a wavelength dependence of the polarization state.

3.5 Discussion

Given the good measured cavity stability, the required output power, self-starting dynamics and suitable spectral coverage around 1045 nm, port 1 from this oscillator could be used to seed the fibre CPA system. It should be noted that the noise performance of breathing-pulse lasers has been shown to depend on the precise choice of net dispersion in the cavity [89] but this secondary point is not the focus of the current chapter and therefore we have not attempted to optimize the laser for zero net dispersion operation.

A wavelength filter driven by NPE was identified as the mechanism for the multi-wavelength dynamics. It should be noted that it was only possible to draw a qualitative comparison between the experimental cavity output and the circulated pulses in the simulations. However, a good match between experiment and simulation can be obtained for a single pass of the fibre section with idealized parameters. This is shown in figure 3.14, and the parameters used for this simulation are given in Table 3.4. The spectral minimum in both data sets matches well, and the two spectral maxima correspond to the satellite peaks seen in the autocorrelation. This simulated solution was not stable for more than a single roundtrip, however, and this may be the result of a number of assumptions made when constructing the cavity model. For example, the cavity birefringence was idealized by reducing its effect to a group velocity mismatch, and the dispersion was assumed to be the same for both birefringence axes. In the experimental cavity, the fibre birefringence will cause the polarization state of the pulse to change during propagation, changing the behaviour of the XPM term in equation 2.27.

Discontinuities in the birefringence will also exist at the splice points of the experimental cavity, and these have been neglected in the simulations. These parameters will have a significant effect on the pulse shape and polarization state over many roundtrips which is not reproduced in the simulations.

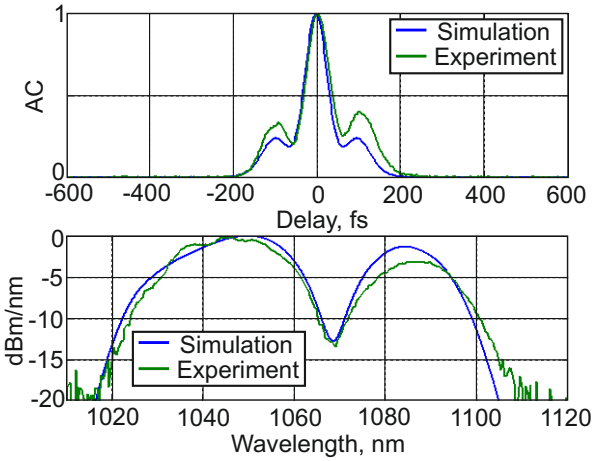

FIGURE 3.14: Comparison between simulated (blue) and experimental (green) data. The simulated data shown here was produced by modelling a single pass of the fibre section of the cavity with idealized input pulse parameters.

Parameter	**Value**
λ_c	1060 nm
$\Delta\lambda$	1 nm
C	-6
λ_g	1060 nm
$\Delta\lambda_g$	100 nm
G	6 m^{-1}
E_{sat}	2.1 nJ
GVM_y ($\beta_{1,y}$)	-26 fs/m
Rep. rate, R	40 MHz
Average power, P_{ave}	690 μW
Field	$(0.94P_{ave}/(RT_{FWHM}))^{0.5} \exp\left[-((1+iC)/2)(t^2/t_0^2)\right]$

TABLE 3.4: Input parameters for the single-pass simulations used in the comparison with experimental data.

Considering the multi-wavelength cavity dynamics, a number of different mechanisms for generating multi-wavelength pulse trains have been proposed recently. Luo, et al. [90] included a linear tunable Lyot filter to form up to four frequency bands near 1580 nm with bandwidths of approximately 0.75 nm in an Er-fibre oscillator. The spacing of the wavelength bands for this design was flexible, and determined by the filter. Similarly, intra-cavity birefringence was attributed to the observation of stable, dual-wavelength dissipative solitons in a figure-of-eight cavity [91]. The pulses had bandwidths of around 10 nm and central wavelengths of 1572 and 1587 nm. The smoothness of the pulse phase

profile was not demonstrated as the output pulses were not externally compressed, and simulations were not included to isolate the cavity birefringence as the mechanism responsible for the observed dynamics.

In addition to Lyot filtering and cavity birefringence, novel saturable absorption mechanisms have also been used. Liu, et al. [92] use a broadband carbon nanotube saturable absorber to encourage the development of modelocked pulses for a wider range of wavelength bands than would be achieved with conventional saturable absorbers, such as semiconductor saturable absorber mirrors. Fibre Bragg gratings were also used to provide differential feedback for selected wavelength bands, and 5.9 ps pulses with bandwidths of 0.49 nm were produced with central wavelengths of approximately 1539.5, 1549.5, and 1559.5 nm.

The multi-wavelength oscillator described in this chapter emits pulses which are orders of magnitude shorter than others in the literature, leading to correspondingly broader bandwidths. Although this is not a requirement for the fibre CPA, potential uses could include time-resolved spectroscopy and super-resolution imaging. Additionally, the cavity simulations allowed for a good understanding of the mechanism responsible for the cavity dynamics which, to the best of my knowledge, has not been presented before in the context of multi-wavelength oscillators.

3.6 Summary

In this chapter, the oscillator used to seed the fibre CPA system was described. A breathing pulse ring cavity was chosen due to the more suitable noise characteristics in comparison with other cavity designs, which was beneficial for the stability of the current fibre CPA design and will aid in possible carrier-envelope phase locking in future work. The pulses had a maximum bandwidth of 72 nm at the 10 dB level and were shown to be compressible down to 47 fs. PICASO reconstructions of the pulses showed that a flat temporal phase could be achieved with external compression, and the fundamental and 20th harmonics of the RF spectrum were used to demonstrate the good cavity stability. Additionally, the novel multi-wavelength cavity dynamics were described and simulations allowed for the nonlinear mechanism which drives this effect to be understood, allowing for a better understanding of the dynamics of breathing-pulse lasers. Although the multi-wavelength modelocking state is not required by the fibre CPA system, it was found that the cavity was most stable and demonstrated the most reliable self-start modelocking when operating in this regime. As such, the output from port 1 of the multi-wavelength oscillator was used to seed the fibre CPA system because of the good bandwidth and output power at the appropriate operating wavelength of 1045 nm.

Chapter 4

Yb^{3+}-doped fibre laser chirped pulse amplification system

4.1 Introduction

This chapter describes how an existing fibre CPA system design was converted to a new wavelength to optimize the performance of the final power amplifier so as to allow for average power scaling, as well as to improve the stability. The previous system, documented in refs. [29, 30] had output specifications of 300 fs, 100 μJ pulses at 16.7 kHz repetition rate and a central wavelength of 1055 nm, and was shown to be capable of generating high harmonics [31]. However, ASE buildup at 1030–1040 nm in the final amplifier led to self-Q-switching, repeatedly damaging the facets of the gain fibre and occasionally even causing damage to the preceding amplifier. Shortening the central operating wavelength of the system to better match the gain peak of the final amplifier therefore presented a clear route for potential repetition rate and average power scaling, as well as for improving the OSNR, and a target wavelength of 1045 nm and 10 dB spectral width ranging from 1038–1052 nm was selected as the dielectric stretcher and compressor grating efficiency was reduced at wavelengths less than 1035 nm. In addition, shot-to-shot stability was also to be improved by fiberizing the majority of the amplifier chain, and long-term stability was improved by using grating stabilized pump diodes and water cooling the signal launch in the final amplifier. The design changes for each component of the new system made necessary by the new operating wavelength are described below.

- The oscillator. This was built in-house as commercial oscillators at 1045 nm are not available. The output from port 1 of the oscillator described in chapter 3 was used.

- The dielectric grating based bulk stretcher and compressor. The overall stretcher design remained similar to the previous system [29, 93]. Numerical work for the realignment was done by Dr. Jonathan Price, and the realignment was done by Dr. Price and myself.

- The pre-amplifier configuration. All components from the previous amplifier chain were screened at the new wavelength. Once rebuilt and spliced back together to form the pre-amplifier chain, the Yb-doped fibre lengths were shortened and pump powers were adjusted iteratively to give the required output OSNR.

- The first power amplifier. This was fully fiberized by incorporating a pump combiner with a single-mode PM signal throughput at the amplifier input, eliminating previous drifts in pump alignment which was previously done using dichroic mirrors. This involved endcapping and polishing the fibre facet to prevent damage and optimizing the fibre length for a new 7 W 975 nm pump diode instead of a 915 nm pump diode as used previously.

- The final amplifier. An endcapping routine and improved endcap length were found for increased resilience to facet damage. The signal launch was water cooled and shielded from scattered pump light for improved thermal stability. Free-space pump and signal coupling was used to minimize the fibre path length and nonlinear distortion.

Once completed, the 100 μJ, 350 fs output pulses had a clean temporal and spectral profile at 16.7 kHz repetition rate with diffraction limited beam quality and minimal gain narrowing. Details are provided in the following sections. Both long-term measurements of the average power and shot-to-shot pulse energy measurements were taken and showed that the system was highly stable so the improved performance was successfully achieved. The main system limitation for average power scaling was found to be photodarkening in the commercial gain fibre used in the final amplifier, which had not been expected and was possibly due to the change to a volume Bragg grating stabilized pump diode that created higher Yb ion inversion levels than had been achieved with the previous pump diodes, which were not wavelength-locked precisely to the 975 nm Yb absorption peak. A new photodarkening-resistant amplifier may be needed in the future.

This chapter is structured as follows. An overview of the system is given in section 4.2, before the fibre CPA performance is discussed in section 4.3. Potential improvements and future work are discussed in section 4.4 before the chapter is concluded in section 4.5.

4.2 System Overview

Figure 4.1 shows a schematic of the fiber CPA system, which was fully fiberized from the stretcher output through to the final amplifier.

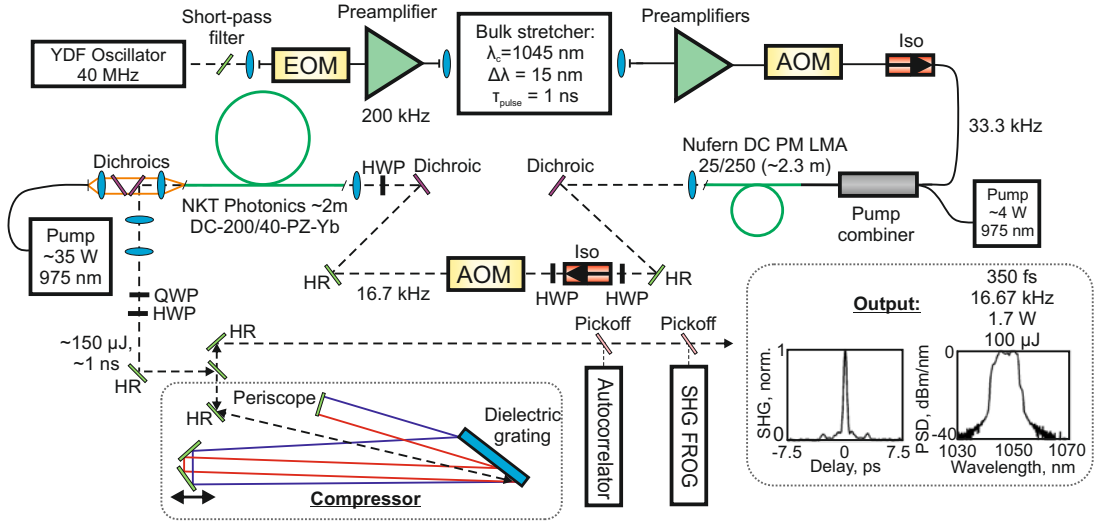

FIGURE 4.1: Schematic of the fiber CPA system. Inset: Autocorrelation and spectral data.

The seed laser at the front of the system was an Yb-doped fiber breathing pulse ring cavity oscillator similar to those reported in refs. [94, 95], and was described in detail in chapter 3. A 1053 nm hard-edged short-pass filter cut the bandwidth of the oscillator to concentrate energy extraction from the amplifiers in the spectral region transmitted through the stretcher and compressor.

At the output of the oscillator the pulses were launched into a fiberized electro-optic modulator (EOM), reducing the repetition rate to 200 kHz as this was found to give a good balance between gain and optical signal-to-noise ratio (OSNR) in the pre-amplifiers. The DC bias voltage applied to the EOM was controlled by a feedback loop (not shown in figure 4.1) which continuously maximized the EOM extinction ratio to prevent thermally related drifts. Feedback was provided by a 20 dB tap in the pre-amplifier chain connected to a photodiode. The feedback loop maximized the photodiode peak voltage to maintain good energy extraction within the pulse transmission window without allowing satellite pulses to deplete the amplifier gain, which was critical for obtaining sufficient pulse energy from the pre-amplifiers to saturate the power amplifiers.

Following the EOM, a fiberized booster amplifier which was core pumped by a 975 nm diode was used to maintain good OSNR after the 200-fold power reduction commensurate with the reduced repetition rate. A bulk stretcher followed, and this had a standard design [93] (used previously in refs. [29, 30]). The stretched pulse duration was 1 ns at intensity FWHM, and the stretcher transmission window was 14 nm (edge-to-edge) with

a central wavelength of 1045 nm, chosen to enable the final amplifier to operate with high gain per unit length with minimal gain narrowing.

Parameter	**Nufern 5/130**	**Nufern 25/250**	**NKT 40/200**
Core diameter (μm)	5	25	40
Core NA	0.12	0.06	0.03
Pump cladding diameter (μm)	-	180	200
Pump cladding NA	-	0.46	0.6
Dopants	Yb/Al/Si	Yb/Al/Si	Yb/Al/Si
Core V-number	1.8	4.5	-
Pump absorption at 976 nm (dB/m)	>100	5.1	10
Slope efficiency (estimated)	75%	75%	∼11%
Effective mode area (μm^2)	30	300	760 ± 100
Saturation energy (μJ)	18	110	265
Typical device length (m)	1-2	2-3	2
Bend radius (cm)	2-3	5	20
M^2 in amplifier configuration	1	1.1	<1.1

Table 4.1: Fibre parameters for each amplification stage.

The fully fiberized pre-amplifiers (details given in column two of Table 4.1) were made using Nufern 5/130 Yb-doped fibre which was core pumped using fibre-coupled 975 nm diodes and telecommunications grade wavelength division multiplexed (WDM) pump couplers in a forward pumped geometry. Each pre-amplifier had an optical isolator at the input to prevent counter-propagating ASE from either depleting the gain or causing any damage in the preceding amplifiers. Typically, the pre-amplifiers used a 2 m length of Yb-doped fibre, which was found to be optimal for achieving low noise and nonlinearity while matching the gain bandwidth to the signal. The pre-amplifier chain had an output OSNR of 10 dB as measured from the spectrum, i.e. including ASE arriving between pulses in the time domain.

A fiberized acousto-optic modulator (AOM) and isolator at the output of the pre-amplifiers then cut the repetition rate to 33.3 kHz and increased the OSNR to approximately 40 dB before transmission into the first power amplifier. The amplifier was constructed using 2.3 m of Nufern DC 25/250 fibre (NA=0.06 and 0.46 for the core and pump cladding, respectively), and was forward pumped with a fiberized 4 W, 975 nm diode using a fiberized multi-mode pump combiner with single-mode signal fibre throughput (column three of Table 4.1). The output facet of this amplifier was polished to an angle of 5 degrees to avoid optical feedback into the core.

A short-pass dichroic filter removed residual pump light after the first power amplifier. A free-space isolator and AOM were used to remove from the beam path backward propagating ASE originating from the final amplifier and to cut the repetition rate to

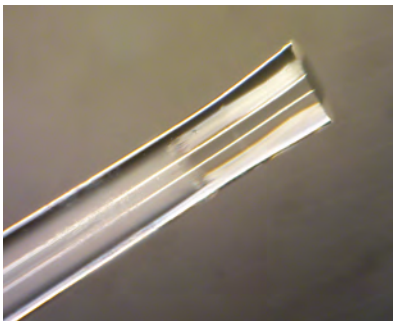

FIGURE 4.2: Microscope image of the endcap at the signal input of the final amplifier, formed in solid-core air-clad PCF by collapsing the air structure.

16.7 kHz. A half waveplate was used to maximize the AOM diffraction and a short-pass dichroic mirror was used to remove short-wavelength ASE and residual backward-propagating final amplifier pump light. The translation stage at the input to the final amplifier was water cooled for improved long-term stability (Not shown in figure 4.1).

The final amplifier used a 2 m length of commercially available, single-mode, single polarization Yb-doped PCF (NKT Photonics DC-200/40-PZ-Yb, column four of Table 4.1) with a core diameter of 40 μm and an effective mode-field area of 760 μm^2. For long-term stability, the amplifier had endcapped and angle polished input and output facets to prevent feedback, and the endcap at the signal input required replacement due to damage. I developed the following new endcapping procedure for air-clad fibres (with advice from others in the Pulsed Fibre Lasers Group with experience in endcapping other fibre types), and the result is shown in figure 4.2:

1. Cleaving the fiber with a CO_2 laser cleaver to give a flat facet.
2. Collapsing the double-clad air-hole PCF structure using a hot filament-based glass processor (Vytran GPX-3000), taking care to adjust the filament heating and position parameters to prevent bubbling.
3. Cleaving the endcap to the correct length using the CO_2 laser cleaver
4. Hand polishing the facet to remove the slight bulge created by the CO_2 cleaver,thus creating an optically flat surface with an angle.

The procedure was optimized to eliminate bubbling and distortions in the fibre shape while the fibre structure was being collapsed. It was found that an endcap length of 800 μm provided a good balance between signal launch efficiency and mode expansion for the counter-propagating ASE, thus preventing facet damage.

The PCF was bent to a radius of 20 cm as recommended by the manufacturer to provide polarizing operation, and was backward pumped using a 35 W, 975 nm diode. The amplifier output was collimated to 3.3 mm ($1/e^2$ intensity radius) for transmission

through the compressor. Due to an initial period of use at high power in a previous experiment, this particular fibre had suffered photodarkening [96] and the associated excess losses resulting in the low overall conversion efficiency of approximately 11% (compared to launched pump power) observed here. Despite this pre-existing photodarkening related loss, the fibre operation remained highly stable during use in the fiber CPA system as illustrated by the long-term power data shown in section 4.3 below. Photodarkening is not an inherent limitation associated with the PCF structure, and it has been largely eliminated in the current version of this fibre which provides pump to signal conversion efficiency between 50–70% according to the manufacturer's specifications.

A dielectric grating compressor was used at the output of the amplifier chain [32]. The grating width was 35 cm, and the groove density was 1740 lines/mm. The compressor used four passes of the grating and resulted in an edge-to-edge spectral width of 12 nm, throughput efficiency of 65%, and a system polarization extinction ratio of 27 dB.

4.3 System Performance

The pre-amplifier output pulse energy (before the first AOM) was 90 nJ. The fiberized AOM throughput efficiency together with the isolator and pump combiner insertion losses led to a seed energy of 30 nJ input to the first power amplifier and the output pulse had ∼3 μJ energy. The output OSNR was 23 dB, and a fibre bend radius of 5 cm was used to achieve a single-mode output beam with $M^2 = 1.1$ for this amplifier. The free-space AOM diffraction efficiency reduced the pulse energy to 1.5 μJ and increased the OSNR to 30 dB by removing ASE between pulses. The seed pulse energy launched into the final amplifier was estimated to be 1 μJ and the output pulse energy was 155 μJ (21.8 dB gain) with an OSNR of 14 dB. As is commonly the case with fibre systems, nonlinearity, not energy storage, limited the maximum pulse energy. We calculated the saturation energy at a wavelength of 1045 nm using typical parameters for aluminosilicate fibre [39] to be 265 μJ for this amplifier, giving $E/E_{\text{sat}} = 0.56$. Saturation related gain shaping is therefore not expected to be significant.

The top left and right plots of figure 4.3 show the spectral evolution throughout the system on a logarithmic and linear scale, measured at the output of the bulk stretcher, the amplifier chain, and the compressor. The spectral resolution is 0.05 nm for all plots (measured using a Yokogawa AQ6370C optical spectrum analyser). Gain-narrowing and dragging were minimal effects, and the latter measured just 1 nm (spectral FWHM) for the entire amplifier chain. This was achieved by tuning the gain of the amplifier chain by appropriately varying the Yb-fibre lengths and pump powers. The result was a reasonably flat spectrum at the compressor output (measured at the 3 dB level). The 3 dB

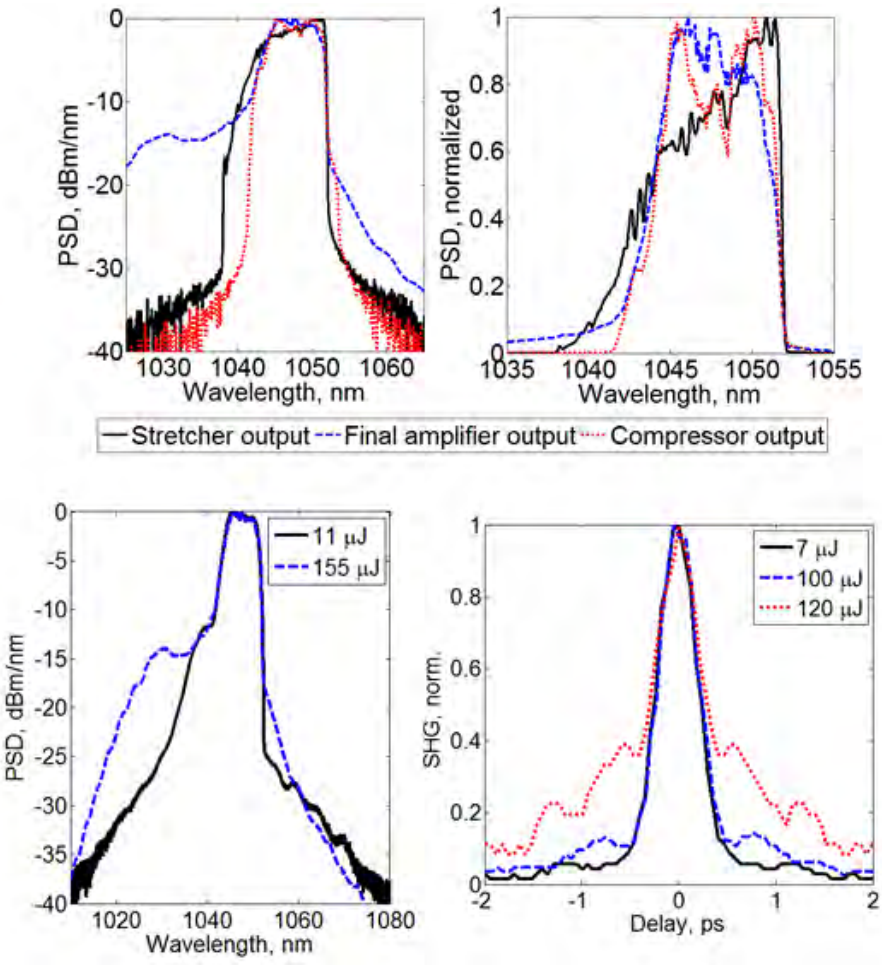

FIGURE 4.3: Top left: Spectra from three different points in the fibre CPA system: output of stretcher, output of final fibre amplifier, output of compressor. (See legend below graphs.) Top right: Spectra on a linear scale. Bottom left: Spectra at the output of the final amplifier for low and high amplifier output pulse energies. Bottom right: Compressed pulse autocorrelation traces for increasing pulse energies.

spectral widths measured 9 nm for the stretcher, and 8 nm for the final amplifier and compressor (edge-to-edge width of 12 nm). The OSNR at the output of the compressor was 30 dB. Very little fine-scale modulation is seen in the spectra, even on a linear scale. This is likely to be a result of using PM fibres for the whole amplification chain because the architecture avoids satellite pulses that can be amplified through cross-phase modulation the final fibre. The spectra at the output of the final amplifier for low and high pulse energy operation are shown in the bottom left plot of figure 4.3, highlighting again the lack of spectral modulation and the low level of ASE from the final amplifier.

It was found that seeding the final amplifier with high pulse energies from the first power amplifier led to a significant autocorrelation pedestal at rather low output pulse energies (40 μJ). Therefore the final amplifier input was reduced to the minimum possible pulse energy commensurate with a good OSNR for 100 μJ compressed pulse energy to reduce the nonlinear length of the amplifier. The resulting output is shown in the

bottom right plot of figure 4.3, which shows autocorrelation traces (measured with an APE PulseCheck 15) for compressed pulse energies of 7, 100, and 120 μJ (corresponding pulse energies at the final amplifier output: 11, 155, 184 μJ). The plot shows that nonlinear distortion limits further pulse energy scaling. Prior to performing this measurement, the compressor grating angle was first set to the design position for linear dispersion compensation, then autocorrelation measurements were recorded at 100 μJ pulse energy. Using the shortest pulse duration and lowest autocorrelation pedestal as a target, small adjustments were made to the compressor input angle and grating separation to iteratively tune the compressor dispersion profile. This partly compensated for the effects of SPM in the final amplifier and resulted in an estimated final pulse duration of 340 fs from the autocorrelation data, assuming a Gaussian pulse shape. The transform limited pulse duration was 224 fs as calculated from the compressed pulse spectrum (figure 4.3, top row, red dotted line). The 100 μJ pulses were therefore 1.51 times transform limited.

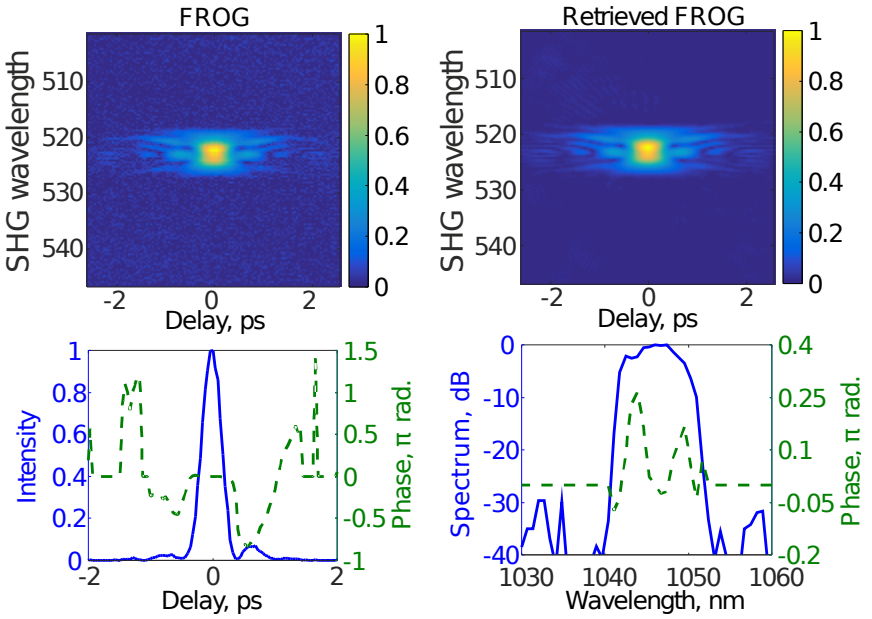

FIGURE 4.4: Top row: SHG FROG spectrograms. Left: Measured. Right: Retrieved. Bottom row: Reconstructed pulse intensity and phase (solid blue and dashed green lines, respectively). Left: Temporal domain. Right: Spectral domain.

With the system operated as shown in figure 4.3, the vast majority of the accumulated nonlinear phase occurs in the final amplifier. The calculated B-integral (equation 2.21) for the optical path to the launch into the final amplifier was 0.18π radians. For the final amplifier, the corresponding estimated B-integrals were 0.48π, 3.68π, and 4.26π radians for 7, 100, and 120 μJ compressed pulse energies, respectively. The peak power of the 1 ns pulses at the output of the final amplifier is 155 kW, which is well below the estimated Raman threshold power for the final amplifier (equation 2.23, 275 kW for

1 ns pulses, corresponding to a pulse energy of 275 μJ, or 4.6 W average power for a repetition rate of 16.7 kHz) [67].

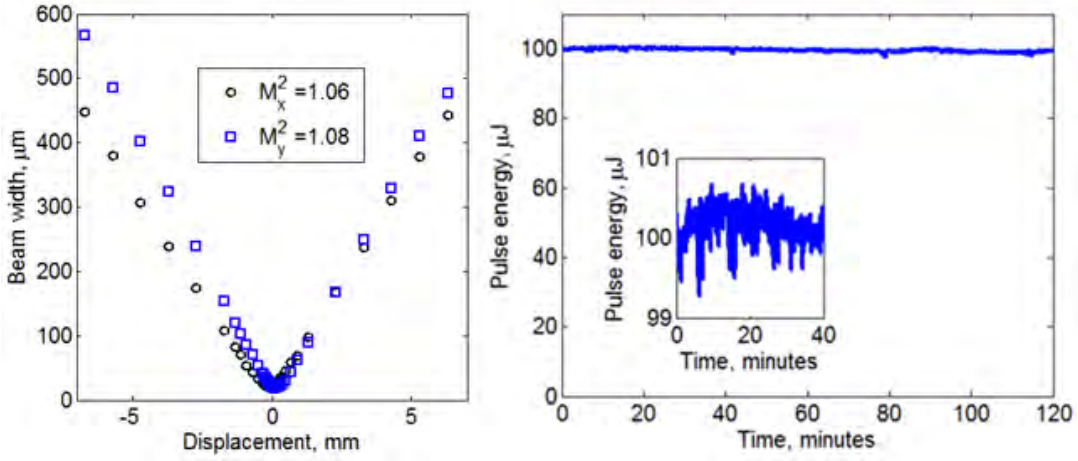

FIGURE 4.5: Left: Beam caustics for the fibre CPA system, measured after the compressor. The average M^2 was 1.07. Right: Long-term pulse energy after the compressor. The data set shows a mean pulse energy of 99.8 μJ (standard deviation of 0.45 μJ). Inset: Power stability data plotted with just $\pm 1\%$ scale on the y-axis for the first 40 minutes after switching on the final amplifier.

The pulse duration of 340 fs estimated from the autocorrelation data was confirmed by direct measurement using SHG FROG (MesaPhotonics FROG Scan). figure 4.4 (top row) shows the measured FROG traces for the 100 μJ output pulses. The raw data was taken with a temporal resolution of 20 fs and a spectral resolution of 0.08 nm, before interpolation onto a 256×256 grid with a time span of 5 ps, 20 fs temporal resolution, a frequency span of 51.2 THz (187 nm) centred at 286.2 THz (1048.2 nm) with a resolution of 0.2 THz (0.73 nm). The close agreement between the measured (top left) and retrieved (top right) FROG traces produced a FROG error of 0.0049. The bottom row of Figure 4.4 shows the reconstructed intensity and temporal phase (left), and the reconstructed spectrum and spectral phase (right, logarithmic scale for the spectrum). The intensity trace shows a pulse duration of 350 fs at intensity FWHM. The sign of the delay axis for this pulse retrieval is ambiguous due to the nature of SHG FROG. The phase across the central pulse peak is approximately flat, but the spectrograms clearly show evidence of satellite pulses outside of the main pulse, which could be due to the nonlinear phase distortions as the autocorrelation pedestal is clearly reduced at lower pulse energies. The peak power of the pulses was calculated to be 240 MW from the FROG reconstructed intensity profile.

The beam caustics used for an M^2 calculation are shown to the left of figure 4.5. The spatial beam profile was diffraction limited, with an average M^2 value of 1.07 (1.06 and 1.08 in the x- and y-directions, respectively). As this data was taken after the compressor it provides confirmation of the good alignment of all compressor optics as a

misaligned compressor would degrade the beam quality [97].

The right-hand plot of figure 4.5 shows the long-term stability of the system, measured over a two hour period at a sample frequency of 1 Hz using a ThorLabs S145C integrating sphere with an InGaAs power sensor. The detector bandwidth was set to 15 Hz so that the measurement was averaged over approximately 100 pulses. The mean pulse energy was 99.8 μJ with a standard deviation of 0.45 μJ. The absolute minimum and maximum outliers over the measurement were 97.8 μJ and 100.7 μJ.

Shot-to-shot pulse energy variation was measured at the output of the compressor by using a 2 GHz detector (EOT ET3000 InGaAs) and comparing the peaks of the diode output pulses on an oscilloscope. Over 30,000 samples it was found that the pulse energy had a standard deviation of $< 1\%$, with an absolute minimum and maximum pulse energy of 95 and 103 μJ.

4.4 System improvements and future work

Technical benefits to system stability could be realized by fully fiberizing additional components and thus eliminating potential alignment drifts associated with most free-space setups. Using a chirped fibre Bragg grating (CFBG) [32] and fiberized circulator for the stretcher (or a specially designed combination of stretcher fibres with dispersion matched to the compressor as was done in ref. [98]) would enable complete integration at the system front end. In addition, a fiberized final amplifier has become possible since the launch of a commercialized pump combiner, which may be spliced onto the NKT DC-200/40-PZ-Yb fibre that was used for the final amplifier. A new length of this fibre would also benefit system efficiency which, alongside higher power pump diodes for the power amplifiers, would enable repetition rate and average power scaling.

Recently, peak power scaling to multiple gigawatts at high repetition rates and high energies has been made possible by using coherent combination of the final amplifier fibres [19], divided pulse amplification [99, 100], nonlinear compression in gas-filled or Kagome fibres [26, 101, 102] followed by dispersion compensation using chirped mirrors for sub-100 fs pulses, or a combination of each. So far, these methods have only been attempted with ultrafast systems which use rod-type fibres in the final amplifiers as opposed to flexible, although there are no inherent differences between the two approaches which would render these methods inapplicable to flexible fibre systems. As such coherent combination, divided pulse amplification, and nonlinear compression form a viable route to average and peak power scaling of the fibre CPA presented in this chapter, and the excellent system stability would help to simplify their addition to the system. This, alongside the dielectric grating compressor, will allow for average power scaling up to at least 100 W [32] in a compact, and highly stable setup. Additionally, active phase

stabilization as used in ref. [30] is a possibility for further improving the autocorrelation shape and FROG trace, and potentially allowing for increased pulse energy before detrimental nonlinear distortion destroys the pulse shape.

4.5 Summary

Improvements to the stability of an existing fibre CPA system were documented in this chapter, and were achieved by changing the operating wavelength to better match the gain peak of the amplifier chain, which was also fiberized for the majority of its length. The process involved realigning the stretcher and compressor, rebuilding the amplifier chain and optimizing gain, nonlinearity and dispersion management thoughout the system. It was found that nonlinearity limits the current maximum pulse energy of the system rather than energy storage, and suitable methods for increasing the pulse energy were discussed. The system produced 100 μJ, 240 MW peak power pulses with shot-to-shot and long-term standard deviations in pulse energy measuring $<$1% and 0.45 μJ, respectively. The diffraction limited beam quality indicates that these pulses can be focussed to intensities of approximately 1×10^{18} Wm^{-2} and are therefore suitable for frequency conversion into the XUV through high-harmonic generation.

Part II

XUV generation and characterization

Chapter 5

An introduction to high-harmonic generation

This chapter introduces the theory of HHG in both a semi-classical (section 5.1) and quantum mechanical (section 5.2) single atom framework. The effect of pulse duration on the resulting XUV characteristics are also described using the quantum mechanical approach. Different generation methods are described in section 5.3 before phasematching and the efficiency of the XUV generation process are considered in section 5.4.

5.1 The semi-classical model

First introduced by Corkum [103], the semi-classical description of HHG has seen remarkable success due to its intuitive nature and accuracy in predicting experimental results, such as the highest available (cut-off) harmonic frequency. The model assumes that only the outermost electron is involved in the interaction with the driving field and, with the exception of the tunnel ionization process, that both the field and the electron may be treated in a classical framework.

Figure 5.1 [31] illustrates the physical processes which make up Corkum's 'three-step' model. The distortion of the atomic Coulomb potential by an intense driving field allows for the tunnel ionization of the outer-most electron (a), which is subsequently accelerated by the incident driving field (b). As the driving field changes sign, the electron is accelerated back towards the parent ion and recombination takes place. The kinetic and potential energy gained by the electron is released as an XUV photon during this step (c). The Keldysh parameter, defined as the ratio of the tunnelling and laser periods and expressed by equation 5.1, determines whether the electron is ionized by multiphoton

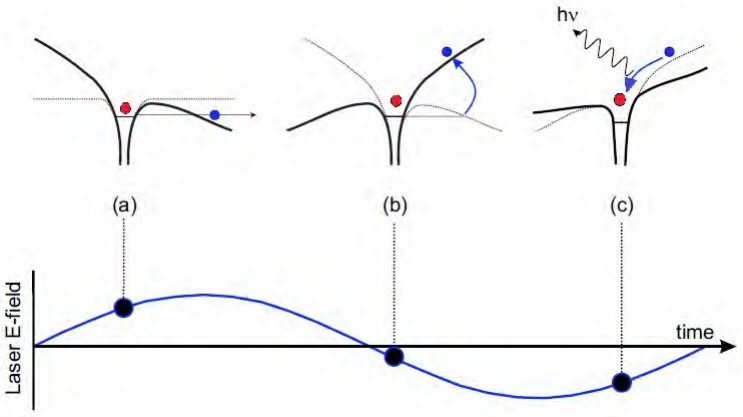

FIGURE 5.1: The three step model for HHG. a) Tunnel ionization of the electron and subsequent acceleration by the electric field. b) The field changes sign, reversing the acceleration of the electron and c) the electron recombines with the parent ion, releasing an XUV photon.

absorption ($\gamma >> 1$) or quantum tunnelling ($\gamma << 1$).

$$\gamma = \sqrt{\frac{I_p}{2U_p}} \tag{5.1}$$

I_p is the ionization potential of the parent atom or ion. U_p is the ponderomotive potential, given by the average kinetic energy that a charged particle has when oscillating in a laser field:

$$U_p = \frac{e^2 E_0^2}{4 m_e \omega_0^2} \tag{5.2}$$

Analysing the electron motion after ionization is useful in determining its recombination energy as a function of ionization time. Assuming a cosinusoidal field and equating the mechanical and Coulomb forces acting on the electron yields the acceleration:

$$\frac{d^2x}{dt^2} = \frac{-eE_0 \cos(\omega_0 t)}{m_e} \tag{5.3}$$

in which e is the unit charge, E_0 is the amplitude of the driving field of angular frequency ω_0, and m_e is the electron mass. Subsequent integration over time gives the electron velocity and position as a function of ionization time, t_0:

$$\frac{dx}{dt} = \frac{eE_0}{m_e \omega_0} [\sin(\omega_0 t) - \sin(\omega_0 t_0)] \tag{5.4}$$

$$x = \frac{eE_0}{m_e \omega_0^2} [\cos(\omega_0 t_0) - \cos(\omega_0 t) - \omega_0 (t - t_0) \sin(\omega_0 t_0)] \tag{5.5}$$

Here, the position of the parent ion is assumed to remain constant (fixed at $x = 0$) and the electron is assumed to have zero kinetic energy immediately after ionization. The left plot of figure 5.2 illustrates the trajectories taken by the classical electron for a range

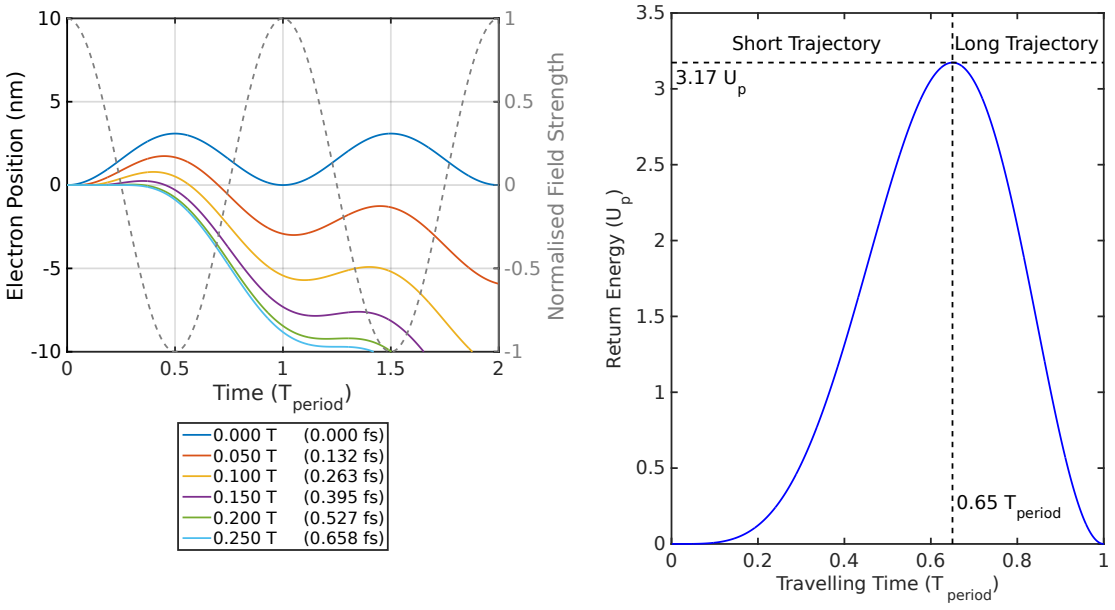

FIGURE 5.2: Left: Electron trajectories for six ionization times, t_0, between $0 \leq t_0 \leq T/4$ of a cosinusoidal driving field (790 nm wavelength). Right: Electron return energy (units of ponderomotive potential) as a function of time spent in the continuum.

of ionization times over the interval $0 \leq t_0 \leq T/4$, where T indicates the period of the $\vec{E}$-field. As is indicated by both equation 5.4 and the trajectories in figure 5.2, the return velocity of the electron is dependent on ionization time, and has zero value for returning electrons which were ionized at $t_0 = 0$, and for the limiting case in which $t_0 = T/4$. The latter case describes the condition for which the electron is accelerated away from the ion permanently, and the recombination step fails to take place. This continues to occur between $T/4 \leq t_0 \leq T/2$, after which the process of ionization and recombination may occur for the next quarter period. Recombination (and subsequently, XUV emission) therefore occurs for all $nT \leq t_0 < nT/4$ and does not occur for all $nT/4 \leq t_0 < nT/2$ for cosinusoidal driving fields, where $n \in \mathbb{Z}$.[1] With emission occurring antisymmetrically every half period, the XUV spectrum is composed of the odd harmonics of the multi-cycle driving pulse.

The right hand plot of figure 5.2 shows the calculated return energy, given by the kinetic energy of the electrons at recombination with the parent ion. Other than at the global maximum at 65% of the driving field period the return energy is not unique with recombination time, but has two solutions. These correspond to the longer and shorter trajectories shown in figure 5.2, which have equal durations at 65% of the driving field period. The shorter trajectories correspond to later ionization times.

The classical cut-off law for the highest energy harmonic may be read directly from the maximum of the right hand plot of figure 5.2. The duration of the long and short

[1] An equivalent condition exists for sinusoidal driving fields, and is given by the addition of $T/2$ to the limits given for the cosinusoidal case.

trajectories is equal at the maximum return energy of 3.17 times the ponderomotive potential. By conservation of energy, the highest photon energy released in the recombination is given by:

$$\hbar\omega_{max} = I_p + 3.17U_p \tag{5.6}$$

Much of the numerical and experimental work presented in this thesis is based on the relevant application of equation 5.6.

5.2 The quantum mechanical model

In the quantum mechanical model of HHG the classical approximation of the driving optical field is maintained. Conversely, the electron is no longer treated as a free-space classical particle, and its motion is described by a temporal and positional probability density. This itself is under the influence of the optical field and a soft Coulomb potential (as defined in equation 5.9 below), which represents the stationary parent ion. The assumption that the optical intensity is low enough to negate the influence of the magnetic component of the optical field also removes the necessity for a relativistic description of the electron motion. Due to this, the electron wavefunction shares the electronic and inertial properties of the classical particle.

The description presented below has been simplified by a number of approximations. A linearly polarized optical field restricts the influence of the soft Coulomb potential to one spatial dimension, while the atom itself is modelled as a single electron bound in a potential. The evolution of the electron wavefunction, $|\psi(x,t)\rangle$, is then derived from the time-dependent Schrödinger equation (TDSE):

$$\hat{H}|\psi(x,t)\rangle = i\hbar\frac{\partial}{\partial t}|\psi(x,t)\rangle \tag{5.7}$$

in which the Hamiltonian is defined as follows:

$$\hat{H} = -\frac{\hbar^2}{2m_e}\frac{\partial^2}{\partial x^2} + V(x,t) \tag{5.8}$$

Here, $V(x,t)$ is a potential determined by the optical field and a soft Coulomb potential, which is used in order to avoid singularities in the calculations:

$$V(x,t) = \frac{-e^2}{4\pi\epsilon_0}\frac{1}{\sqrt{\alpha_0^2 + x^2}} + eE(t)x \tag{5.9}$$

where α_0 is the Bohr radius, $a_0 = 5.29\times10^{-11}$ m, multiplied by a scalar chosen so that the ionization potential matches the gas species in question ($\alpha_{0,\,\mathrm{Ar}} = 1.7a_0$, $\alpha_{0,\,\mathrm{Xe}} = 2.2a_0$ for ionization potentials of 15.76 eV and 12.13 eV, respectively).

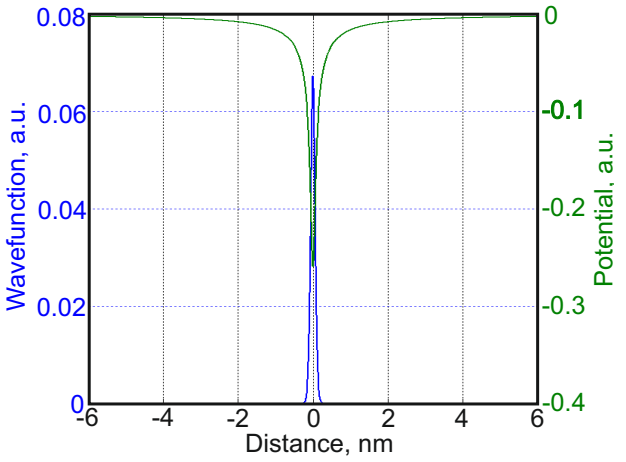

FIGURE 5.3: The initial ground state wavefunction of the electron in the soft Coulomb potential.

Figure 5.3 shows the initial electron wavefunction in the soft Coulomb potential for argon gas, calculated using equations 5.7–5.9 under the approximation that the optical field has zero amplitude. Once this wavefunction is known, Taylor's theorem is then used to approximate the temporal evolution of the electron wavefunction. Substituting for the temporal derivative in the Schrödinger equation yields:

$$|\psi(x,t_0+t)\rangle \approx |\psi(x,t_0)\rangle - \frac{i}{\hbar}(t-t_0)\hat{H}|\psi(x,t_0)\rangle \tag{5.10}$$

Using a time propagator of the form $\hat{T} = \exp\Big(-(i/\hbar)\hat{H}(t-t_0)\Big)$, which may be introduced by a comparison of its Taylor expansion with that of $|\psi(x,t)\rangle$, allows for equation 5.10 to be expressed as follows:

$$|\psi(x,t_0+t)\rangle = \left[\hat{I} - \frac{i\Delta t}{\hbar}\left(-\frac{\hbar^2}{2m_e}\frac{\partial^2}{\partial x^2} + V(x,t)\right)\right]|\psi(x,t_0)\rangle \tag{5.11}$$

where $\hat{I}$ is the identity operator, and $\Delta t = (t - t_0)$. Equation 5.11 expresses the temporal evolution of the electron wavefunction within potential $V(x,t)$.

In order to define an expression for the spatially dependent term of equation 5.7 the spatial evolution of $|\psi(x,t)\rangle$ is expressed as the mean average of the solutions to the forward and backward Euler methods (a finite difference technique known as the Crank-Nicolson method). The Taylor expansion of both $|\psi(x_0+x),t)\rangle$ and $|\psi(x_0-x),t)\rangle$ is followed by their addition, and rearrangement gives the second spatial derivative:

$$\frac{\partial^2\psi}{\partial x^2} = \frac{\psi_n^{i+1} - 2\psi_n^i + \psi_n^{i-1}}{(\Delta x)^2} \tag{5.12}$$

in which the nomenclature has been abbreviated such that $|\psi(x_i,t_n)\rangle = \psi_n^i$. Using equation 5.12 in the Schrödinger equation gives rise to the forward time central step

solution:

$$\psi_{n+1}^{i} = \psi_{n}^{i}\left[\hat{I} - \frac{i\Delta t}{\hbar}\left(-\frac{\hbar^2}{2m_e}\frac{\psi_{n}^{i+1} - 2\psi_{n}^{i} + \psi_{n}^{i-1}}{(\Delta x)^2} + V(x,t)\right)\right] \tag{5.13}$$

Equivalently, there exists an expression for ψ_{n-1}^{i} which is derived by backwards propagation and is referred to as the backward time central step solution. The Crank-Nicolson method is then used, giving:

$$\psi_{n+1}^{i} = \left(\hat{I} + \frac{i\Delta t}{2\hbar}\hat{H}\right)^{-1}\left(\hat{I} - \frac{i\Delta t}{2\hbar}\hat{H}\right)\psi_{n}^{i} \tag{5.14}$$

A visual representation of $|\psi|^2$ for the electron before, during, and after the interaction of a 5 fs driving pulse with a single atom is given in figure 5.4, and was produced using the derivation above. The maximum displacement of the electron from the origin is much larger than the radius of the parent ion, which justifies the free-electron assumption made in the semi-classical model. Analogously, the classical electron trajectories depicted in figure 5.2 are also reproduced as ripples of high probability density, propagating away from or interacting with the ionic core, as was seen in the classical model.

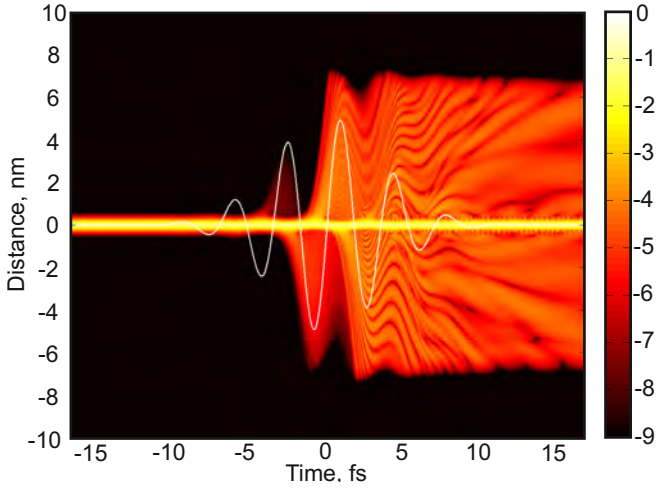

FIGURE 5.4: A 5 fs driving pulse of 1045 nm wavelength and $\sim 1.8\times10^{14}$ Wcm^{-2} intensity (white line) is incident on a single Ar atom. The colourmap represents $\log_{10}(\langle\psi|\psi\rangle)$ for the electron involved in the interaction.

Differences between the classical and quantum mechanical models arise when considering the recombination process. Previously it was suggested that the purely classical electron falls back to the ground state after returning to its parent ion. In the quantum mechanical description, the portion of the wavefunction which tunnels through the field-distorted soft Coulomb potential suffers a temporal phase shift (and therefore a translation in frequency) relating to the time propagator in equation 5.11 during acceleration in the continuum. On returning to the parent ion, the induced frequency shift results in interference between the portion of the wavefunction which was propagated

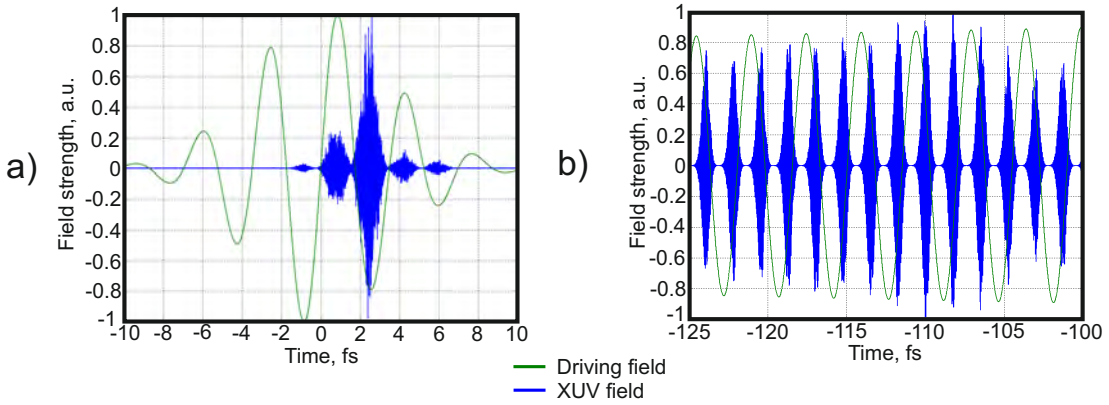

FIGURE 5.5: Applying a high-pass filter to the acceleration versus dipole moment allows for the attosecond XUV pulse train to be seen clearly: a) XUV bursts from the 5 fs pulse shown in figure 5.4, and b) XUV bursts generated by a 330 fs pulse with a central wavelength of 1045 nm and intensity of $\sim 1.8 \times 10^{14}$ Wcm^{-2}. Argon was used as the target gas for both simulations.

and that which remained bound within the atomic potential. The result is an induced dipole oscillation with dynamics determined by the beating caused by the wavefunction interference. Driven by this highly nonlinear interaction with the incident optical field the oscillating dipole radiates, generating the XUV field, which may be calculated from the second derivative of the positional expectation value.

Figure 5.5 demonstrates the dipole oscillation in the time domain after a high-pass frequency filter has been applied, allowing for the attosecond structure of the XUV pulse train to be seen clearly. Figure 5.5a shows the XUV pulse train for the single atom interaction with the 5 fs pulse shown in figure 5.4. The pulse parameters used for this simulation are similar to those most frequently used for high-harmonic generation due to the high intensities which they provide. Figure 5.5b shows the same thing, but for a 330 fs driving pulse with a central wavelength of 1045 nm and an intensity of approximately 1.8×10^{14} Wcm^{-2}. These parameters were chosen as they are similar to those produced by Yb-fibre CPA systems. As is expected, shorter driving pulses produce fewer attosecond XUV bursts (isolated, in some cases [104]) than the longer pulses. The latter may be used to generate XUV pulse trains. Figure 5.5b has been cropped to show the leading edge of the long driving pulse, where the XUV pulses with the highest amplitude are produced, due to the ionization process saturating the ion population of the target gas over the pulse duration. This has important consequences for the generation efficiency, and will be discussed further in section 5.4.

By taking the Fourier transform of the dipole acceleration the spectrum radiated by the oscillating dipole can be predicted. This is shown in figures 5.6a and b for the 5 fs and 330 fs driving pulses, respectively. Shorter driving pulses generate spectra with an under-developed harmonic structure due to the low number of XUV bursts produced each half cycle. The odd harmonics are only visible in figure 5.6a for the perturbative

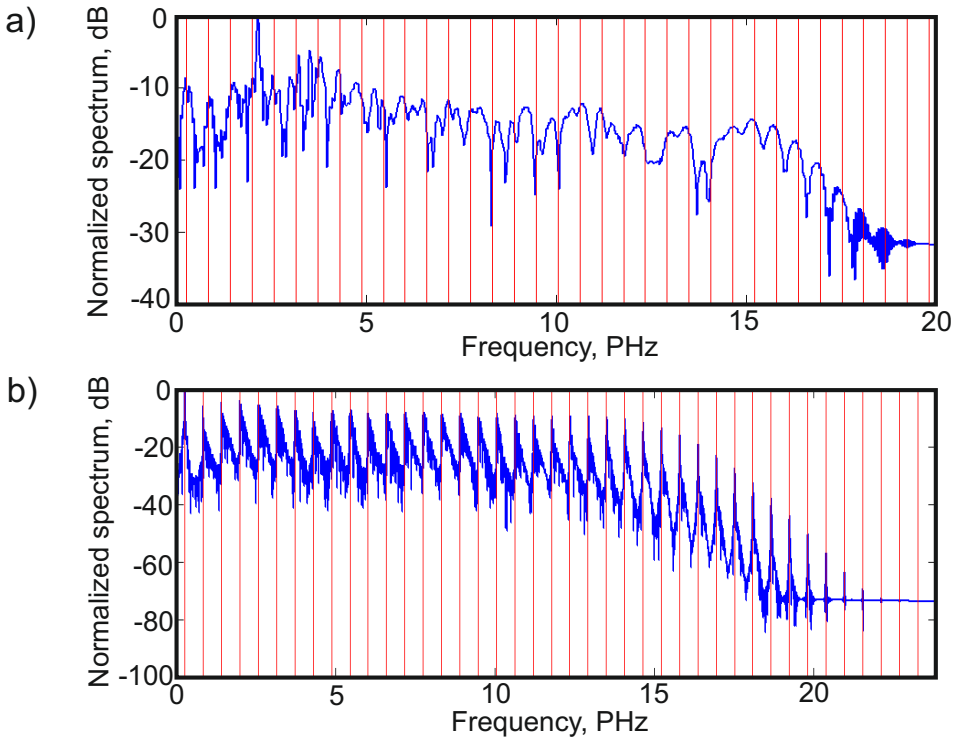

FIGURE 5.6: The emission spectrum of the oscillating dipole for a) the 5 fs pulse shown in figure 5.4, and b) the 330 fs pulse shown in figure 5.5. In both plots, the red lines mark the frequencies of the odd harmonics of the driving laser field. Argon was used as the target gas for both simulations.

region (harmonic orders 1 to 5), and after cut-off at approximately 17 PHz (17.6 nm). The carrier-envelope phase of shorter (sub-10 fs) driving pulses strongly determines the number of XUV bursts produced, and therefore the degree of spectral modulation. The carrier-envelope phase for the simulation shown in figure 5.6a is $\pi/2$, giving the maximum spectral modulation for this example. This effect is not seen for longer driving pulses (figure 5.6b). The large number of generation sites in the longer pulses and the resulting train of attosecond XUV bursts creates a fully developed spectral modulation, with well defined narrow line odd harmonics of the driving laser field.

In light of the differences between the properties of the XUV produced when using short or long driving pulses, it becomes apparent that the resultant single-shot flux (intrinsically higher for shorter pulses of a given energy) is not the only parameter which needs to be considered when designing a usable HHG source. These differences, as well as the usable XUV photon flux, determine the suitability of a source for a given application. For example, near single-cycle driving pulses may be used to generate isolated attosecond pulses for time resolving molecular electron dynamics [105]. However, often narrow-band XUV radiation is required (e.g. for lithography, photoelectron spectroscopy, etc.), and such a source would be less suited to this experiment due to a reduction in the XUV

power spectral density for a given pulse energy. Here, the fully developed spectral modulations exhibited by longer driving pulses maximize the power spectral density of each harmonic order, leading to an increased efficiency when monochromating the XUV.

5.3 Generation methods

The simplest experimental setup for HHG uses a tapered glass or metal nozzle backed with approximately 1 bar of gas which is fed from a wider inlet through to a 0.1-1 mm aperture to form a supersonic jet, and is shown in the top left of figure 5.7. Maximum flux for this geometry is found when the driving field is focussed into the Mach disk [106], situated underneath the nozzle. Improved generation efficiency is usually found for the gas cell geometry due to the extended interaction length and higher achievable gas density in comparison to the jet [107]. In this thesis, gas cells are constructed from lengths of copper tubing, and gas is fed through the cell from one end and is prevented from leaking through the other by blocking the tubing (right hand side of figure 5.7). Entrance and exit holes for the driving field are drilled through either side of the copper tubing. As discussed in section 5.4 it is often necessary to translate the focus through the target gas to find the position of best phasematching. By using a gas cell to increase the interaction length a larger parameter space may be scanned when finding the best focal position. Additionally, the restriction on gas flow from the generation region to the surrounding vacuum may be higher for a gas cell than a jet, and is achieved by using small entrance and exit holes for the gas cell. The higher vacuum outside of the generation region leads to a reduced background absorption of the XUV as it propagates from the generation region to the detection optics.

The capillary geometry shown at the bottom of figure 5.7 may be used for enhanced conversion efficiency. Capillaries are usually constructed from silica, with gas inlet holes positioned close to the ends. In the initial stages of propagation through the capillary, the fundamental driving field undergoes temporal and spatial compression through SPM, dispersion, and mode beating. The longitudinal positions at which temporal and spatial compression is maximized can be made to coincide by tuning gas pressure, capillary length and bore to increase the intensity at the capillary output by approximately two orders of magnitude [108]. The XUV is then generated at this point, and the best flux is found when the capillary is terminated here to minimize reabsorption. This geometry comes at the expense of increased design complexity, as the capillary setup must in general be developed using a numerical approach to find the optimum parameters for a given input pulse. It has recently been shown that capillary design can provide a 50-fold increase in flux by exploiting temporal pulse self-compression and mode beating to achieve near single-cycle driving fields with intensities of 10^{14} W/cm^2 from a 40 fs,

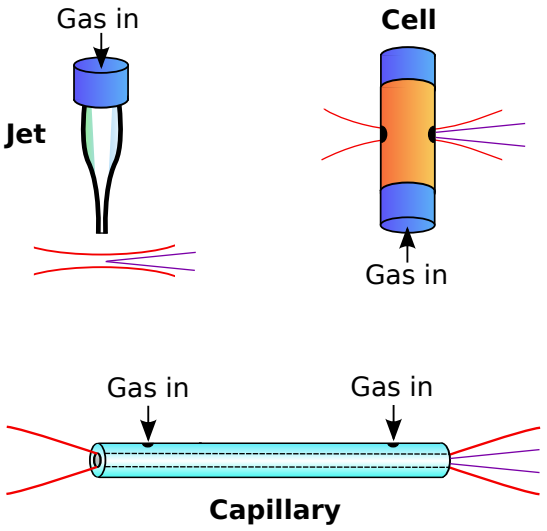

FIGURE 5.7: Schematic of the jet (top left), cell (top right), and capillary (bottom) geometries. The red and purple lines denote the infrared driving field and the generated XUV, respectively.

1 mJ driving pulse at the capillary input [108, 109, 110, 111].

Both the gas cell and capillary geometries are used in this thesis. A capillary HHG source was used while developing and testing the single-exposure XUV characterization method outlined in chapter 6. A gas cell was used for XUV generation with the fibre CPA system, and details of this experiment are given in chapter 7.

5.4 Phasematching and efficiency

In order to achieve a high conversion efficiency from the driving field to the XUV macroscopic effects must be considered alongside the single atom description, and are incorporated into the theory by the difference between the wave vectors of harmonic q and q times the fundamental driving field:

$$\Delta\vec{k} = \vec{k}_q - q\vec{k}_f \tag{5.15}$$

Under the condition that equation 5.15 has zero value the frequency conversion process is said to be phase-matched, and energy is efficiently and continuously transferred to harmonic q. Contributions to the phase mismatch between the fundamental and harmonic q are determined by the dispersion from the the free electrons released during the HHG process (Δk_0), neutral gas atoms (Δk_d), the atomic phase (Δk_a), which corresponds to the phase acquired by the electron wavefunction in the continuum and that due to the time difference between ionization and recombination [112], and geometrical effects such as the Gouy shift and those imposed by the generation geometry (Δk_G). These terms

must be balanced for perfect phasematching over an infinite distance [113]. For the case that this condition is not met a coherence length is defined as $L_c = \pi/\Delta k$ to determine the length over which the phase mismatch evolves by π radians.

Due to the extended pulse duration used to drive the HHG process with the fibre CPA system presented in this thesis, a large amount of plasma is generated at the early stages of the pulse. As shown by figure 5.8, the ion fraction can be as high as 100% at the peak intensity of the pulse for typical fibre CPA parameters [114] (See Appendix B for the MATLAB script used for this calculation). This induces a refractive index change over its duration, and alters the phasematching condition as well as the spatial and temporal characteristics of the driving field.

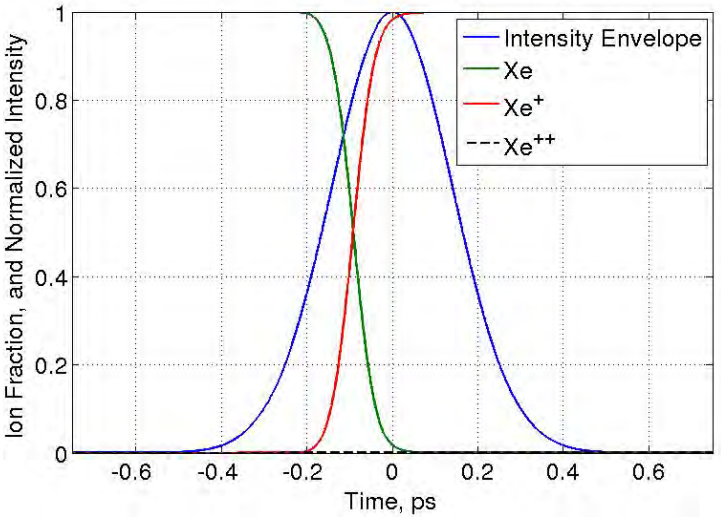

FIGURE 5.8: Calculation of the on-axis population fraction of neutral Xe atoms (green), Xe^+ ions (red), and Xe^{++} ions (black dashed) over the duration of a 100 μJ, 330 fs pulse (blue line) focused to a 7 μm spot to reach an intensity of 1.8×10^{14} Wcm^{-2}.

The refractive index experienced by the fundamental due to the free electrons is calculated as follows:

$$n_f = \sqrt{1 - \frac{\omega_p^2}{\omega_0^2}} \tag{5.16}$$

in which ω_p is the plasma frequency:

$$\omega_p = \sqrt{\frac{e^2 N_e}{m_e \epsilon_0}} \tag{5.17}$$

Here, N_e is the free electron density, and given by the product of pressure (in atmospheres), ionization fraction, and the number density of atoms at 1 atm. Using equation 5.15, it is found that the phase mismatch and resulting coherence length due to the free electrons are given as:

$$\Delta k_0 = \frac{\pi q \omega_p^2}{\lambda_0 \omega_0^2} \tag{5.18}$$

$$L_{cf} = \frac{2\pi c\omega_0}{q\omega_p^2} \tag{5.19}$$

It may be assumed that the ionization has no effect on the refractive index of the gas species [115], giving the ion population the same refractive index as the neutral atoms. The refractive index of the partially ionized gas can therefore be written as:

$$n = 1 + P\delta(\lambda) \tag{5.20}$$

where $\delta = Re(n) - 1$ and P is the pressure in atm. Using this, the wave vector may be expressed as the sum of the vacuum wave vector and that due to the refractive index of the partially ionized gas. Using equation 5.15, the phase mismatch due to the neutral and ionized gases is as follows:

$$\Delta k_d = \frac{q2\pi P}{\lambda_0}(\delta(\lambda_q) - \delta(\lambda_0)) \tag{5.21}$$

The coherence length for the partially ionized gas can then by defined as:

$$L_{cd} = \frac{\lambda_0}{2qP}\frac{1}{(\delta(\lambda_q) - \delta(\lambda_0))} \tag{5.22}$$

The free electron coherence length (equation 5.19) is proportional to the fundamental frequency, and inversely proportional to the harmonic order and the square of the plasma frequency, and therefore decreases rapidly for a higher ionization fraction. Conversely, the dispersion of the partially ionized gas is proportional to wavelength, but maintains the inverse proportionality to harmonic order and pressure. The coherence lengths for the free electrons and the partially ionized gas therefore decrease with increasing harmonic order, making it increasingly difficult to phase-match higher harmonics.

In addition to the partially ionized gas and free electron phase mismatches, the length of the trajectory followed by the ionized electron (as shown in figure 5.2) also plays a significant role in the conversion efficiency from the fundamental to harmonic q. This is referred to as the atomic phase in the literature, and is given by [112]:

$$\phi_a = \frac{S(t_0, t_1)}{\hbar} + q\omega t_1 \tag{5.23}$$

The phase mismatch contribution from the atomic phase is therefore given by:

$$\Delta\vec{k}_q = q\vec{k_1} + \vec{\nabla}\phi_a(r, z) \tag{5.24}$$

where $\vec{k}_1$ is the wave vector for the fundamental, and:

$$S(t_0, t_1) = \int_{t_0}^{t_1}\left(\frac{m_e v^2(t)}{2} + I_p\right)dt \tag{5.25}$$

Here, $t_{0,1}$ are the ionization and recombination times, respectively, and S is the quasi-classical action, given by the integral of the total electron energy over time spent in the continuum. As discussed in section 5.2, the fraction of the electron wavefunction which is ionized undergoes a frequency shift which is proportional to the kinetic energy gained as it is propagated outside of the atomic potential. A shift in phase accumulates as a result of this frequency shift, and therefore the long and short trajectories experience different atomic phases with an intensity variation which is greatly lessened for the short trajectories. The spatial intensity variation has a profound effect on the spatial profile of the harmonic field, resulting in an annular structure for the long trajectory harmonics.

When considering gas jet and cell geometries, the effects of focusing a free-space mode must be taken into account. The transverse and longitudinal spatial phases of the focused Gaussian beam therefore have an effect on the phase mismatch, and are described by [112]:

$$\phi(r,z) = \arg\left[\frac{1}{2(z_0+iz)}\exp\left(-\frac{k_0 r^2}{2(z_0+iz)}\right)\right] \tag{5.26}$$

where r is the radial distance, z is the longitudinal distance, and z_0 is the Rayleigh range. Considering the on-axis phase shift (known as the Gouy phase, $\phi_G = \arctan(z/z_0)$ [116]), it is possible to write the on-axis wave vector imparted on the driving field by the focal geometry:

$$k_G = \frac{d\phi_G}{dz} = \frac{z_0}{z^2+z_0^2} \tag{5.27}$$

Using equation 5.15, the phase mismatch due to the Gouy shift and its associated coherence length may be written as:

$$\Delta k_G = -\frac{qz_0}{z^2+z_0^2} \tag{5.28}$$

$$L_{cG} = \frac{\pi(z^2+z_0^2)}{qz_0} \tag{5.29}$$

where the wave vector for harmonic q has been neglected under the assumption that $1/(qz_0) \approx 0$.

As the Gouy coherence length is approximately proportional to the Rayleigh range, it becomes dominant for systems requiring small spot sizes to reach the required intensities of $\sim 10^{14}$ Wcm^{-2} for HHG to take place. It has been shown that the mismatch between the Gouy and atomic phases is dependent on the relative position of the generation medium with respect to the focus [112]. This z-dependence of the total phase mismatch results in a variation in phasematching conditions throughout the focal volume, and there exists a longitudinal position where phasematching of the q^{th} harmonic may be achieved. When using the cell or jet geometry, translating the focus through the gas

explores a parameter space which is dependent on the ionization fraction (and therefore intensity), gas pressure, as well as the Gouy and atomic phases to find the position of the focus relative to the generation medium which gives the best phasematching. This is exploited in the gas cell HHG geometry described in chapter 7.

The wavelength of the driving field further limits the HHG efficiency. The λ^2 dependence of the ponderomotive potential (see equation 5.2) has placed wavelength scaling of the fundamental at the forefront of a number of recent HHG experiments in which shorter wavelength XUV was the desired outcome [117]. Despite the production of shorter wavelength XUV radiation, this is not a parameter which will be exploited within this project due to the inherent difficulty of phasematching high order harmonics, which is a direct result of the inverse proportionality of the coherence lengths with order number, q.

It has also been noted that the production efficiency of the harmonics scales with approximately λ_0^{-6} [118]. The origin of this is purely quantum mechanical, and is based in the continuous spatial dispersion of the electron wavefunction during free-space propagation. Longer driving wavelengths lead to a larger difference between ionization and recombination times, therefore resulting in the wavefunction being dispersed more. The overlap between the electron wavefunction and the parent ion is therefore reduced, and this greatly reduces the strength of the beating which occurs between the ionized portion of the wavefunction and that which remained within the Coulomb potential. The XUV yield is therefore diminished, as less of the energy gained by the electron during propagation is transferred to the dipole oscillation.

5.5 Summary

This chapter introduced the classical and quantum mechanical models of the single-atom HHG process. The models were shown to quantitatively predict the characteristics of the generated harmonics, such as the frequency cut-off, and qualitatively suggest the extent to which the generated spectra are modulated, and the number of XUV bursts per shot. It was shown that fundamental differences in the resulting XUV pulse trains and spectra between short and long driving pulses exist, and appropriate applications for both cases were briefly discussed.

Different HHG geometries were then described before phasematching was considered in order to describe limitations on the harmonic generation efficiency in the fibre CPA experiments. It was shown that the limitations arise due to the phase mismatch between the fundamental and each generated harmonic as a result of dispersion from the neutral and ionized gas, the contribution from the electron trajectories, and the phase mismatch created by the focal geometry. The inverse proportionality of coherence length on the harmonic order was described. A method for reducing the phase mismatch involving a

balance of gas pressure, driving pulse intensity, focal position, and the atomic phase was also introduced, before the effects of wavelength scaling were discussed.

Chapter 6

Single exposure characterization of high-harmonic XUV radiation

6.1 Introduction

It is important for novel XUV sources to be characterized fully, and a number of methods have been outlined recently for determining the XUV spectrum, accurately retrieving the transverse phase profile and, in some cases, the spatial coherence for each harmonic [119, 120, 121, 122]. These methods each rely on spatially sampling the beam by scanning narrow slits across it, before grazing incidence spectrometry spatially separates the harmonics at a detector. This leads to a relatively complex alignment procedure, inefficient use of the generated XUV flux, a requirement for moving parts, and propagation distances of order 1 m which will result in a low XUV intensity at the detector due to the tight focusing required for HHG with the fibre laser system. The characterization process is also restricted to one spatial dimension and requires multiple exposures. As such, although these methods can be highly accurate and are appropriate for low divergence sources, they do not present a practical route for characterising the XUV as generated by the fibre laser system developed in this work.

A single exposure spectrometry method (developed before this work was started by Dr. Matthew Praeger, University of Southampton – see refs. [123, 124]) was adopted as an alternative to grazing incidence spectrometry because it has minimal spatial sampling and therefore makes efficient use of the XUV flux by detecting most of the beam, can spatially resolve the spectrum in two dimensions, and has very flexible design parameters allowing for propagation distances of order 0.1 m to be used. In this thesis work, the method was extended to include radius of curvature retrieval, thus allowing for a more complete characterization of the fibre CPA system as a high-harmonic source through an

appropriate method requiring just one exposure of the beam. When applied generally, the method may be used to characterize low-flux sources when longer integration times are used, or to determine the single-shot beam characteristics with high-flux sources. The method is demonstrated in a proof-of-principle experiment in this chapter using a capillary high-harmonic source, and is shown to allow for the two-dimensional XUV intensity profile at the capillary exit to be reconstructed from an exposure of just 50 laser shots.

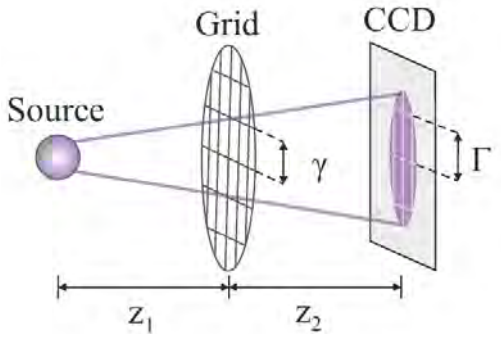

FIGURE 6.1: Schematic of the alignment free XUV characterization setup.

The general experimental setup is shown in figure 6.1. Light emitted from a source propagates a distance z_1 before being diffracted by a grid with square apertures of period γ. The diffracted light then propagates a distance z_2 before it is incident on a spatially sensitive detector, such as a CCD. The spatially resolved spectrometry information is retrieved from the projected near-field diffraction pattern of each individual grid square, and the radius of curvature information is calculated using distance z_2 and the period of the grid projection at the CCD, Γ.

This chapter is structured as follows: Section 6.2 introduces the spatially resolved spectrometry technique, which was developed in the Ultrafast X-ray Group at the University of Southampton prior to this thesis work. Following that, the algorithm for retrieving the radius of curvature is described in section 6.3, before experimental guidelines for implementing the spectrometry and radius of curvature methods are given in subsection 6.4. The full characterization technique is then applied to experimental data taken using a capillary high-harmonic source in section 6.5. Limitations and future work are discussed in section 6.6, before the chapter is concluded in section 6.7. All simulated diffraction patterns presented in this chapter were calculated using the angular spectrum method (ASM) [125]. A proof for this technique and a MATLAB function for calculating near-field diffraction patterns using this technique are given in Appendix E.

6.2 Prior art: Spatially resolved spectrometry using single-image diffraction

This section describes a technique for analysing Fresnel diffraction patterns from square apertures in order to infer spectral information about the source, and was reported previously in refs. [123, 124]. By analysing the diffraction pattern created by an array of square apertures and considering each aperture independently, the retrieved spectral information may be spatially resolved across the beam.

The spectrometry technique uses the general setup shown in figure 6.1, and figure 6.2 shows a simulation of near-field diffraction of monochromatic XUV radiation as would be seen using a setup similar to this, with the exception that the grid has been replaced by a single square aperture for the purposes of this introduction. Distances z_1 and z_2 were equal to 0.5 m for this simulation, and the aperture size was set to 340 μm to match the experimental configuration described later in section 6.5. In the simulation, the resulting intensity distributions for 27 and 38 nm wavelength light are compared. As can be seen in the figure, although the square shape of the aperture is in part maintained, there is a significant difference in the intensity distribution between the two wavelengths. This difference may be used to infer the spectral content of the XUV beam in the plane of the grid.

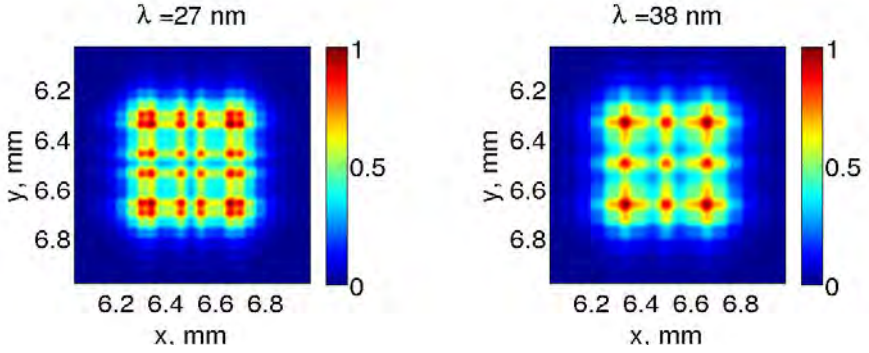

FIGURE 6.2: ASM simulation showing diffraction changes associated with different XUV wavelengths.

The algorithm which predicts the XUV spectrum uses wavelength and intensity as the input variables for simulating diffraction from a square aperture with the same dimensions as that used in the experimental arrangement. The diffraction is simulated for each wavelength in a user defined range, and a least squares fitting routine is then used to determine the correct intensity for each wavelength component so that the incoherent sum of the simulated diffraction patterns produces a good match with the experimental data. The algorithm outputs the spectral intensities which minimize the difference between simulated and experimental diffraction patterns, thus providing an estimate of the XUV spectrum.

Prior to simulating the diffraction, the four-fold symmetry of the square aperture is exploited, and a uniform intensity distribution at the plane of the square aperture is forced on the experimental data. This is done by taking the average of four copies of the measured diffraction patterns, each respectively oriented at multiples of 90°. The result is a symmetrized diffraction pattern resembling that which would be produced by uniform illumination of the square aperture. This process serves to increase the signal-to-noise ratio of the experimental data and greatly simplifies the procedure for calculating the spectral intensities.

The intensities for each wavelength are inferred by finding positive solutions to the following equation:

$$P_{\mathrm{exp}}(x,y) = \sum_{h=1}^{\infty} P_{\mathrm{sim}}(x,y,h)I(h) \tag{6.1}$$

Here, P_{exp} is the symmetrized experimentally measured diffraction pattern for the square aperture, and P_{sim} is the simulated diffraction pattern for harmonic h. Parameters x and y are the spatial coordinates in the plane of the CCD. In this manner, the problem is reduced to a system of linear equations which are resolved by finding the set of $I(h)$ which minimizes the quantity $\mathrm{norm}(P_{\mathrm{sim}}(x,y,h)I(h) - P_{\mathrm{exp}}(x,y))$ by using a least squares routine. Typically, the user will enter 25 odd harmonics into the algorithm, with values between 13 and 59 for a driving field produced by either a Ti:Sapphire or Yb-fibre laser. The resulting diffraction pattern for one aperture typically occupies 50–150 pixels, resulting in a minimum of 2500 data points (or 2500 unknowns) for the system defined by equation 6.1. The problem is therefore overdetermined and no unique solution exists, so the spectrum output by the algorithm is a best fit estimate of the actual XUV spectrum.

If an array or grid of square apertures is used as the diffractive element as opposed to a single square aperture, this process can be repeated for each square in the array, thus providing the spatial distribution of the harmonic spectrum. The process for estimating the spatial distribution of the XUV spectrum may therefore be summarized as follows:

1. Crop the square of interest from the experimental grid diffraction data.
2. Symmetrize the cropped experimental data.
3. Simulate the diffraction for each wavelength in a user-defined array.
4. Use a non-negative least squares fitting routine to calculate the best fit spectral intensity for the square of interest.
5. Move to the next square, and repeat.

The following assumptions have been made:

1. The spectrum is assumed to consist of odd harmonics of the driving field centre wavelength, and the linewidth of each harmonic is ignored.

2. The beat period between adjacent spectral peaks is assumed to be ∼1–2 fs. As such, features in the diffraction pattern resulting from interference between different harmonics is averaged out over the integration time of the CCD.

3. The intensity of each harmonic is assumed to be uniform over each aperture.

4. Each diffraction pattern is assumed to be isolated, i.e., diffracted light from one square in the grid does not interfere with the light diffracted from adjacent squares.

Assumption 1 typically has the effect of increasing the contrast between diffraction minima and maxima, which would otherwise be reduced if the harmonic linewidth was taken into account. Although this assumption is not necessary for the method to work, it was found to improve the stability of the least squares routine when analysing each data set shown in this thesis. Assumption 2 is justified because the CCD measures the time-averaged intensity of the incident XUV field. It is therefore possible to reproduce the experimental diffraction pattern by considering the diffraction of each harmonic component independently, and then summing their intensities rather than their complex fields. Although assumption 3 does not hold for a typical HHG experiment, the aim is to produce a single set of spectral coefficients for each aperture, rather than to spectrally resolve the detailed intensity distribution within each aperture. Symmetrizing the experimental data validates this assumption. Assumption 4 may be justified by selecting appropriate experimental parameters for the grid, and distances z_1 and z_2, which will be discussed in section 6.4.

6.3 Radius of curvature estimation from single-image diffraction

Unlike the spatially resolved spectrometry technique introduced in section 6.2, the algorithm developed in this work for estimating the radius of curvature of an XUV beam uses the near-field diffraction pattern of the grid as a whole, rather than separately considering the diffraction pattern produced by each aperture in the grid. The algorithm is based on determining how the projected aperture size, Γ, scales as a function of radius of curvature. This principle is demonstrated in figure 6.3, which shows a zoomed area of a simulated near-field diffraction pattern produced by equal amplitude harmonics (numbers 19–29 for a 790 nm fundamental wavelength) after passing through a grid with 340 μm square apertures separated by opaque 40 μm thick bars (again, chosen to match

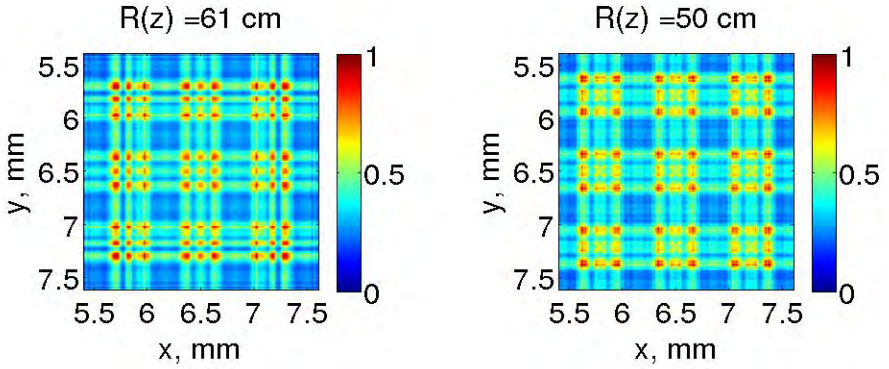

FIGURE 6.3: ASM simulation showing how the projected grid period changes with a change in radius of curvature.

the experimental arrangement in section 6.5). Distances z_1 and z_2 were set to 0.5 m.

The figure shows that for XUV fields incident on the grid, the radius of curvature scales the projected aperture size, Γ. A smaller positive radius of curvature, shown on the right of figure 6.3 and corresponding to a higher beam divergence, magnifies the projected aperture size at the plane of the screen/CCD in comparison to beams with larger positive radii of curvature (left of figure 6.3). If the sign of the radius of curvature is reversed, the opposite effect takes place, and Γ is reduced for the XUV beam with a smaller radius of curvature.

This characteristic of the near-field diffraction patterns produced by arrangements such as that shown in figure 6.1 was exploited to estimate the radius of curvature of an XUV beam. This was done by iteratively comparing the projected grid period from input diffraction data produced by the beam under test with that measured from diffraction data produced by simulated fields with different radii of curvature to produce a best-fit estimate. The algorithm required the user to input the following parameters:

1. The grid diffraction data under test (which may be generated from experiment or simulations).
2. The starting field in the plane of the grid: $A(x, y, z_1, \lambda)$.
3. The aperture size and spacing for the grid used as the diffractive optical element.
4. The distances between the source, grid, and CCD (z_1 and z_2).
5. A set of estimated radius of curvature values to be used in the ASM simulation step.

First the projected grid period, Γ, was measured from the input diffraction pattern. The diffraction data was integrated along one axis, and cubic smoothing splines were

fitted to the resulting curve to isolate the diffraction minima corresponding to the bars of the grid from other intensity modulations in the diffraction data. The distance between the diffraction minima defined the projected grid period, Γ_{exp}, which was then calculated and stored. This process was repeated for the other axis to obtain Γ_{exp} in two spatial dimensions, which concluded the analysis step for the input data.

Secondly, simulated diffraction data was calculated for comparison with the experimental data. The angular spectrum method was used to calculate the diffraction patterns for each wavelength at the CCD using the input harmonic intensity profiles and the grid parameters as defined by the user. The starting field used in the diffraction simulation was defined in the plane of the grid at distance z_1 from the source as follows:

$$E(x, y, z_1, \lambda) = A_0(x, y, z_1, \lambda) e^{\frac{ik\left(x^2+y^2\right)}{2R(z)}} \tag{6.2}$$

where A_0 is the square root of the spatial intensity distribution for harmonic wavelength λ. This field was then multiplied by the transmission function of the grid, and propagated using ASM to give the field distribution in the plane of the CCD. The standard parabolic phase term for approximating a spherical wavefront at large distances from the source was used, and is well supported by prior investigations of XUV sources [119, 120]. As with the spatially resolved spectrometry method, the total diffraction pattern for a given radius of curvature was then retrieved by an incoherent sum over the ASM propagated intensity distributions of each harmonic wavelength, λ. Following this, the projected grid period for the simulated diffraction, Γ_{sim}, was measured in the same way as the experimental data, and a comparison between Γ_{exp} and Γ_{sim} was made using:

$$\Delta\Gamma = |\Gamma_{\text{exp}} - \Gamma_{\text{sim}}| \tag{6.3}$$

This process was repeated for all elements of the user-defined set of wavefront curvatures for both the x- and y-directions. The radii of curvature within this set which minimized the difference between the experimental and simulated data were selected by the algorithm and output as the best-fit curvature values.

The Γ measurement is demonstrated in figure 6.4, which shows the analysis of the simulated data for two radii of curvature during the iterative comparison process. Two example diffraction patterns and the corresponding integrals over the y-axis are shown. As can be seen, an increase in radius of curvature from 0.3 m to 0.37 m reduced the projected grid period, Γ_{sim}, which was calculated to be 731 μm and 660 μm for the smaller and larger curvature values, respectively. The process for measuring Γ is summarized in the second row of the figure, and is the same for the input data analysis stage and the iterative comparison stage. The integrals (black lines) are calculated from the diffraction patterns, before cubic smoothing splines are fitted (blue lines), which are

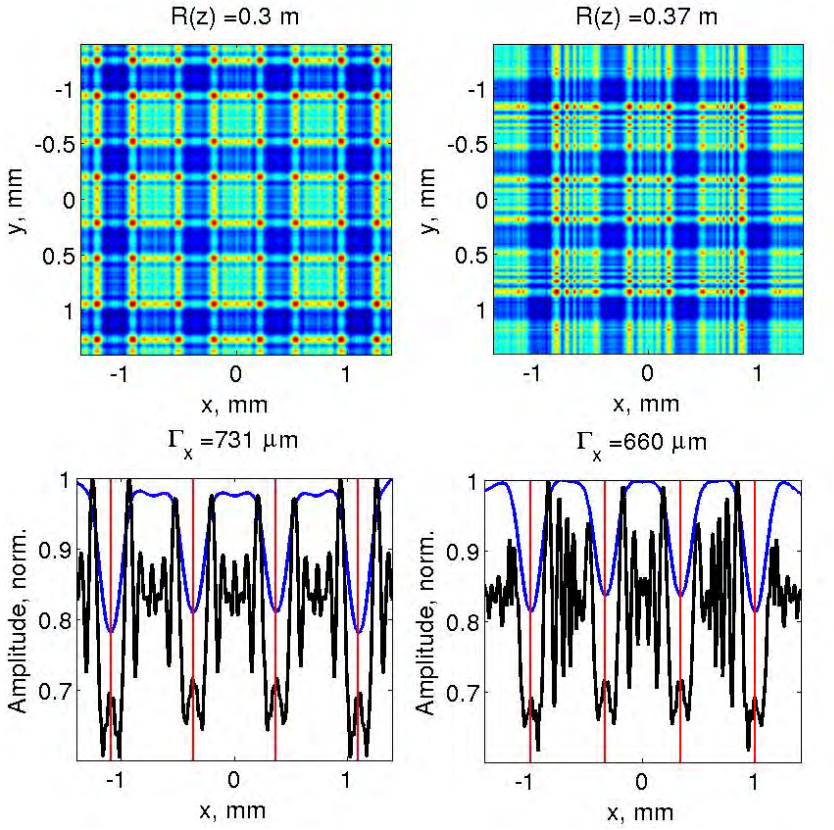

FIGURE 6.4: Left column: ASM simulation (top) and integral over the y-axis (bottom) for an input radius of curvature of 0.30 m. The black line is the integral data, the blue curve is a fit spline. The red lines indicate the minima corresponding to the grid bars. Right column: The same, but for $R(z) = 0.37$ m.

used to find the central point of the diffraction minima which correspond to the grid bars by smoothing over the fast intensity modulations in the diffraction pattern. The minima are marked by the red vertical lines, and Γ is given by their separation.

The algorithm used to estimate the radius of curvature from the user-defined input data listed above may be summarized as follows:

1. Load the input diffraction data, integrate along each axis, and fit cubic smoothing splines to the resulting functions. Γ_{exp} may be calculated from the separation of the spline minima.

2. Simulate the diffraction using the user-defined wavelengths and their intensity distributions, distances z_1 and z_2, and the first element of the set of estimated radii of curvature.

3. Calculate Γ_{sim} using the procedure outlined in item 1. Compare this value with Γ_{exp} using equation 6.3, and store $\Delta\Gamma$.

4. Repeat items 2 and 3 for all elements of the set of estimated radii of curvature values to define $\Delta\Gamma$ as a function of radius of curvature. Find the minimum of this function.

5. Output the radius of curvature which minimizes this function.

As part of a series of tests performed on the algorithm, numerical data was used as the input diffraction data so that field parameters could be 'dialled up' and tested efficiently. In one such test, diffraction data sets calculated from four fields with radii of curvature measuring 38.7 cm, 36.1 cm, 33.9 cm, and 35.1 cm were used as the input for four separate radius of curvature retrieval tests. For these tests, the user-defined set of estimated radii of curvature contained that used to produce each input diffraction data set to test that there was no uncertainty intrinsic to the retrieval process. $\Delta\Gamma$ as a function of radius of curvature for the iterative comparison step is shown in figure 6.5 for each of the four tests. As can be seen, the radius of curvature is retrieved with zero error for all four input data sets. For this test, a polychromatic field composed of odd harmonics from number 19 to 27 were used, with a fundamental wavelength of 790 nm. Each harmonic was assumed to have a uniform intensity distribution and equal amplitude. Distances z_1 and z_2 were set to 33.5 cm and 40 cm, respectively.

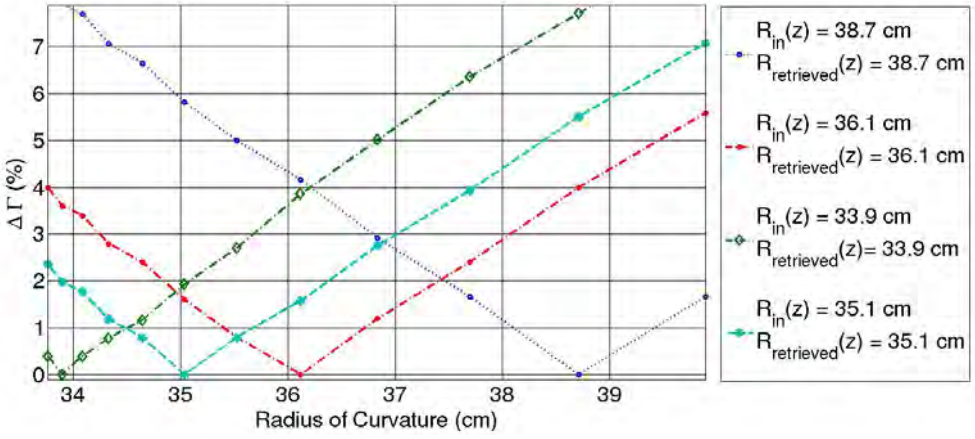

FIGURE 6.5: Testing the algorithm with simulated diffraction patterns created by an XUV field of five harmonics (19–27). The retrieved radius of curvature for each simulation as shown in the legend is seen to be an exact match to the input radius of curvature.

The algorithm was also tested using simulated input diffraction data under other conditions. For example, it was found that if the radius of curvature of the field used to generate the input diffraction data is not in the set of user-defined estimated radii of curvature values, $\Delta\Gamma$ does not fall to zero. A minimum does occur for $\Delta\Gamma$ about the input radius of curvature value, but a typical magnitude error of $\sim$0.3% resulted. By randomly generating radius of curvature values for the input diffraction data, it was possible to numerically generate an estimated average error of 0.6% for the retrieved radius of

curvature. Additionally, it was possible to approximate an error for the retrieved radius of curvature which occurs when the change in $\Delta\Gamma$ from one estimated radius of curvature to the next is smaller than the pixel size of the detector used. If this is the case, there will be no change in $\Delta\Gamma$ between pairs of consecutive radius of curvature estimates. The resulting uncertainty in the retrieved radius of curvature in this scenario is approximately 3.5%. This error may be mitigated (or at worst, minimized) by selecting appropriate experimental parameters, as discussed in section 6.4. The error in the best-fit radius of curvature value is therefore estimated to be of order 1%.

Although polychromatic radiation with uniform intensity distribution was used for these tests, it should be noted that harmonics with arbitrary intensity distributions can also be used. The intensity distributions for each harmonic as calculated by the spatio-spectral algorithm summarized in section 6.2 may therefore be used to define $A_0(x, y, z_1, \lambda)$ in equation 6.2, thus merging the two methods to provide a single-exposure characterization technique for XUV beams.

6.4 Experimental guidelines

In this section the near-field diffraction parameters required for the correct application of both the spectrometry and radius of curvature retrieval algorithms will be quantified, and experimental guidelines for implementing the methods will be outlined.

It is useful to refer to the Fresnel number when considering different diffraction regimes, and its definition is given as follows:

$$F = \frac{a^2}{\lambda z_2} \tag{6.4}$$

where a is the characteristic aperture width (for square apertures, this is given as the half-length of the aperture sides), λ is the wavelength, and z_2 is the distance between the aperture and the screen. If the incident beam is divergent, then this definition must be modified to account for the effect that divergence has on the diffraction. This is done as follows [126]:

$$F = \frac{(z_1 + z_2)a^2}{z_1 z_2 \lambda}. \tag{6.5}$$

For far field (Fraunhofer) diffraction, $F \ll 1$, and the diffraction pattern tends towards the Fourier transform of the field distribution in the plane of the grid. For the near field (Fresnel) regime, $F > 1$, with large F causing the diffraction pattern to tend towards the shadow pattern of the grid.

The radius of curvature estimation algorithm was found to work well for Fresnel numbers as high as 4, after which the change in Γ with wavefront curvature became

smaller than the pixel size of the detector, as mentioned in the previous section. This can be resolved by moving the camera further away from the CCD. For the grid parameters used throughout this chapter (340 μm aperture width for a bar width of 40 μm), the lower limit on Fresnel number was determined to be 0.4 by extending the distance z_2 in the simulations. This affects both the spatially resolved spectrometry and the radius of curvature estimation techniques alike. However, using a larger aperture spacing can resolve this issue when considering the radius of curvature algorithm, but this will come at a reduced spatial resolution for the spectrometer.

The spectrometry method used here imposes the tightest constraint on the grid aperture size, period (γ), and distance z_2 as it has been shown to work best for Fresnel numbers between 2 and 3 [124]. For these values, the distance z_2 is large enough for the diffraction features to be well defined whilst also being low enough to prevent interference from adjacent squares for the given aperture spacing. It is important for the diffraction features to be well defined as this is generally correlated with a larger average size of the diffraction features, which makes them easier to detect experimentally as they can occupy a larger number of pixels. This also helps to reduce uncertainty in the retrieved spectrum. However, increasing z_2 to larger distances will push the diffraction towards the Fraunhofer regime, where no correlation can be made between different spatial regions of the diffraction pattern.

6.5 Single-image characterization of a capillary high-harmonic source

In this section the spectrometry and radius of curvature retrieval techniques described in sections 6.2 and 6.3 are applied to the output of a capillary high-harmonic source as a proof-of-principle demonstration of the characterization method. The development and optimization of this high-harmonic source formed earlier work, and is documented in Refs. [31, 109, 110, 111, 127]. First, the experimental setup used to collect the diffraction data is described, and the spatially resolved XUV spectrum is calculated before the radii of curvature of the XUV beam are retrieved in the x- and y-directions. Assuming a parabolic phase profile, the radii of curvature are used to back-propagate the spatial intensity distribution of each harmonic over the distance from the grid to the source, which allows for the wavelength resolved intensity distribution at the generation region to be retrieved.

Figure 6.6 shows the experimental setup used for the beam characterization. The nomenclature matches that used in figure 6.1. The high-harmonic XUV radiation was generated in argon gas by focusing the 790 nm, 40 fs, 0.8 mJ pulses (1 kHz repetition rate) from a Ti:Sapphire laser into the 150 μm diameter core of a silica capillary

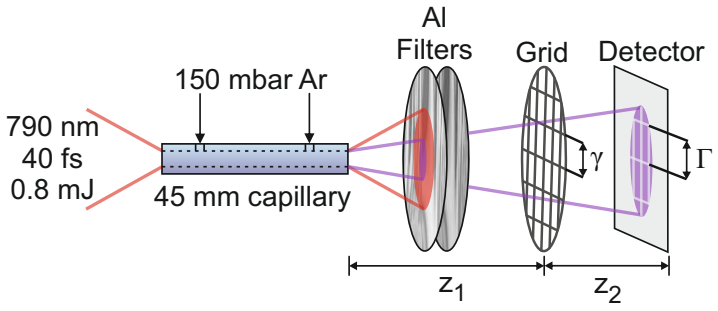

FIGURE 6.6: Schematic of the experimental setup. The distances $z_1 = 65$ cm and $z_2 = 45$ cm remained fixed for the data presented in this section. Variables γ and Γ denote the period of the grid and of the projected diffraction pattern in the plane of the detector, respectively.

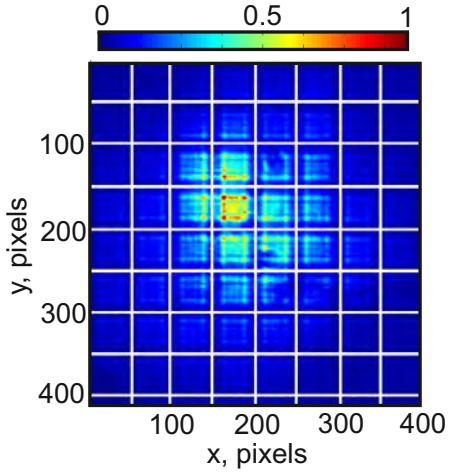

FIGURE 6.7: Normalized intensity plot of the Fresnel diffraction data. The Fresnel number for this geometry was ~ 2. Γ was approximately 620 μm for the capillary high-harmonic source.

(see section 5.3) using a 500 mm focal length plano-convex lens. A capillary length of 45 mm and argon at a pressure of 150 mbar were chosen as this combination produced spatial and temporal compression of the pulses very close to the output end of the capillary, thus allowing efficient XUV generation with minimal reabsorption by the argon gas [109, 110, 111]. Two 200 nm thick aluminium filters were used to preferentially reflect and absorb the residual infrared and only transmit the XUV through to the detector. A square grid with 340 μm apertures separated by 40 μm nickel wires (repeat period of $\gamma = 380$ μm) was placed in the beam at a distance $z_1 = 65$ cm from the end of the capillary in order to create a near field diffraction pattern, and a 1024×1024 pixel CCD detector (Andor, 13 μm square pixels) was positioned at a distance of $z_2 = 45$ cm from the grid to capture the near field diffraction image.

Figure 6.7 shows a diffraction pattern recorded experimentally with an exposure time of 50 ms, corresponding to 50 laser pulses with an estimated XUV flux of 2×10^{12} photons per second at the exit of the capillary. The white lines superimposed onto the data mark the projected shadow pattern of the grid, and the positioning of the line centres

was achieved by finding the minima of the fitted cubic smoothing splines, as discussed in the preceding sections.

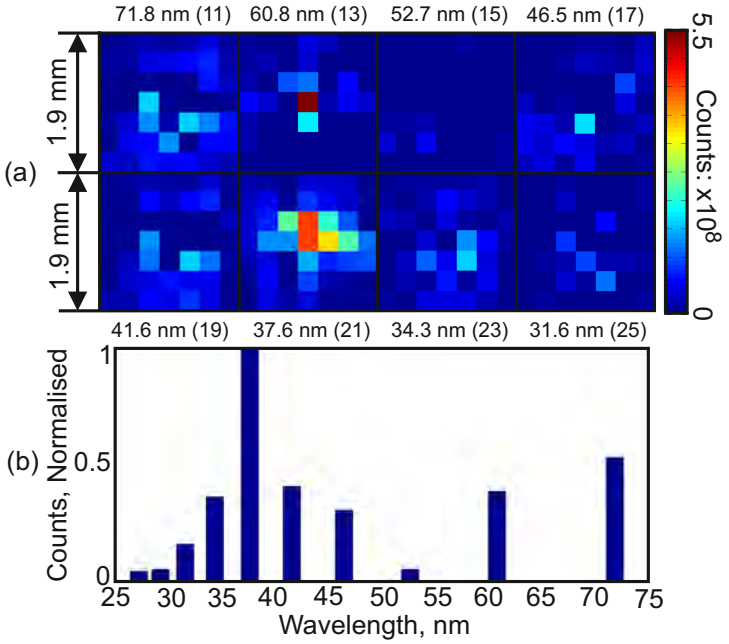

FIGURE 6.8: (a) Calculated XUV spectral intensity distributions in the plane of the grid for the eight harmonic orders with the highest powers. Each square block in the intensity patterns corresponds to one square of the Fresnel diffraction data oultined by the white grid in figure 6.7. (b) the high harmonic spectrum retrieved by spatially integrating the calculated spectral intensity distributions in a).

In order to combine the spectrometry technique and radius of curvature estimations (as described in section 6.3), the intensity profiles of each harmonic order must be calculated first so that they can be used as input for the radius of curvature estimation algorithm. The spatially resolved spectrometry technique was therefore used first, and the calculated harmonic intensity distributions are shown in figure 6.8a. This figure is ordered such that the long wavelength data is shown in the top left, and short wavelength data is shown in the bottom right, with the wavelength value and harmonic number shown above and below the intensity distributions. The spatial extent of the intensity distributions is shown to be 1.9 mm on the left hand side of the plot. The colour bar indicates CCD counts. The resolution of this image appears low due to the 'block' nature of the data, but this is an artefact of the grid method and is indicative of the resolution limit that the grid period imposes. Spatial integration of the calculated distributions produces the spectrum shown in figure 6.8b, which is similar to that which would be recorded by a conventional grating-based spectrometer [123] within the constraints of the linewidth and harmonic peak wavelength assumptions outlined in section 6.2.

Having calculated the spectral intensity pattern shown in figure 6.8a, the next step is to extract the radius of curvature of the high-harmonic beam in both the x- and the

y-directions from the diffraction data shown in figure 6.7. This was done using the algorithm outlined in section 6.3, using the spectral intensity distributions as the input field distributions for the algorithm ($A_0(x, y, z_1, \lambda)$ in equation 6.2). The resulting fit functions for the x- and y-directions as defined by $\Delta\Gamma = |\Gamma_{\text{exp}} - \Gamma_{\text{sim}}|$ are given in figure 6.9. This figure shows how $\Delta\Gamma$ varies with each radius of curvature value in the user-defined set, which ranged from 64.5 cm to 68.2 cm. The minima for these functions indicate the best fit radius of curvature values for the XUV beam, which are 66.3 cm in x and 66.6 cm in y. The corresponding difference between experimental and simulation values for Γ was 0.06 μm for a projected grid period of 620 μm.

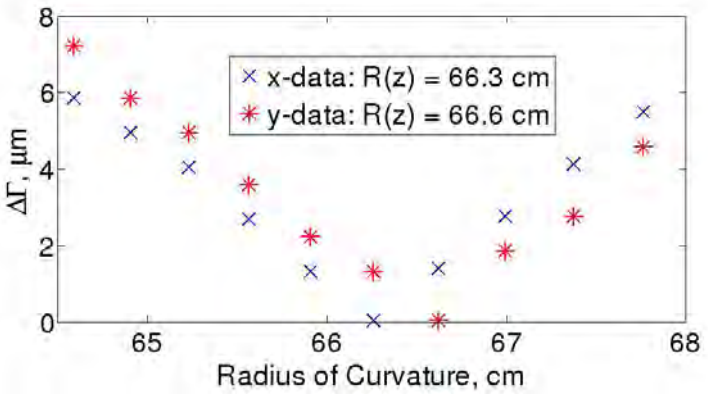

FIGURE 6.9: $\Delta\Gamma$ for each radius of curvature used in the diffraction simulations. The curves represent the modulus of the difference between the projected square sizes of the experimental and simulated data in the x-direction (crosses) and y-directions (asterisks). The best-fit radii of curvature values are 66.3 cm in x and 66.6 cm in y.

An attraction of the ability to determine the radius of curvature is that when moving on to using the spatially resolved harmonic spectrum (figure 6.8a) and the radius of curvature data (figure 6.9), it was possible to back propagate the spectral intensity distributions and obtain an estimate of the spatial profile of the harmonic orders at the output of the Ar-filled capillary. The spectral intensity distributions in figure 6.8a were multiplied by a parabolic phase corresponding to the best fit radii of curvature. The propagation axis for the phase calculations applied to all of the harmonics was centred on the intensity weighted centroid of the total XUV spot retrieved through the summation of the harmonic intensity distributions. The numerical beam propagation also starts with the assumption of a flat phase profile at the generation region. ASM was then used to back propagate the individual spectral intensity distributions, retrieving the spatially resolved XUV intensity at the capillary exit as a function of harmonic order, and the results are shown after normalization in figure 6.10. This figure is arranged in the same manner as figure 6.8a, with key differences being the normalization of each harmonic intensity to its maximum value, and the reduction in spatial extent of the images to 0.096 mm (shown to the left of the figure). The XUV spot size at the output of the capillary averaged across all harmonics was approximately 10 μm (intensity FWHM) with

an estimated error of 5% arising from the radius of curvature and distance measurements. This agrees very well with numerical simulations of the Ti:Sapphire laser spot size after the spatial and temporal compression in the capillary [109], where it was found that the driving field undergoes spatial compression through mode beating to produce a spot size of approximately 10 μm FWHM, significantly smaller than that of the TEM_{00} mode of the capillary ($\sim$50 μm), giving a peak intensity of 0.6×10^{15} W/cm^2.

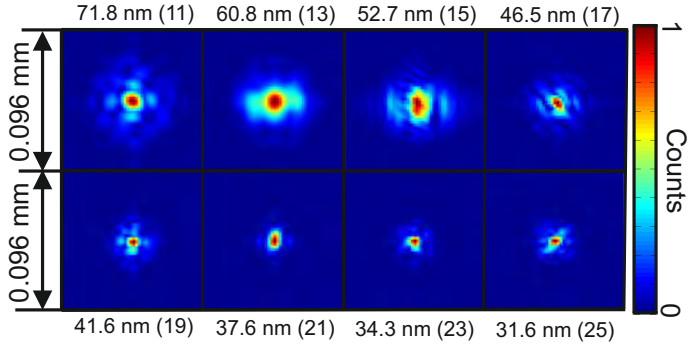

FIGURE 6.10: The normalized XUV intensity profiles at the capillary output, calculated using the smoothed intensity distributions of figure 6.8a) multiplied by parabolic transverse phase profiles with curvatures corresponding to the radii estimated by the algorithm.

The pixilation effect shown in figure 6.8a made it necessary to smooth the distributions shown in that figure before the ASM propagation was performed. The smoothing process was found to have a negligible effect on the size and shape of the reconstructed

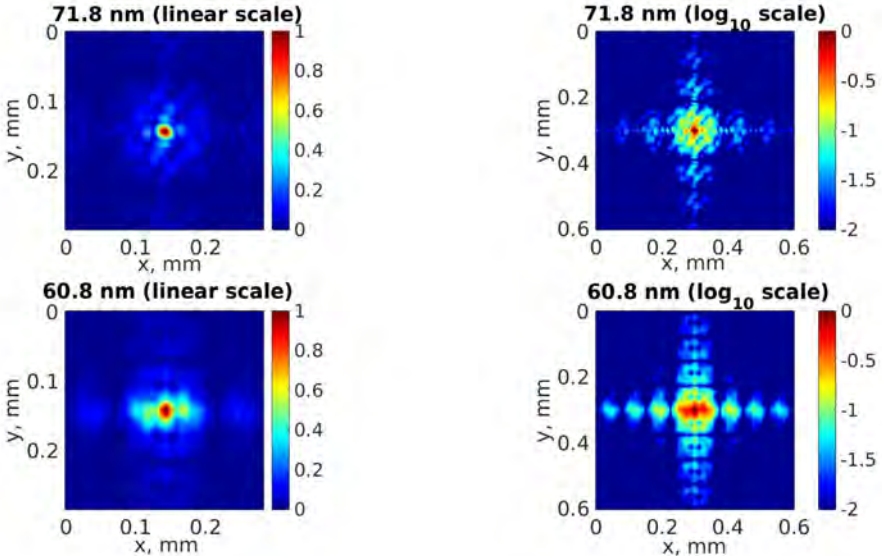

FIGURE 6.11: Reconstructed XUV generation spot for the 71.8 nm and the 60.8 nm harmonics, using the calculated data shown in figure 6.8a) without spline smoothing. The top row shows the data for wavelength 71.8 nm on a linear and log scale (left and right, respectively). The second row shows the same, but for harmonic wavelength 60.8 nm.

spot, and was included in order to remove a 'ringing' effect which was otherwise observed to extend beyond the capillary diameter. This effect is shown for harmonics with wavelength 71.8 and 60.8 nm in figure 6.11, where the intensity distributions are again normalized to their maximum value. It is seen that there is little change to the spot size and intensity distribution within 50 μm either side of the central spot, as the 71.8 nm XUV spot shows the four lobes which are apparent in figure 6.10, and the two peaks at either side of the central maximum in the 60.8 nm distribution are also reproduced. However, low amplitude oscillations extend to beyond 0.3 mm either side of the central spot (and therefore beyond the capillary core diameter). These are caused by the hard edges in the inferred spectral intensity distributions shown in figure 6.8a, which result from the assumption that the harmonic intensities are flat across each grid square. It was also necessary to interpolate the calculations in figure 6.10a onto a finer numerical grid before the back propagation, as the generation spot size for this data set is smaller than the pixel size of the detector used.

6.6 Limitations and future work

The back-propagation step for imaging the XUV generation region is limited predominantly by the cubic smoothing spline fitting and the ringing which occurs in its absence. The uncertainty introduced by the spline may be reduced by using a smaller grid period, increasing the beam sampling. As this will reduce the size of the square apertures which make up the grid, z_2 must also be reduced to comply with the Fresnel constraint discussed in section 6.4. This will, however, reduce the size of the diffraction features, which need to have a minimum squared size of four pixels to satisfy the Nyquist sampling condition. Detector pixel size therefore poses a fundamental limitation to the radius of curvature retrieval and back-propagation techniques, and may be restricted by commercially available detectors as well as what is available in the laboratory. Although using a detector with a smaller pixel size will allow for better beam sampling, doing so generally corresponds to an increased dark-count which reduces the contrast of the collected diffraction data. Although using longer exposure times can increase the signal above the noise, this will increase the data acquisition time for both the radius of curvature and spectrometry techniques when characterising low-flux sources.

Although the parabolic phase approximation is made under the assumption that it is flat at the generation region during the back-propagation step outlined in section 6.5 this is justified when considering the guided driving field and small infrared spot size which results from the optimized capillary source [109], and by recent direct measurements of the transverse phase of other high-harmonic sources in the literature [120]. This assumption allows for the transverse phase to be closely described by two degrees of freedom.

This, however, is not the case for XUV beams which have a modulated transverse phase profile as can result from astigmatic driving fields [128]. The capillary source analysed in this chapter is therefore not generic, but represents a proof-of-principle for the technique under the condition that the transverse phase profile may be parametrized by two orthogonal radii of curvature.

The single-exposure method outlined here may be generalized for more complex wavefronts by incorporating other phase retrieval techniques. A Shack-Hartmann integrator [129] is currently under development for this purpose. The displacement of the intensity centroid of the diffraction pattern for each grid aperture from the equivalent intensity centroid derived from a simulated plane-wave reference will be measured, and can then be used with a simple integrator to retrieve arbitrary transverse phase profiles. With this improvement, the single-exposure characterization method will be suitable for analysing the spatial properties of arbitrary XUV beams.

6.7 Summary

A method for analysing the spatial characteristics of an XUV beam has been introduced in this chapter, starting with a description of a previously reported spatially resolved spectrometry technique outlined in section 6.2. The method involved comparing the near-field diffraction pattern produced by a square aperture with simulated data to find the set of harmonic intensities which minimized the difference between the two. The main assumptions made when using this technique were outlined before a method for extending the technique to include radii of curvature estimations was described in section 6.3. These were made by comparing the magnification of the projected grid dimensions in comparison to simulated data, and the radii of curvature in the x- and y-directions which minimized the difference between the simulated and experimental data were given as the best-fit curvatures. Experimental guidelines were then discussed in section 6.4, with emphasis on the Fresnel number and how this was used to determine the correct diffraction regime when implementing this technique.

A capillary high-harmonic source was characterized in section 6.5 as a demonstration. The spatially resolved spectrum was retrieved with a peak wavelength of 37.6 nm and radii of curvature of 66.3 and 66.6 cm in the x- and y-directions, respectively. By smoothing the intensity distributions in the plane of the grid and multiplying by a parabolic phase with the radii of curvature given by the algorithm, it was possible to back-propagate them for an estimate of the frequency resolved intensity distribution at the generation region. The retrieved spot sizes for the harmonics were well matched to previously reported numerical data for the driving field of the same source. Section 6.6 included a discussion regarding the limitations and validity of the capillary analysis and

back-propagation approach, before key problems with generalising the current single-exposure analysis algorithm were identified. Current and future work in developing a Shack-Hartmann algorithm for retrieving arbitrary transverse phase profiles was described as a method for mitigating these problems.

Chapter 7

High-harmonic generation driven by a fibre CPA system

7.1 Introduction

In order to reach the high intensities required for HHG the output of the fibre CPA system must be focussed to a sub-10 μm spot size (intensity FWHM), which is roughly an order of magnitude lower than that used with traditional Ti:Sapphire driving lasers. As such, the number of atoms involved in the HHG process becomes an important parameter for achieving a usable flux. The most obvious solution would be to increase the gas pressure in the interaction region, but this also decreases the XUV absorption length and puts strain on the vacuum pumps to quickly remove excess gas from the beam path, and this was indeed found to be the limiting factor on XUV flux given the vacuum equipment that was available.

Alternatively, the interaction region may be optimized by selecting the appropriate focal length focussing optics for the input beam parameters to maximize the volume over which tunnel ionization dominates. This method was adopted and a telescope was designed for this purpose, allowing for XUV to be generated with a flux of 10^{11} photons/sec (average power of approximately 400 nW) as measured by an XUV photodiode. This corresponds to a state of the art conversion efficiency of 240 nW of XUV per Watt of infrared for both linearly and nonlinearly compressed single-fibre CPA systems. The single exposure characterization method outlined in Chapter 6 was then used with this efficient source for the first account of the spatial properties of high-harmonic light generated using a fibre CPA system.

This Chapter is structured as follows. Section 7.2 describes the vacuum chamber system used for the flux, spectrometry, and radii of curvature measurements, as well as

the photodiode and filter housing, and the focal optics. The method used to optimize the XUV signal is outlined in section 7.3, before the XUV is characterized in section 7.4. The photon flux and average XUV power detected are calculated in section 7.5, before a comparison between the generation efficiency of the fibre CPA system and others in the literature is drawn. Directions for possible improvements are considered in section 7.6 before the Chapter is summarized in section 7.7.

7.2 Experimental setup

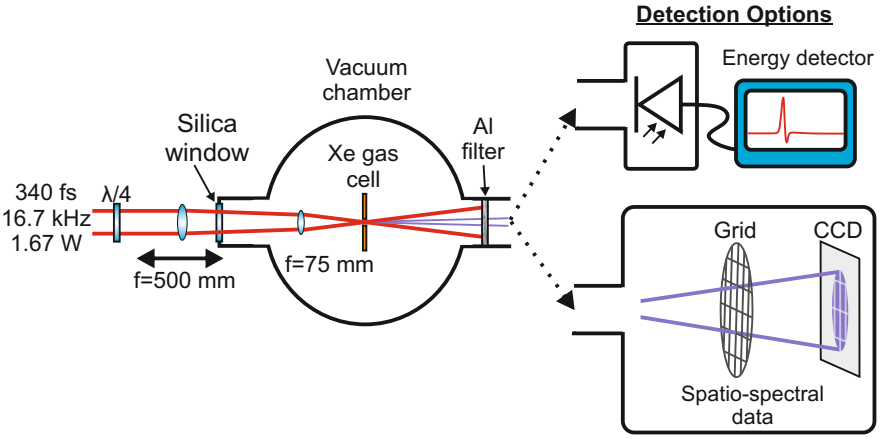

FIGURE 7.1: Schematic of the XUV generation and detection setup used with the fibre CPA system. The diode and camera were in separate vacuum chambers which could be attached to the chamber used for XUV generation. The energy detector was an Al-coated XUV photodiode with a low noise amplifier. The spectrum was reconstructed using the method outlined in chapter 6.

To demonstrate that the fibre CPA system was suitable for XUV generation, a test-bed vacuum system and diagnostics were set up as shown schematically in figure 7.1. A low pressure xenon gas cell was positioned at the focus [130]. Using this setup, the signal from an XUV photodiode was used to estimate the XUV flux and conversion efficiency from the infrared. The spectrum and radius of curvature of the XUV were measured using the methods outlined in chapter 6, and refs. [123, 131]. For all of the XUV generation experiments, the standard technique of using the differential short and long wavelength transmission characteristics of an aluminium filter (200 nm thick) was employed to separate the residual infrared from the XUV output. The XUV transmission window of aluminium extends from 17 to 80 nm [25, 132, 133], so all detected XUV is expected to be in this wavelength band.

7.2.1 Filter and XUV photodiode housing

The photodiode housing (designed by Dr. Thomas Butcher, Dr. Jonathan Price, and Simon Butler) is shown in figure 7.2 (adapted from ref. [31]). The housing was made using aluminium tubing with a minimum inner diameter of 5 mm. A small recess was made at the entrance to the housing which was deep enough for an aluminium filter to sit in. A deeper recess was made in the back of the photodiode housing, and an insulating base which sat in this recess and was held to the body of the housing with screws supported the photodiode (labelled photodiode insert in the diagram). A front-cap was also included to aperture the beam at the entrance to the housing. This reduced the thermal load on the aluminium filter by reducing the incident residual infrared without attenuating the XUV signal. The front cap also had a wider diameter than the body of the photodiode mount to help block scattered infrared from passing through to the back of the housing where it would have a higher chance of being detected by the photodiode. A gas inlet was drilled into the top of the housing, which prevented the aluminium filter from tearing while the chamber was being pumped down. Carbon tape was used around each join to improve the optical signal-to-noise ratio of the photodiode reading.

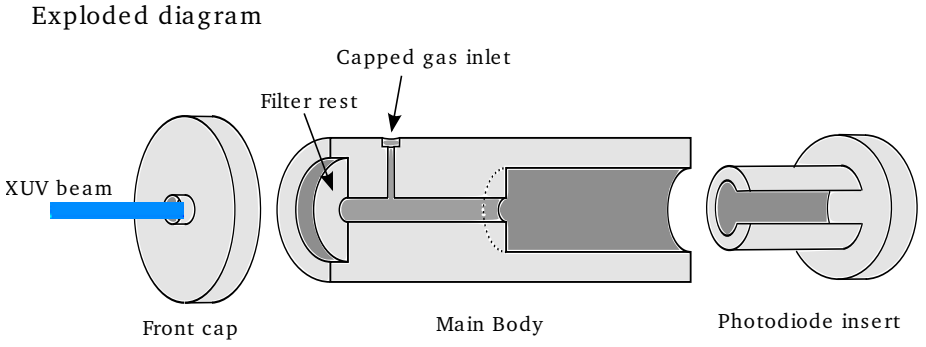

FIGURE 7.2: Schematic of the Photodiode mount (adapted from [31]).

The XUV transmission of the aluminium is dependent on both the thickness of the aluminium and the surface oxide layers. The aluminium filters used in these experiments were 200 nm thick, and the oxide layer is estimated to be on the order of 10 nm thick. The detected XUV signal will therefore depend on the transmission of the 200 nm aluminium, and the transmission of two 10 nm aluminium oxide layers (one for each surface of the filter). Typically, it was found that an acceptable OSNR for the XUV detection was achieved with two 200 nm thick aluminium filters, which resulted in ∼40 nm of aluminium oxide. Coating the XUV photodiode with a layer of aluminium meant that one of the filters could be removed, which improved the OSNR of the XUV detection by attenuating the infrared and minimizing excessive absorption by the aluminium oxide, as this could only form on the exposed surface of the photodiode thus reducing the total oxide layer thickness to ∼30 nm.

When using the CCD for the spatially resolved spectrometry (spatio-spectral) data, two aluminium filters were used. A brass tube was designed which held both the filters and the spectrometry grid in a length of KF40 vacuum tubing between the gas cell and the CCD. During the spectrometry measurements, the XUV photodiode and electronics were removed from this KF40 tubing and replaced by this brass insert and a vacuum chamber which housed the CCD.

7.2.2 Vacuum chamber design

A photograph of the generation chamber and XUV photodiode setup is shown at the top of figure 7.3. The generation chamber was cylindrical with an internal diameter of ∼17 cm. A f=75 mm aspheric lens, which formed part of the focussing optics used for the generation (discussed in section 7.2.3) was positioned at the entrance to the chamber (left of the photograph). A gas cell was made from a length of flattened 1/4-inch copper pipe and positioned at the focus. It had an interior depth of ∼500 μm, with two 500 μm holes drilled through either side so that the focussed driving beam could pass through. One end of the copper piping was capped so that it could be mounted in a standard 1/2-inch post holder, and the other end was connected to a gas line and regulator so that xenon could be passed through the cell with variable pressure. Following this, a custom designed aluminium filter and photodiode mount was slotted into a KF40 port positioned after the gas cell, and a KF40 cross-piece was used to house the photodiode wiring. A low-noise amplifier was attached to the back of the cross-piece using a vacuum compatible BNC feed-through flange. A pressure gauge was attached to the side of the generation chamber so that the background xenon pressure could be monitored during the experiments. This information was later used to calculate the XUV flux from the photodiode signal and spectrum.

The chamber was evacuated using both a turbomolecular pump and a rotary backing pump, which were connected in series. A gate valve and a regulator were assembled in the vacuum line so that the chamber could be pumped down at a continuous and slow rate until the background pressure fell below 5 mbar. This precaution reduced the likelihood that the filter would tear while the chamber was being pumped down.

The photograph at the bottom of figure 7.3 shows the vacuum chamber setup used for the spectrometry and radius of curvature measurements. The generation chamber remained unchanged for both the photodiode and spectrometry experiments, but the cross-piece and amplifier were exchanged for a secondary chamber which housed an XUV CCD. An extra length of KF40 tubing was attached between the generation chamber and the CCD chamber and contained the filters and grid (as mentioned in subsection 7.2.1). The length of the KF40 tubing was chosen to allow for the gas cell, grid, and CCD

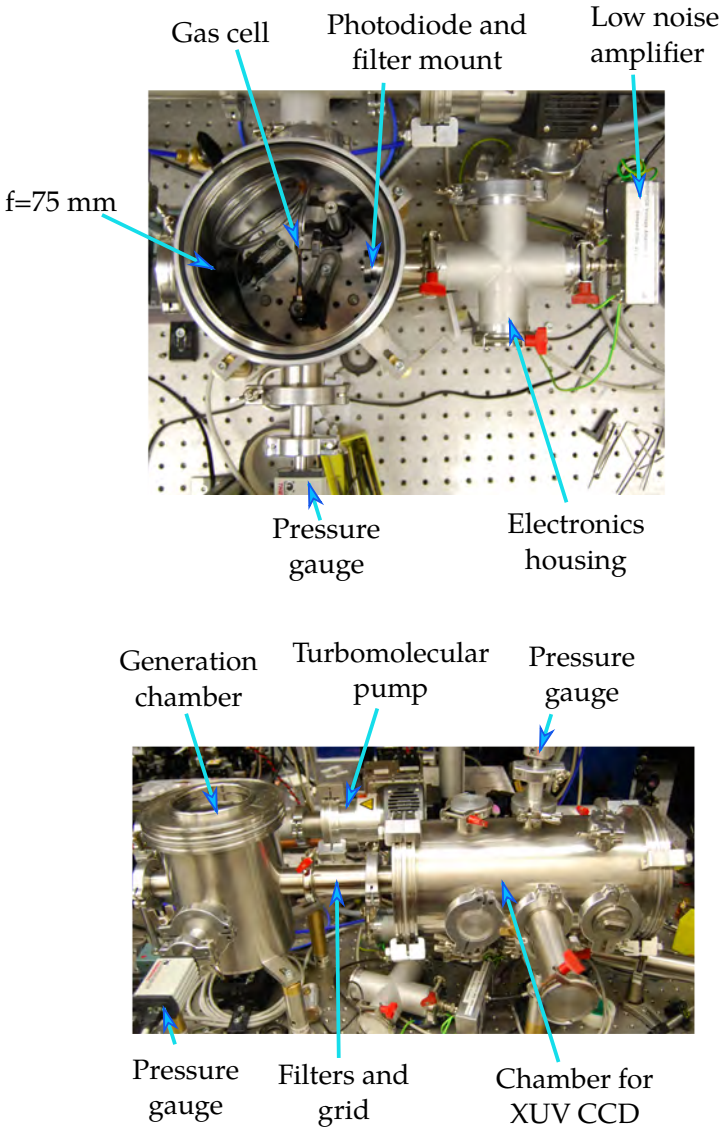

FIGURE 7.3: Photographs of the setup. Top: generation optics and housing for the photodiode electronics. Bottom: vacuum chamber setup for the spatio-spectral characterization.

separations to be set to the correct position to comply with the Fresnel constraint of the spectrometry method (see section 6.4), and will be considered in more detail below. The same vacuum pump arrangement was used for this chamber as with the photodiode setup, but both chambers were connected using KF40 tubing to ensure even pumping either side of the filters to reduce the likelihood that they would become damaged. The same gate valve and regulator arrangement was used, and an extra pressure gauge was added to the CCD chamber so that the pressure either side of the filters could be monitored.

7.2.3 Focussing optics

By controlling the beam waist size at the focus it is possible to maximize the volume over which tunnel ionization can occur. Simulations using the ABCD matrix formalism for beam propagation were performed for a number of different focal lengths with the aim of finding the maximum generation volume around the focus for which the Keldysh parameter, γ (equation 5.1), was less than 1, thus maximizing the tunnel ionization volume. The result was that a focal length of approximately 70 mm was appropriate, and given the size of the available vacuum chamber this required that the lens was positioned inside the chamber. Therefore to provide the ability to scan the focus axially through the gas cell in order to balance the Gouy and atomic contributions to the phasematching (equations 5.28 and 5.24), a telescope was constructed using a 75 mm best form lens (placed inside the vacuum chamber) and a 500 mm plano-convex lens (placed outside the vacuum chamber). The focal length of this telescope could be adjusted about a median value of approximately 6.8 cm depending on the separation of the two lenses. The 500 mm plano-convex lens was mounted on a rail so that it could be shifted axially along the beam-path to scan the focus through the gas cell.

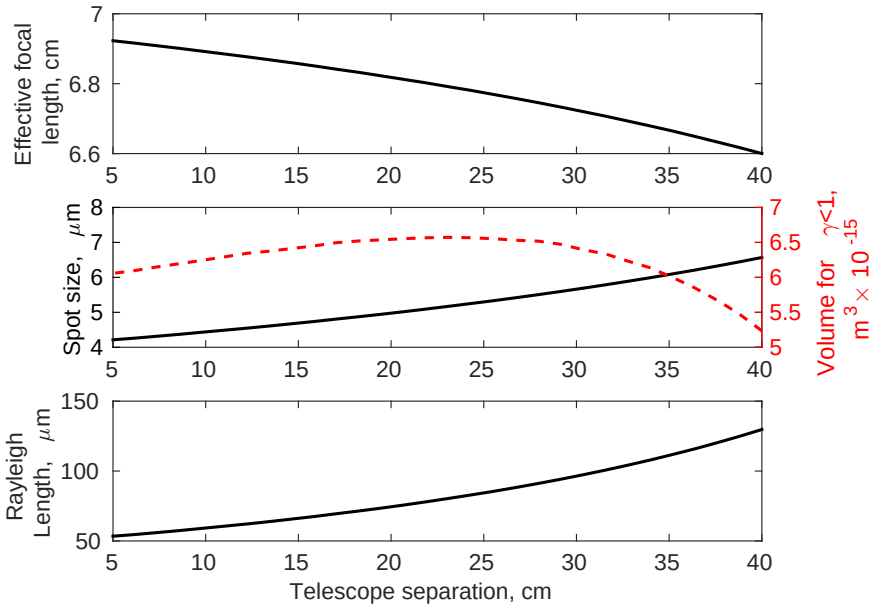

FIGURE 7.4: Simulations showing the effective focal length, spot size, and Rayleigh range for the telescope. The central plot also includes the calculated focal volume for which $\gamma < 1$ (red dashed line), and shows that the tunnel ionization volume is maximized for a lens separation of 24 cm.

Figure 7.4 shows the simulated effective focal length, spot size, and Rayleigh length for the focal setup with an input beam radius of 3.3 mm ($1/e^2$ intensity radius) and M^2=1.07 (see sections 4.2 and 4.3). The calculation for focal volume over which $\gamma < 1$ is included as the red dashed line in the spot size plot (centre). This volume is maximized

at 6.6×10^{-15} m^3 for a telescope separation of approximately 24 cm, which corresponds to an effective focal length of 6.78 cm, a intensity FWHM focal spot of 5.1 μm, and a Rayleigh length of 78 μm. The peak intensity for the 340 fs, 100 μJ pulses emitted by the fibre CPA system was estimated to be 1.8×10^{14} W/cm^2, which is high enough to generate XUV. The telescope lens separation was therefore set to an initial position of 24 cm during the experiments in order to maximize the tunnel ionization volume at the focus.

Figure 7.4 also shows how the effective focal length, spot size, and Rayleigh range may be adjusted by changing the telescope separation. Bringing the 500 and 75 mm lenses closer together increases the effective focal length, thus translating the focus to the back of the gas cell. Moving the lenses further apart has the opposite effect. Changing the telescope separation by 7.5 cm either side of the 24 cm central position adjusts the effective focal length by ∼0.7 mm, which is greater than the interior depth of the gas cell, allowing for the Gouy and atomic phase mismatches to be balanced adequately. Although the spot size does change with the telescope separation the variation in tunnel ionization volume is reasonably small over the ∼0.7 mm change in effective focal length (∼5%), indicating that the volume over which $\gamma < 1$ is not reduced beyond ∼ 7% as the focus is swept through the gas cell.

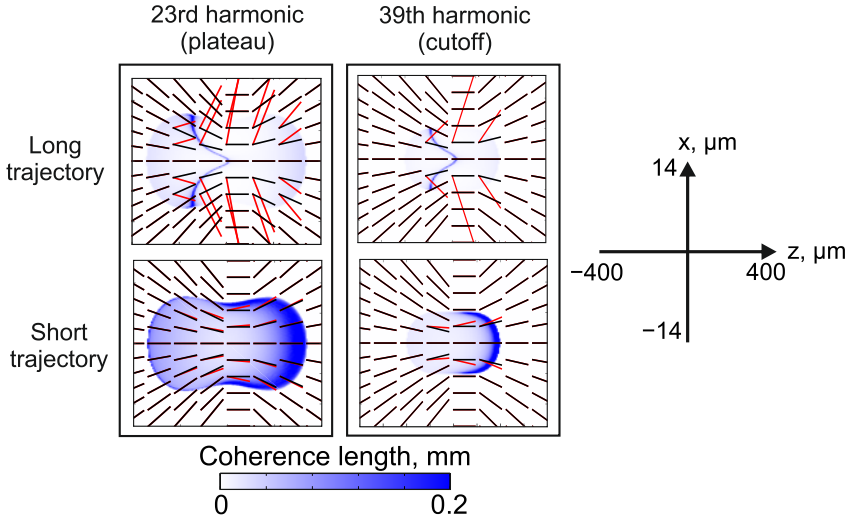

FIGURE 7.5: Simulation of the coherence length for the 23$^{\text{rd}}$ (plateau) and 39$^{\text{th}}$ (cutoff) harmonics for a focal length of 6.78 cm ($I_0 = 1.8 \times 10^{14}$ W/cm^2). Long and short trajectories are included in the top and bottom rows and the black and red lines superimposed onto the images indicate the directions of the driving and harmonic field k-vectors, respectively. The scale for each image is given on the right hand side.

The Gouy and atomic phase contributions to the coherence length are shown in figure 7.5 for an estimated plateau (23rd) and cutoff (39th) harmonic generated using the fibre CPA system and the focussing optics described. For these simulations the

example outlined in ref. [112] was followed and involved calculating the quasi-classical action using equation 5.25, including the radial and longitudinal dependence on the momentum. The colorbar indicates how the coherence length varies within a region where the intensity is high enough to generate the harmonic under the semi-classical model outlined in section 5.1. The black and red lines superimposed onto the images indicate the directions of the driving and harmonic field k-vectors, respectively. Scale axes are given to the right of the figure.

For both the plateau and cutoff harmonics, the long trajectories provide a limited region towards the centre of the focus where phasematching can be achieved. The 23rd harmonic sees some increase in coherence length towards the back edges of the focal region. Furthermore, the generated XUV field is highly divergent (as indicated by the red k-vectors) and will have an annular structure due to the spatial variation in the divergence angle. This differs from the short trajectories which, for both harmonics, show large regions of good phasematching after the focus, with a larger region of slightly decreased coherence length towards the left for the 23rd harmonic. The spatial variation in coherence length is similar for both harmonics, although the region is larger for the plateau harmonic as it may be generated by a lower intensity driving field. This indicates that the optimum position for the gas cell will be approximately 350 μm after the focus, which not only maximizes the amount of XUV generated but also limits reabsorption of the XUV by the higher pressure gas in the cell. The beam divergence is also similar to the driving field and shows little spatial variation, indicating that the XUV beam will remain roughly the same size as the driving field and have a smooth profile. As a result, the experiments described here account predominantly for the short trajectory harmonics.

7.3 XUV photodiode measurement and signal optimization

The focal length and backing pressure were adjusted iteratively to produce the best XUV generation efficiency as determined by the maximum photodiode signal voltage read from an oscilloscope trace. An averaging function was used on the oscilloscope and calculated the mean signal voltage over 256 samples to reduce the OSNR on the signal reading by a factor of 16, which provided a noise floor of $\sim$1 mV. The XUV flux could be efficiently optimized using the photodiode as it provided real-time data about the generation efficiency.

For each backing pressure applied, the best gas cell position was found to be just after the focus (between 0.3–0.5 mm), therefore matching the coherence length calculations given in figure 7.5. By maximizing the phasematching each time in this way,

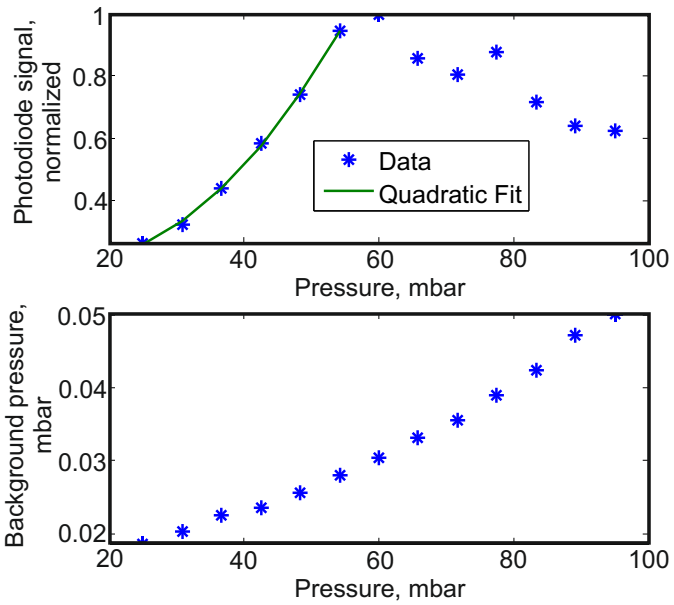

FIGURE 7.6: Top row: Variation in XUV photodiode signal (normalized) with backing pressure in the gas cell. Bottom row: Increase in chamber background pressure with gas cell pressure.

a quadratic increase in XUV intensity with backing pressure is expected, as the XUV field will scale with the number of generating atoms within the region of best phase-matching. This is shown in the top row of figure 7.6, where the normalized photodiode data has a quadratic dependence on the xenon backing pressure before saturating at a maximum of 60 mbar. The dimensionless attenuation coefficient for Xe at 40 nm and a pressure of 1 atm is approximately $\beta = 2.44 \times 10^{-5}$ [133], which gives an absorption length of 261 μm when defined as the length over which intensity is reduced to 1/e of the initial value ($L_{\text{abs}} = 1/(\beta k)$). This parameter will scale linearly with pressure, so the absorption length for 60 mbar is 1.57 mm, which is approximately twice as large as the total length over which the 23rd harmonic can be generated according to simulations (figure 7.5). Residual Xe gas in the chamber therefore poses the main limitation on the generation and detection efficiency of the XUV, and this is also seen in figure 7.6. The lower plot shows the linear increase in background chamber pressure with Xe gas cell pressure. Beyond 60 mbar the chamber pressure exceeds 35 μbar, after which the increase in XUV generation efficiency with cell backing pressure is exceeded by the increase in background absorption. Increasing the Xe pressure in the cell above 60 mbar reduced the detectable level of XUV due to this effect, and as a result the cell backing pressure remained fixed at this pressure.

Once the flux was optimized, a simple test was performed to confirm that the observed signal was produced by high-harmonic generation as opposed to fluorescence. As described in chapter 5, a circularly polarized driving field will not allow for recombination of the electron with its parent ion, and a small degree of ellipticity will heavily attenuate

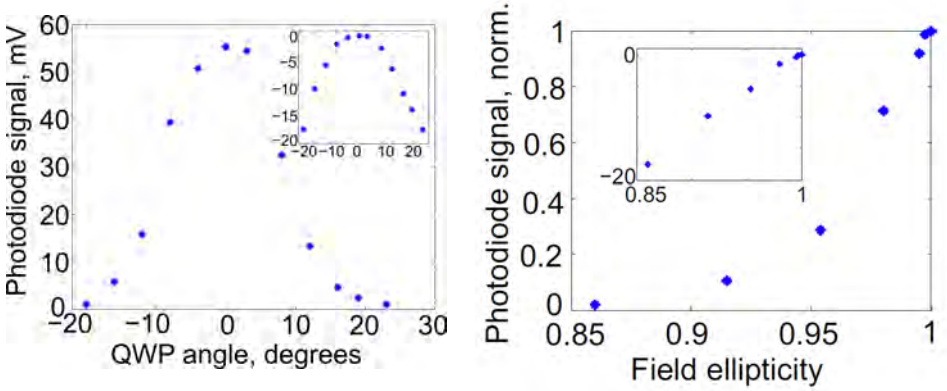

FIGURE 7.7: Left: Photodiode signal as a function of QWP angle (inset: dB scale). An extinction of 17.5 dB was achieved with increased ellipticity of the driving field before the signal could no longer be detected above the noise. Right: Normalized photodiode signal as a function of ellipticity of the driving field (inset: dB scale).

the XUV signal. In practice, a quarter waveplate was placed in the beam before the 500 mm plano-convex lens (shown in figure 7.1). The photodiode signal was recorded as a function of waveplate angle, and is shown in figure 7.7 (linear polarization was given for a waveplate angle of 0°). Beyond ±20° the XUV signal could not be detected above the noise, which led to a maximum measurable attenuation of 18 dB. The rapid decrease in photodiode signal as a function of ellipticity is given to the right of figure 7.7 (shown to be a power-of-ten relationship by the log plot inset), in which ellipticity has values on the interval [0;1] for circular and linear polarization, respectively.

7.4 Single-exposure characterization of a fibre CPA high-harmonic source

Once the XUV flux had been optimized using the photodiode arrangement, the single-exposure characterization method for retrieving the spatially resolved XUV spectrum and radius of curvature (outlined in chapter 6) was used to characterize the XUV produced by the fibre CPA system. This was done using the setup described in section 7.2, and ASM simulations of the XUV diffraction were used to determine the correct source-to-grid (z_1) and grid-to-CCD (z_2) distances, as well as the aperture size and period (γ) of the grid used for the diffraction. These simulations were based on the assumption that the XUV source was point-like, which is justified due to the small focal spot of the fibre CPA in comparison to the required distances for the experiment (>10 cm). Using the simulations as a guide, transmission electron microscopy (TEM) calibration grids were chosen due to their availability and suitable size, and a microscope image of selected TEM grid (G100, Agar Scientific) is shown to the right of figure 7.8. The square apertures were 200 μm wide with a separation of 50 μm, giving a total period of

$\gamma = 250$ μm. The diagonal bars in two of the apertures towards the centre of the grid are not required for the characterization algorithm, which was adapted to accommodate for these two apertures. Grids without these features were not available, and no other grids with square apertures and suitable dimensions were available.

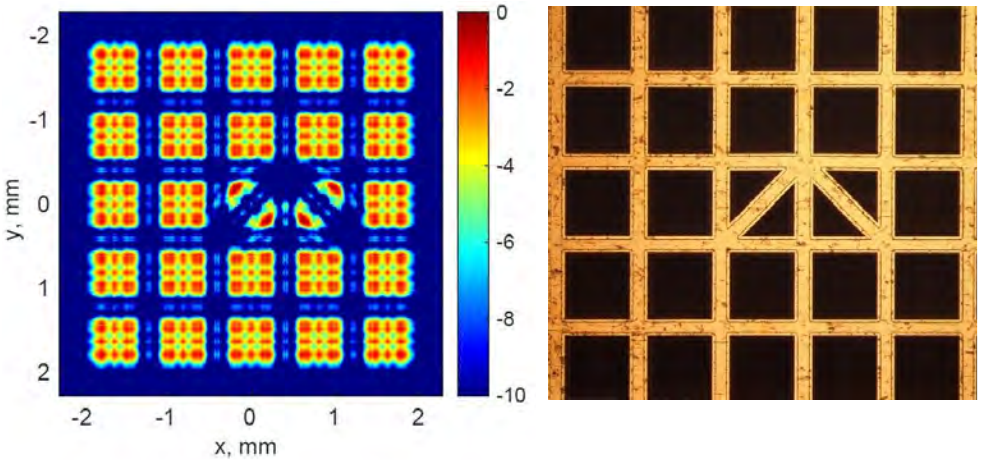

FIGURE 7.8: Left: ASM simulation of the grid diffraction for the expected XUV wavelengths and radius of curvature produced by the fibre CPA (dB). Right: The grid used for the spatially resolved spectrometry and radius of curvature measurements.

Distances z_1 and z_2 were also chosen using the ASM simulations, assuming an XUV field consisting of odd harmonics 19 to 27 of 1045 nm (55 to 38.7 nm) with equal amplitudes and flat spatial distribution. The best visual contrast between the maxima and minima of the diffraction patterns produced by each square of the grid was found for distances $z_1 = 11.5$ cm and $z_2 = 25$ cm, and this simulation is shown to the left of figure 7.8. The estimated error in these distances for the experimental setup is ± 2 mm. Due to the small focal spot required to generate XUV with the fibre CPA (and the resulting high XUV divergence), the modified version of the Fresnel number as given by equation 6.5 must be used to ensure that the setup is compliant with the Fresnel constraint outlined in section 6.4. Using a characteristic half-width of 100 μm for the apertures, distances z_1 and z_2 give a Fresnel number of 2.8, which is within the stated constraint. The estimated high divergence of the XUV beam also has the effect of increasing the size of the diffraction features. The area covered by the smallest diffraction feature in the simulation is approximately 64 pixels (at intensity FWHM and a pixel size of 13 μm), and so the Nyquist sampling condition is met and the pixel size constraint on the radius of curvature retrieval is eliminated for this experimental setup.

The simulation also shows that cross-talk between the diffraction patterns created by adjacent apertures is minimal, and restricted to the 9–10 dB level. The simulation also shows that cross-talk from the apertures with the diagonal bars to adjacent ones is insignificant, and very little distortion of the adjacent diffraction patterns is seen.

Although these apertures do not obey the Fresnel constraint (F≈ 1.6), they were included in the spectral analysis as the diffraction features which they produced showed some wavelength dependence. These apertures also have a two-fold rotational symmetry rather than four, and the symmetrization step was adjusted accordingly.

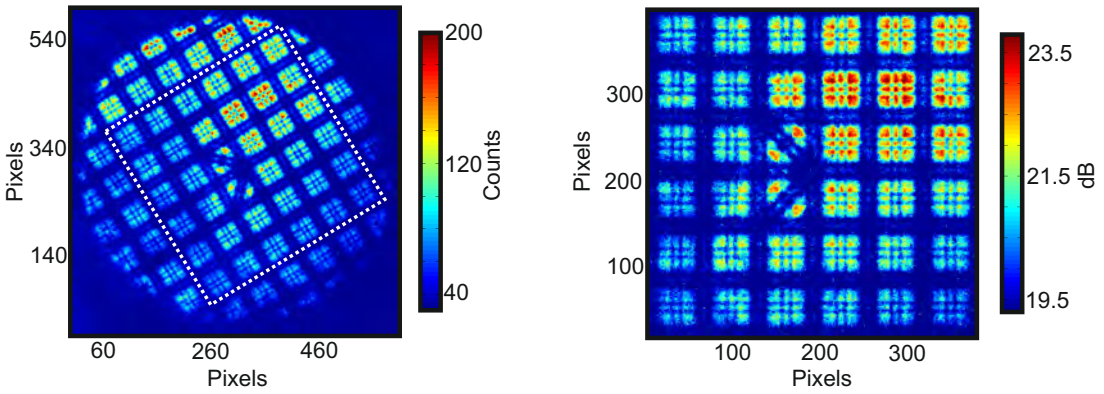

FIGURE 7.9: Left: grid diffraction image after background subtraction and cropping (linear scale). Right: The set of squares analysed using the spectral and radius of curvature algorithm introduced in chapter 6 (dB scale. Shown on a linear scale by the white dashed square overlaid onto the left image).

The left hand side of figure 7.9 shows the total XUV grid diffraction data on a linear scale taken from the fibre CPA system using the grid, distance, and optimum flux parameters described. The hard circular edge around the diffraction data is the shadowgram of the ∼3 mm diameter grid mount. This image was taken using a 1 megapixel XUV CCD (Andor Technologies) with a pixel size of 13 μm and 20 s exposure time, and the OSNR was reduced by cooling the CCD to $-25°$C and subtracting a second image taken with no Xe in the gas cell, thereby stopping the XUV generation so that residual infrared and back-scatter detected by the CCD could be removed. The white dotted square marks the region of the diffraction pattern which was analysed for the spatially resolved spectrum and radius of curvature data, and this region is shown on a logarithmic scale to the right of the figure. Despite the non-uniform intensity distribution of the diffracted light, the structure of the diffraction patterns produced by the individual squares of the grid is very similar to the simulation shown in figure 7.8. The cross-talk between adjacent squares is minimal, and the diagonal bars do not produce far-field diffraction features, matching the simulations. This region was therefore deemed suitable for the single-exposure characterization technique.

For the spatially resolved spectral analysis, odd harmonics from numbers 7 to 61 (149.3 nm to 17.1 nm) were included to ensure that the algorithm did not converge on spectra with components outside of the aluminium transmission band, but converged on the best estimate of the spectral intensities. This was the case, as all spectral components above and below 60 and 25 nm were returned with zero amplitude. The intensity distributions for the five strongest harmonics generated by the fibre CPA are given on a

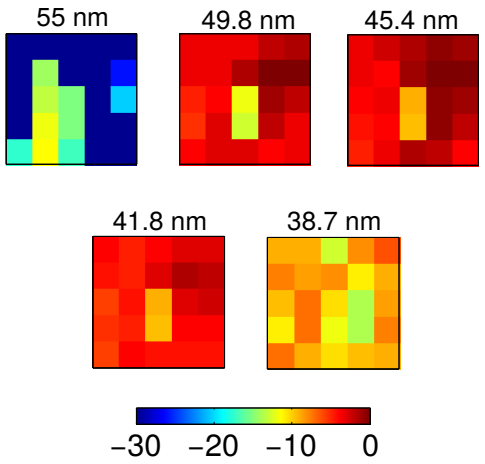

FIGURE 7.10: Intensity distributions of the strongest 5 harmonics in dB. The plots each contain 318 × 318 pixels (total area: 4.1 × 4.1 mm).

logarithmic scale in figure 7.10. The distributions are smooth, indicating little variation in generation conditions across the focal spot, attributable to the diffraction limited beam quality of the fibre CPA output and indicative of minimal nonlinear spatial pulse distortion of the driving field from the Xe gas before the HHG process takes place. The highest harmonic intensities occur for the 49.8, 45.4, and 41.8 nm spectral components (corresponding harmonic orders: 21, 23, 25) and the reduced amplitude for the two squares with the diagonal bars is reproduced by the algorithm.

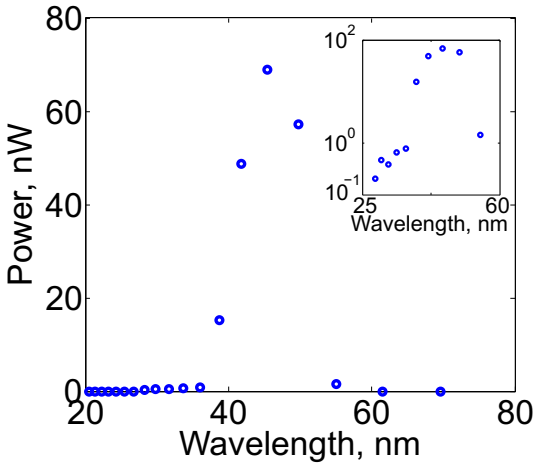

FIGURE 7.11: Spatially integrated spectrum for the cropped region shown in figure 7.9.

Spatially integrating the spectrometry data gives the total high-harmonic spectrum generated by the fibre CPA, and this is shown on a linear scale (logarithmic inset) in figure 7.11. The cutoff wavelength for Xe at an intensity of $1.8{\times}10^{14}$ W/cm^2 is approximately 21 nm. The spatially integrated spectrum shows wavelengths down to approximately 27 nm, therefore the system is not limited by the cutoff frequency, but by

the high ionization fraction over the long pulse duration and by the difficulty in phase-matching the higher harmonics, as described in section 5.4 and indicated by the small estimated area over which the coherence length for the cutoff harmonic is appreciable (shown in figure 7.5). The ionization fraction for the test-bed HHG setup is estimated to be 100% at the pulse peak, indicating that XUV generation is restricted to the first half of the pulse before the point at which this high peak intensity and hence high ionization fraction is reached.

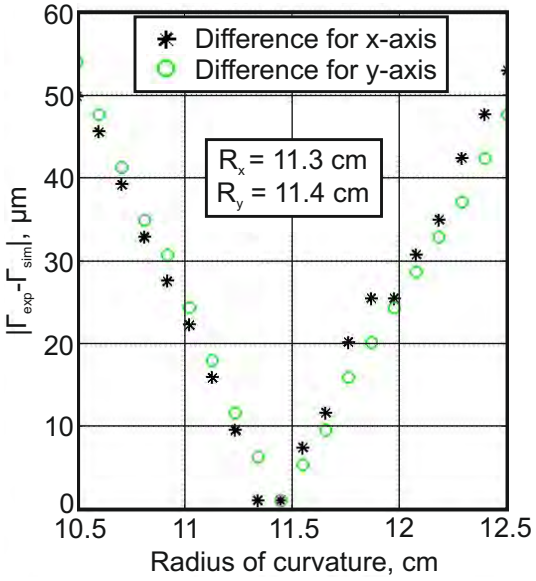

FIGURE 7.12: Fit functions for the radius of curvature in the x- and y-directions for the XUV generated by the fibre CPA system.

The output of the radius of curvature retrieval algorithm is shown in figure 7.12, and indicates that the radii of curvature measured 11.3 cm in x, and 11.4 cm in y. The value for x is seen to be degenerate for two consecutive values about the minimum. As discussed in chapter 6 this results when the radius of curvature of the beam is not an element of the user-defined array of test radii of curvature. The smallest value was chosen arbitrarily as the radius of curvature of the beam in the x-direction, but the true radius of curvature could take on values between 11.3 and 11.4 cm. Despite this uncertainty, the measurements match the distance between the gas cell and the grid within the ± 2 mm estimated distance error. As a result, the parabolic approximation for beam propagation over a distance much larger than the Rayleigh range is met. Given that the beam fills the 3 mm diameter aperture of the grid mount, a lower limit of 1.46° is estimated for the divergence angle of the XUV using the radius of curvature information.

7.5 XUV flux calculation and comparison with other sources

In this section the method used to approximate the average XUV power is outlined before it is used to form a comparison between the generation efficiency presented here and that reported in the literature.

The following relationship was used to estimate the number of photons per second detected by the XUV photodiode:

$$n_{\mathrm{ph/s}} = \frac{VC}{9200 q_e \delta} f_{\mathrm{rep}} \tag{7.1}$$

where V is the voltage read from the oscilloscope, $C = 2$ nF is the capacitance of the photodiode, q_e is the electron charge, δ is the overall transmission of the Xe gas, the aluminium and aluminium oxide on the filters, and f_{rep} is the repetition rate of the fibre CPA system (16.7 kHz). Considering the path length from the gas cell to the photodiode of approximately 13 cm with a typical background Xe gas pressure of 4×10^{-2} mbar and using the attenuation appropriate for XUV wavelengths between 20–80 nm we estimated δ to be in the 1.5–3% range. The factor of 9200 in the denominator corresponds to the gain in the amplifier.

Equation 7.1 gives a maximum flux of approximately 0.5–1 $\times 10^{11}$ ph/s based on the maximum observed photodiode signal of 70 mV. Using the photon energies and relative amplitudes of the harmonic wavelengths as inferred from the spectrometry technique used in section 7.4 the average XUV power is calculated to be 200-400 nW within the Al transmission band.

In order to establish a benchmark against which the XUV generation may be compared to others in the literature, an efficiency parameter was calculated for the highest XUV flux results from a number of fibre CPA systems using the following definition:

$$\eta = \frac{P_{\mathrm{XUV}}}{P_{\mathrm{IR}}} \tag{7.2}$$

The results of this calculation are given in Table 7.1. The output power which gave the best XUV flux was used for these calculations, and was taken at the output of the linear compressor so as to account for the inefficiency of any nonlinear compression stages used. This way, a better measure of conversion efficiency from the perspective of an end user is gained. All XUV powers were estimated from the data given in each paper if the value is not stated directly.

The fibre CPA pulse parameters for the systems in Refs. [21, 134] range from up to 400 μJ, 800 fs pulses at repetition rates of up to 500 kHz when linear compression is used, to 45 fs, 0.58 mJ pulses at 50 kHz when nonlinear compression is used ($\sim$ 1 mJ pulses before the nonlinear compression stage). The conversion efficiencies from the infrared to

Reference	**IR power**	**XUV power**	$\eta = \mathbf{P_{XUV}/P_{IR}}$
[134]	10 W	1-100 nW	1-10 nW/W
[21]	80 W	9.2 μW	120 nW/W
[22]	$\sim$ 165 W	600 μW	3600 nW/W
This work	1.67 W	400 nW	240 nW/W

TABLE 7.1: Comparison between the infrared to XUV generation efficiency between fibre CPA systems presented in the literature and that described in this thesis.

the XUV for these systems range from 1–120 nW/W. For the system used in this chapter η = 240 nW/W, which is higher than other systems by a factor of $\sim$ 2 in spite of the reduced pulse energy and repetition rate. This is attributed to the diffraction limited beam quality of the flexible fibre system in comparison with the degraded M^2 typically achieved from rod-type systems, the good stability of the fibre CPA as discussed in chapter 4, and the optimized phasematching and focal volume arrangement discussed in section 7.2.3.

The fibre CPA system described in Ref. [22] uses an array of four coherently combined Yb-doped rod-type fibres for the final amplification stage as well as dual-stage nonlinear compression to produce 130 μJ, 29 fs pulses at a repetition rate of 600 kHz and an IR to XUV conversion efficiency of 3.68 μW/W. This drastically increased efficiency may be explained when considering the peak power of $\sim$ 4.4 GW which would allow for a much longer focal length lens to be used for the generation, thereby increasing the number of atoms used in the generation process for a given gas pressure. The shorter pulse duration also reduces the free electron density, leading to better optimized phasematching conditions.

The XUV conversion efficiency produced by the fibre CPA system is roughly double that reported for other systems in the literature. However, further improvements to the conversion efficiency are possible.

7.6 Future work

In the short-term, further improvements to the focal arrangement have been tested using the ABCD matrix method. It was found that a telescope constructed using three lenses could provide a similar focal scan range with a much reduced variation in spot size (and therefore tunnel ionization volume) than that used for the XUV generation in this chapter. Figure 7.13 shows the effective focal length, spot size, and Rayleigh length for an f=-150 mm lens at a variable separation from an f=200 mm lens, which is then situated 5$\pm$1 cm away from the f=75 mm best-form lens. The simulations show that the focus can be swept through the gas cell with a change in laser spot size of only 800 nm

(FWHM intensity radius), which is significantly smaller than the current setup. This will allow for the phasematching to be decoupled from the intensity dependence of the generation efficiency more effectively, allowing for these two parameters to be explored independently and thereby improving the optimization procedure.

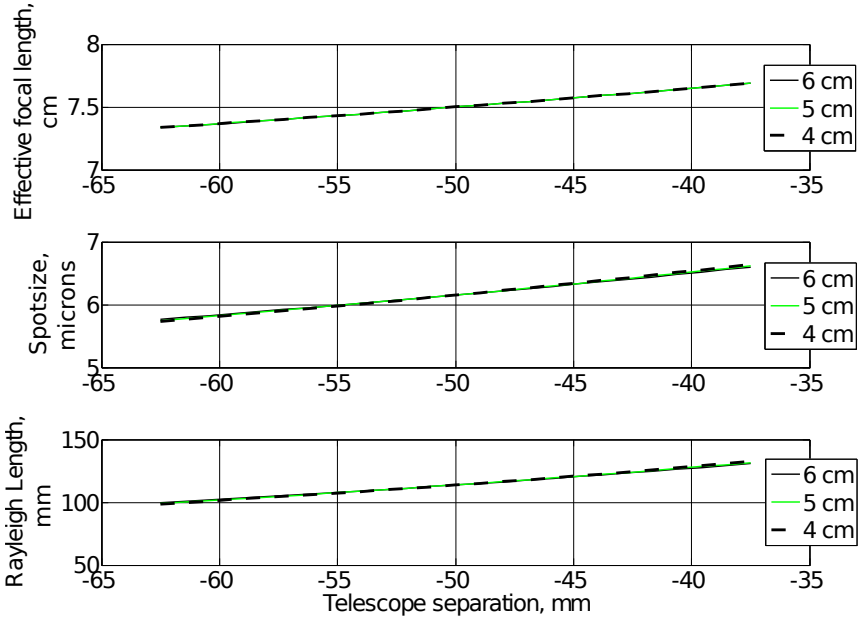

FIGURE 7.13: Simulations showing the effective focal length, spot size, and Rayleigh range for the new focal lens design as a function of telescope separation (see text for details). The legend refers to the separation between the telescope and the focusing lens.

Additionally, the comparison with other fibre CPA-based XUV sources in section 7.5 has indicated a number of avenues for long-term future work. It is evident from Ref. [22] that reducing the pulse duration for approximately the same energy benefits the generation efficiency considerably. Scaling the current output pulse energy of the fibre CPA system (as discussed in chapter 4) would allow for nonlinear compression to be used, thereby improving the XUV generation efficiency. This however, comes at the cost of increased system complexity. A more simple route to improving the XUV flux may be to follow the example outlined in Ref. [135], where gas pressures exceeding 8 bar were used to better overcome the effect of the Gouy shift on the phasematching when using a tight focus. This method could not be used with the test-bed vacuum system due to the limited pumping speed of the vacuum equipment available, but may be included trivially by using higher capacity vacuum pumps.

7.7 Summary

The fibre CPA system was demonstrated as a high-harmonic source with state of the art conversion efficiency using a xenon-filled gas cell. This was achieved in part due to the diffraction limited beam quality and good stability of the infrared source, but also through an optimized focal arrangement which maximized the number of atoms involved in the HHG process by maximizing the volume over which tunnel ionization dominated. The XUV signal was optimized using an aluminium-coated photodiode as a monitor while the focal position in the gas cell and xenon pressure were altered iteratively. The best phasematching was found when the focus was position approximately 0.5 mm before the gas cell when it was filled with 60 mbar of xenon. The generated XUV was characterized using the single exposure method outlined in chapter 6, and had a peak wavelength of 45.5 nm and radii of curvature measuring 11.3 and 11.4 cm in the x- and y-directions, respectively. The spatial intensity distribution of the five most intense harmonics (wavelengths 55–38.7 nm) was also shown. The cutoff wavelength was 27 nm, indicating that the generation was limited by the phasematching condition as the theoretical cutoff for the driving intensity of $1.8{\times}10^{14}$ W/cm^2 is approximately 21 nm.

The calculated photon flux of 0.5–1 $\times$ 10^{11} ph/s was used alongside the spectrum to estimate an average power of 400 nW of XUV. This gives a conversion efficiency of approximately 240 nW/W, which is double that reported with equivalent systems (120 nW/W) reported in the literature. It was suggested that by using a coherently combined array of Yb-doped flexible fibres as the final amplifier followed by both a linear and nonlinear compression stage it would be possible to scale the generation efficiency further, as values of 3.68 μW/W have been reported when incorporating these additional methods into the CPA architecture. Further improvements to the vacuum chamber were discussed which would allow for the gas pressure to be better optimized for the tight focusing regime, as it has been shown that gas cell pressures of approximately 1 bar are optimal for HHG using small focal spot sizes.

Part III

Supercontinuum in the all-normal dispersion regime

Chapter 8

Decoherence of supercontinuum in ANDi fibre due to Raman gain

8.1 Introduction

Low cost sources of supercontinuum light are useful for applications in metrology and carrier-envelope phase locking [136]. The invention of small-core PCF was important for the development of such sources because low energy pulses could be used to generate bandwidths of more than an octave, and this was one of the key technologies supporting the Nobel prize winning team who pioneered frequency comb metrology [137]. A high degree of coherence is required for these applications which typically necessitates the use of pump pulse durations below the 50 fs region when pumping in the anomalous dispersion regime ($\beta_2 < 0$), as is traditionally the case when broad bandwidths are required. This ensures that the gain bandwidth for modulation instability (MI) is coherently seeded by the pulse spectral wings. When this is the case, the supercontinuum generation (SCG) process is driven initially by the soliton fission process, before the soliton self-frequency shifting process continues to broaden the spectrum. If the MI bandwidth ($\sim$0.1 THz) exceeds that of the pump pulse the process is seeded by quantum noise which leads to incoherent spectral broadening [60], as is the case for longer pump pulses. The need for such short pulses means that the sources are typically more complex.

An alternative is offered by the inherently coherent broadening in all-normal dispersion (ANDi, $\beta_2 > 0$) PCF. It has been shown that the properties of supercontinuum generation (SCG) in the ANDi regime are dependent only on the peak power of the pump pulses, and are independent of the input pulse duration [138]. The seed laser cost can therefore be reduced. The coherent nonlinear pulse propagation dynamics which give rise to spectral broadening in this dispersion regime are well understood, and pulses with

a single-peaked, smooth temporal profile and a spectral bandwidth of more than an octave can be produced through optical wavebreaking [139]. Hence, picosecond, higher energy pump pulses from, for example, a parabolic amplifier could be used without the need for a compressor or a sub-100 fs oscillator to produce a highly coherent broadband source.

The onset of Raman scattering in fibres operated in the normal dispersion regime has been observed for nanosecond pump pulses, where the narrow bandwidth and high peak power result in a nonlinear length which is significantly shorter than the dispersion length ($L_{\mathrm{NL}} \ll L_{\mathrm{D}}$). Under these conditions long fibres are used and this allows Raman scattering to dominate over SPM-induced broadening. This is in part due to the reduced gradient of the pump pulse intensity envelope and increased influence of the Raman convolution integral in equation 2.19 for a given peak power. It is also caused by the difference in the way that the two effects are scaled with propagation distance. Spectral broadening through SPM scales linearly, and is dependent on $P_0\gamma z$, whereas Raman is a stimulated amplification process determined by the relation $\exp(g_R z)$, as shown in equation 2.22. The Raman effect is therefore favoured by longer propagation distances for a given peak power when longer pump pulses are used.

Motivated to produce coherent octave spanning supercontinua directly from a parabolic amplifier an investigation into novel low energy ANDi SCG sources pumped by ∼1 ps pulses was started by Dr. Alexander Heidt and Dr. Jonathan Price, and I was involved because of my development of a suitable pump laser for the work. Unexpectedly, cascaded Raman scattering was observed, producing similar spectra to those reported for the nanosecond case. As no previous reports had been made for picosecond pump pulses at this time, the focus of the work was shifted towards an investigation into the onset of Raman scattering and how this process effects the coherence properties of the fully developed supercontinuum spectra.

Since this work was started a theory paper reporting octave spanning SCG in ANDi fibre with picosecond pump pulses has been published [140]. Decoherence was observed in the simulations, but a description of the decoherence mechanism was restricted to the increased Raman gain for the ∼10 cm fibre lengths required for the largest bandwidths. Hence there has been no previous thorough experimentally verified exploration of Raman scattering for picosecond and femtosecond pump pulse durations in ANDi fibres. The simulations and experiments presented in this chapter provide the first conclusive analysis of the nonlinear dynamics which lead to Raman scattering and the corresponding degradation in coherence in this dispersion regime. All of the simulations and experimental data shown are my own work, while initial experiments and simulations involved Dr. Heidt and Dr. Price.

This chapter is structured as follows. Section 8.2 presents simulated data to introduce optical wavebreaking when using femtosecond pump pulses and demonstrates the

effect of Raman scattering on the spectral broadening process when using picosecond pump pulses. The resulting spectral coherence for both cases is examined. Section 8.3 introduces the experimental and data analysis procedures used for two ANDi SCG experiments performed as part of this investigation. The experimental results are discussed in subsections 8.4.1 and 8.4.2. The chapter is then concluded in section 8.5.

8.2 Simulation

In this section, broadening mechanisms in the ANDi regime are explored numerically. The impact that the effects of wavebreaking and Raman scattering have on the shot-to-shot spectral phase stability are demonstrated using as a quantitative measure the complex first-order degree of coherence as defined in equation 2.31. This is determined by the sensitivity of the broadening to the initial conditions as set by input quantum noise (included using the one photon per mode approach and the Raman ASE term as defined in subsection 2.4.3). The Taylor coefficients which describe the fibre dispersion profile used in all of the simulations are given in table 8.1 (taken from ref. [141]). The fibre MFD was set to 2.2 μm, giving a nonlinear parameter of $\gamma = 0.037$.

$\beta_2 = 2.259 \times 10^{-2}$ ps^2/m	$\beta_3 = -4.0444 \times 10^{-5}$ ps^3/m
$\beta_4 = 2.5464 \times 10^{-7}$ ps^4/m	$\beta_5 = -1.0273 \times 10^{-9}$ ps^5/m
$\beta_6 = 2.8644 \times 10^{-12}$ ps^6/m	$\beta_7 = 1.3131 \times 10^{-14}$ ps^7/m
$\beta_8 = -1.9999 \times 10^{-16}$ ps^8/m	$\beta_9 = 1.0332 \times 10^{-18}$ ps^9/m
$\beta_{10} = -2.6889 \times 10^{-21}$ ps^{10}/m	$\beta_{11} = 2.9639 \times 10^{-24}$ ps^{11}/m

TABLE 8.1: Taylor coefficients for the all-normal fibre dispersion profile as used in the simulations.

This section is separated into two subsections. Subsection 8.2.1 introduces spectral broadening in the ANDi regime when pumped with femtosecond pulses, and subsection 8.2.2 focusses on picosecond pump pulses. A comparison between the stability and coherence of femtosecond and picosecond pumped supercontinuum is also included in this subsection. All of the spectrograms in this section show the normalized power in grid-pixels with dimension $\Delta f = 90$ GHz, $\Delta t = 2.4$ fs.

8.2.1 Supercontinuum seeded with femtosecond pump pulses

Figure 8.1a)–d) shows the propagation of a transform limited Gaussian pulse with 250 fs duration, 6 nJ pulse energy and a central wavelength of 1055 nm through ANDi PCF in spectrogram form, simulated using the RK4IP technique (section 2.4) for four different

fibre lengths. These figures demonstrate the four main stages in the optical wavebreaking process, and will be discussed in detail following the argument presented in ref. [142].

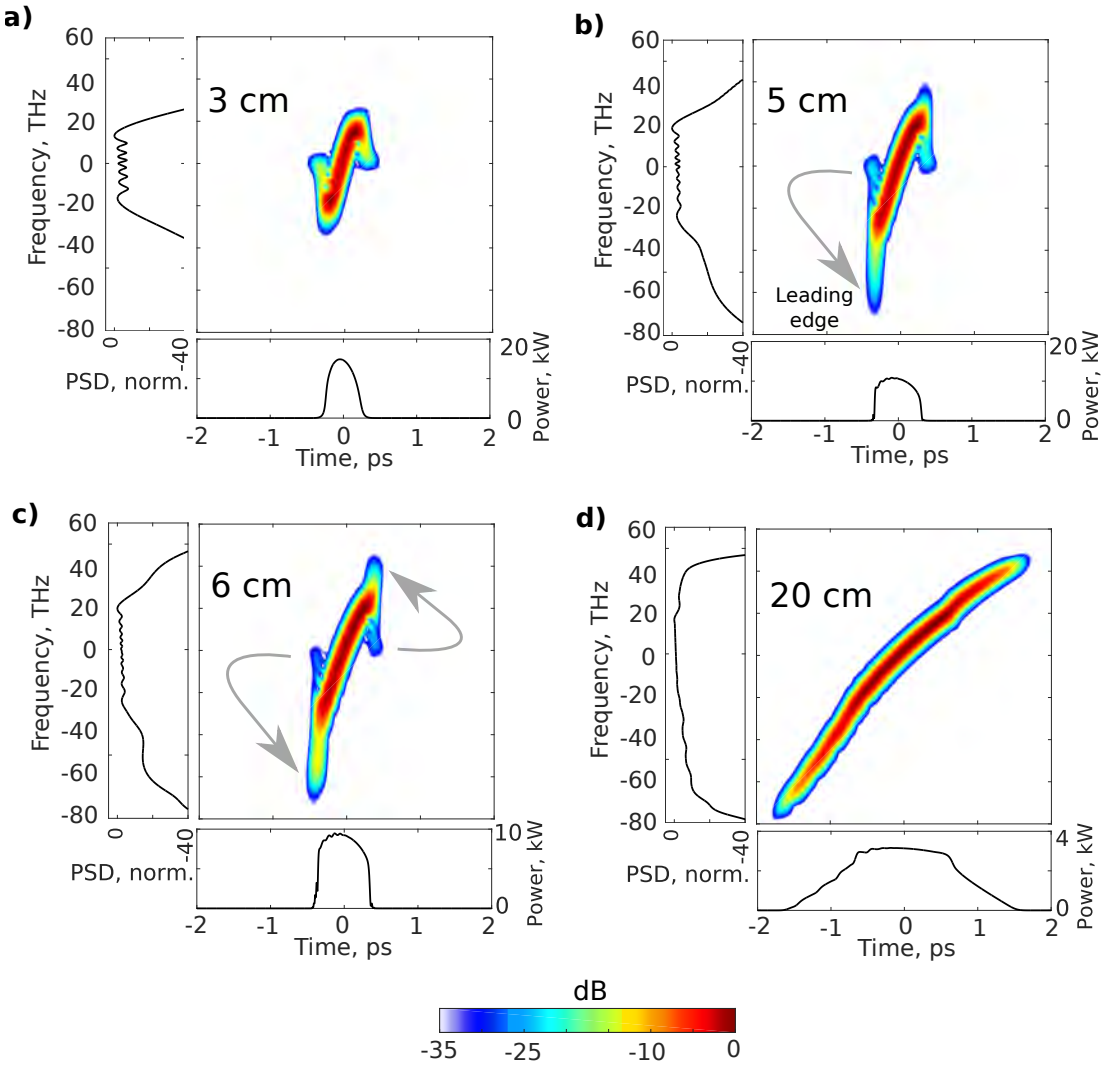

FIGURE 8.1: Spectrograms showing the simulated evolution of a 250 fs, 6 nJ Gaussian pulse as it propagates in ANDi fibre. a) Spectral broadening through SPM after 3 cm of propagation. b) and c) After 5–6 cm of propagation, wavebreaking occurs and dispersion and four wave mixing transfer energy (indicated by the arrows) to higher and lower frequencies than would be achieved by SPM alone. d) The spectral broadening is complete by 20 cm of propagation, and dispersion becomes dominant. The temporal pulse shape is shown below each spectrogram (units of kW). The spectral pulse shape is shown to the left of each spectrogram, and is normalized to the maximum value (units of dB).

After 3 cm of propagation, the spectrogram in figure 8.1a) shows the characteristic '*S*' shape produced by SPM. Dispersion in the fibre is low, so SPM is the dominant process. The leading edge of the pulse is red-shifted and the trailing edge is blue-shifted, and the spectrum on the left-hand side shows the oscillatory structure which arises due to interference of identical spectral components which are present at different temporal

positions. This forms the first step in the wavebreaking process.

The second step occurs after 5 cm of propagation where the onset of optical wavebreaking is first seen. This is governed by the interaction of both SPM and the dispersion profile of the fibre, is shown in figure 8.1b). The fibre has normal dispersion at all wavelengths, and the most red-shifted component (f≈-40 THz) created by SPM travels faster than the unshifted frequencies (f≈0 THz). At this point pulse components with different frequencies overlap in time, and this allows for the generation of new components at frequencies governed by four wave mixing, i.e., $\omega_{\mathrm{FWM}} = 2\omega_{\mathrm{pump}} - \omega_{\mathrm{seed}}$. The arrow indicates the direction of this energy transfer, and this process continues as the pulse propagates along the fibre. The original pulse leading edge is eventually completely depleted, and replaced with the further red-shifted one. The total extent of the bandwidth given by the wavebreaking process is significantly larger than what could be achieved with SPM alone.

After 6 cm of propagation, the opposite occurs for the pulse trailing edge, where the most blue-shifted light created by SPM in the centre of the trailing edge travels slower, and wavebreaking begins to occur for the blue-shifted trailing edge of the pulse. Four wave mixing occurs again and the arrows indicate energy transfer along the frequency axis, showing the generation of new blue-shifted frequency components through the four wave mixing process. This occurs even as the four wave mixing process is continuing at the leading edge (figure 8.1c)).

Once the explosive spectral broadening created by wavebreaking has occurred, dispersion acting on the broad spectrum becomes dominant. This process continues with propagation distance until smooth, continuous, and flat spectral and temporal profiles are obtained (figure 8.1d)). After 20 cm of propagation the wavebreaking process has concluded and the spectrum remains unchanged as dispersion broadens the pulse in the time domain, reducing the peak power and creating a predominantly linear chirp. Each of the new frequencies generated in the wavebreaking process is assigned a unique position in the time domain through this mechanism, and as such no modulation is seen in either the spectral or time domains. Due to this simple phase structure an external compressor can be used to create a transform limited pulse with duration as short as 1.5 optical cycles [143]. This in general cannot be achieved through SPM alone due to the complex chirp shape.

Another important point to note, as it is the reason the process of supercontinuum generation by optical wavebreaking in ANDi fibre is so useful, is that the SPM and four wave mixing processes are largely insensitive to noise fluctuations because they are all governed by the high energy dynamics associated with mixing of regions of high energy density in the spectrogram. The process is predominantly deterministic and insensitive to small fluctuations on the input and thus the complex first-order degree of coherence (equation 2.31) is close to one over the entire bandwidth.

It is interesting to note that the 250 fs pulse above is not a special case. For supercontinuum generation in fibres with anomalous dispersion the soliton fission process is strongly influenced by the precise duration, chirp, and shape of the pulse. Remarkably, it has been shown that for most pulse shapes the main parameters affecting supercontinuum generation in fibres with normal dispersion are only the peak power and bandwidth of the pulse, enabling analytic predictions of the required length of fibre for a desired bandwidth to be obtained. The analytic expression for the distance over which wavebreaking begins to occur is given as follows [144]:

$$L_{\mathrm{WB}} \approx \sqrt{L_{\mathrm{D}} L_{\mathrm{NL}}} \tag{8.1}$$

and for the simulation parameters given above, $L_{\mathrm{D}} = 2.8$ m, $L_{\mathrm{NL}} = 1.2$ mm, and $L_{\mathrm{WB}} \approx 6$ cm, in good agreement with the simulations shown in figure 8.1. To obtain the largest bandwidths the condition $L_{\mathrm{WB}} < L_{\mathrm{fibre}}$ must be met.

It may be expected that this wavebreaking dominated continuum generation can occur in a suitable length of fibre when using picosecond pulses. However, the analytic theory omits the Raman effect. This is not always important and the simulations above, which include Raman, have no evidence of Raman peaks, a result which has been repeated in numerous experimental papers [139, 143]. As shown below, the Raman gain becomes increasingly important for longer pulses.

8.2.2 Supercontinuum seeded with picosecond pump pulses

Figure 8.2 shows the spectral evolution of a 7 ps, 2.5 kW transform limited Gaussian pulse as it propagates along a 1.5 m length of the ANDi fibre. The initial spectral broadening is given by SPM, is linear in propagation distance as expected and, in contrast to the case of femtosecond pulse pumping, is small. As a result, dispersion does not become a dominant effect and the peak power of the pulse is maintained in the time domain over the total fibre length. The long pulse duration and high peak power allow for a considerable contribution from Raman scattering with increased propagation distance, and after approximately 75 cm the first Stokes wave becomes visible and undergoes an exponential increase in intensity with propagation distance. The Stokes wave lies outside the bandwidth of the main pulse and is therefore seeded by quantum noise. As the pulse continues along the fibre, higher order Stokes and anti-Stokes bands are generated at multiples of the frequency of the Raman gain peak for silica (13.2 THz).

The higher order Stokes and anti-Stokes peaks are generated by Raman scattering and degenerate four wave mixing with the pump pulse [145]. This is illustrated in figure 8.3, which shows the final pulse shape in a spectrogram representation for

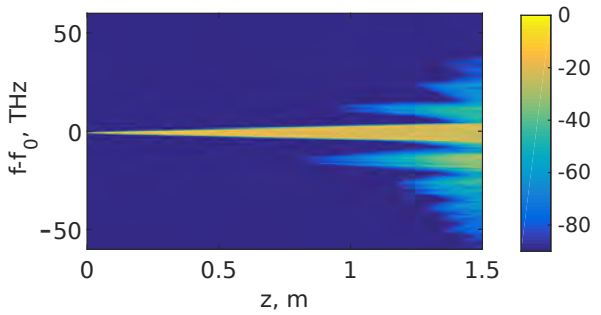

FIGURE 8.2: Spectral evolution of a 7 ps, 2.5 kW peak power transform limited Gaussian pulse during propagation along the ANDi fibre. The colourmap indicates power spectral density in dBm/nm.

the simulation shown in figure 8.2. Each order of cascaded Stokes (located at frequencies $f_{\mathrm{S,n}} = f_{\mathrm{P}} - nf_{\mathrm{R}}$, where $f_{\mathrm{R}} = 13.2$ THz, f_{P} is the pump frequency, n is an integer and $f_{\mathrm{S,n}}$ is the n^{th}-order Stokes peak) is followed by the creation of a corresponding anti-Stokes peak through degenerate four wave mixing at the new frequency of $f_{\mathrm{aS,n}} = 2f_{\mathrm{R}} - f_{\mathrm{S,n}} = f_{\mathrm{P}} + nf_{\mathrm{R}}$. These frequency bands are indicated for the 3rd anti-Stokes peak, the pump frequency, and the 1st and 3rd Stokes peak in the spectrogram.

As the frequency shifts induced by four wave mixing and Raman scattering are equal to 13.2 THz it is possible that once the first order Stokes peak has become strong enough, four wave mixing alone could be responsible for the creation of all higher order Stokes and anti-Stokes peaks. However, if the Raman gain is switched off at any point during the simulation, then spectral broadening stops, indicating that these peaks are indeed created through a combination of Raman scattering and four wave mixing.

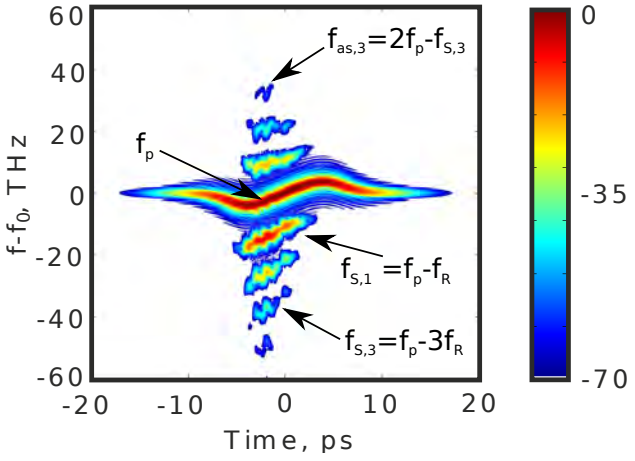

FIGURE 8.3: Simulated spectrogram of SCG output for 1.5 m of ANDi fibre pumped with a 7 ps, 2.5 kW Gaussian pulse. (colourbar is normalized and in dB).

The energy transfer between the spectral components only occurs when there is a temporal overlap of the frequency components, as was the case for wavebreaking. The ANDi fibre dispersion profile used in these simulations is relatively flat and has low

dispersion near the peak, and so the newly generated spectral components do not walk off significantly over the fibre length. This is the case for the pulse shown in figure 8.3 and the SCG process would therefore continue for an increased fibre length.

As the Raman effect amplifies quantum noise if the gain bandwidth is not self-seeded by the pulse and SPM, the coherence is destroyed as the random phase and amplitude fluctuations spread throughout the supercontinuum spectrum through four wave mixing. SPM and wavebreaking are always seeded by wavelength components within the pulse bandwidth, and are therefore coherence preserving processes. Although it is possible to generate supercontinua with broad bandwidths which are independent of pulse duration by exploiting wavebreaking and increasing the ANDi fibre length so that the condition $L_{\mathrm{WB}} \ll L_{\mathrm{fibre}}$ is maintained, the dominance of Raman scattering and the resulting spectral decoherence set a limit to the ability of this approach to produce novel and inexpensive octave-spanning supercontinuum sources suitable for time-resolved spectroscopy, metrology, and carrier-envelope phase locking.

The simulations were next extended to consider how this Raman broadening influences the shot-to-shot fluctuations. Repeated simulations with randomly generated quantum noise were run to show where the ensemble was producing almost identical results, consistent with a highly coherent process, or a wide spread of outcomes.

Figure 8.4 shows simulations of supercontinuum in 1.5 m of the ANDi fibre pumped with transform limited Gaussian pulses of 0.1, 3.5, and 7 ps duration, each with the same peak power of 2.5 kW. The output spectra for 20 individual simulations (red traces) and their ensemble average (black trace) are shown in the top row, and the complex first order degree of coherence calculated over the ensembles is given in the second row. Optical wavebreaking occurs for the 0.1 ps pulse (first column) and results in a broad, flat continuum with excellent coherence and a single-peaked temporal profile. $L_{\mathrm{WB}} = 10$ cm for these pulse conditions, which is shorter than the fibre length, so wavebreaking is expected to be the dominant broadening process. Once the wavebreaking process is completed the peak power of the pulse is <100 W, suppressing any further nonlinear spectral broadening.

For $T_{\mathrm{FWHM}} > 1$ ps the spectra become narrower as the wavebreaking process is suppressed. This is because the contribution to the phase from SPM is scaled by $1/T^2$ and so is reduced quickly as the pulse duration is increased, even if the peak power is kept the same [58]. The correspondingly narrow bandwidth therefore indicates that dispersion is not a significant effect, which prevents the frequency components from overlapping in the time domain and from undergoing the four wave mixing process. The wavebreaking length therefore extends beyond the fibre length at a value of 2.4 m. The resulting spectrum maintains the oscillations produced by SPM, and a broad incoherent Stokes peak appears at the long-wavelength side, as shown for the 3.5 ps pulse. This peak is red-shifted from the SPM-broadened spectral peak by approximately 13.2 THz,

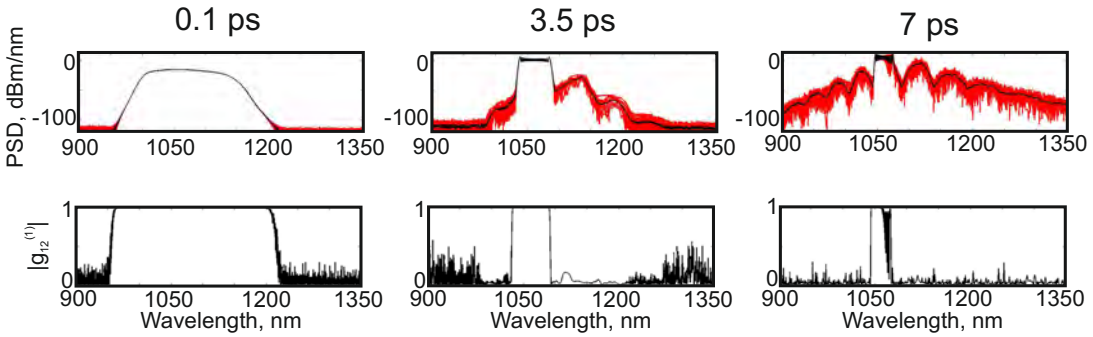

FIGURE 8.4: Simulations for the ANDi supercontinuum with transform limited pump pulses with durations between 0.1–7 ps and the same peak power of 2.5 kW. Top row: Spectra in units of dBm/nm. The red traces show 20 individual realizations, and the black traces are the ensemble average. Bottom row: complex first order degree of coherence.

commensurate with Raman scattering.

Further increasing the pump pulse duration allows the Raman effect to dominate the SCG process, and cascaded Stokes and anti-Stokes waves appear. The small SPM-broadened section of the spectrum from the 7 ps pump pulse retains some coherence, whilst the Stokes and anti-Stokes peaks exhibit large fluctuations in amplitude and phase between successive simulations because of the precise details of the one photon per mode and Raman ASE noise fluctuations. This leads to an ensemble averaged coherence of zero for the Raman spectral components.

The resulting supercontinuum dynamics are therefore governed by a competition between SPM and wavebreaking, and Raman scattering and four wave mixing. The competition is driven by the length scaling of both SPM and Raman scattering, the fibre dispersion, and the input pulse duration. Raman scattering is expected to be the dominant broadening process for pulses of a given peak power and T_{FWHM} >1 ps as SPM is suppressed by the reduced gradient of the intensity envelope. This increases the wavebreaking length beyond the fibre length, allowing for the Raman effect to dominate before wavebreaking occurs. However, if the pulse duration is decreased so that $L_{\mathrm{WB}} \ll L_{\mathrm{fibre}}$ wavebreaking causes explosive spectral broadening before the Raman effect can contribute significantly. Dispersion acting on the spectrally broadened pulse rapidly reduces the peak power, thus reducing the contribution from the Raman effect for increased propagation distance despite the increased pulse duration.

8.3 Experimental method and data analysis procedure

Motivated by the understanding of the dynamics obtained by the simulations detailed above and to show the importance of the Raman effect with long pulses, two experiments

were performed to investigate the onset of decoherence in the ANDi regime. In the first, the pulse energy was scaled using a variable attenuator before the ANDi fibre while keeping the pulse duration and bandwidth constant. Two lengths of ANDi PCF (NKT NL-1050-NEG-1) were used, measuring 1.4 and 15.4 m. The shorter length was chosen as it allowed for gradual decoherence to be observed in detail. The longer length was chosen so that complete decoherence across the whole SCG bandwidth could be observed from an initially coherent signal. The second experiment involved scaling the pulse duration while keeping the pulse energy and bandwidth constant. Only the 15.4 m length of ANDi PCF was used for this experiment. The experimental setup is described in subsection 8.3.1 and the data analysis procedure is outlined in subsection 8.3.2.

8.3.1 Experimental setup

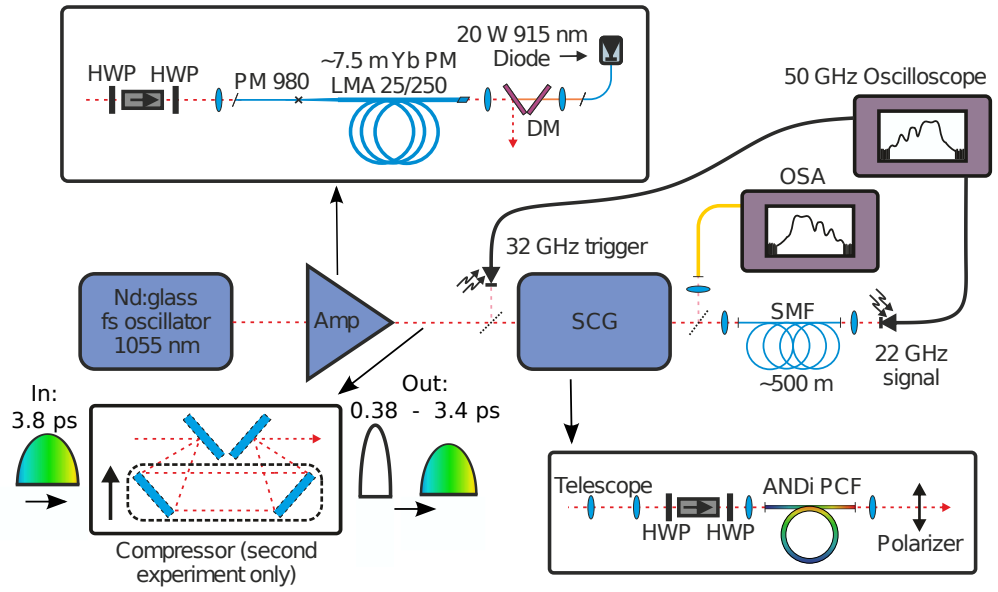

FIGURE 8.5: Schematic of the experimental setup used in the ANDi supercontinuum generation experiments. The compressor was used for the second experiment documented here, and was bypassed in the first. Care was taken to ensure that the compressor never produced a negatively chirped pulse at the output, as described in the text. DM: Dichroic mirror.

The experimental setup for both energy and duration scaling experiments is shown in figure 8.5, and allowed for Raman decoherence to be observed. A master oscillator power amplifier (MOPA) configuration was used, and an Nd:glass modelocked laser (GLX-200, Time Bandwidth) producing output pulses with a duration of 400 fs, 120 mW average power, central wavelength of 1055 nm at a repetition rate of 82 MHz seeded an amplifier constructed of 7.5 m DC polarization maintaining large mode area Yb-doped fibre (Nufern PLMA-YDF-25/250-VIII). This fibre has a core diameter of 25 μm (NA=0.06), pump cladding diameter of 250 μm (NA=0.46), and was backwards pumped by a fibre

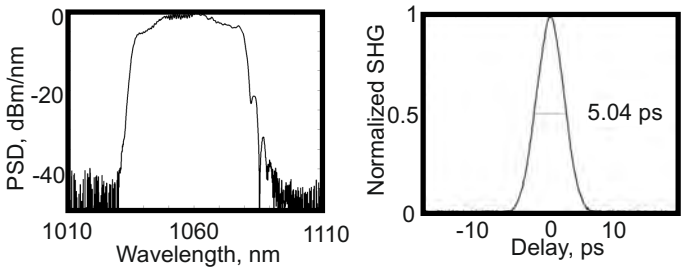

FIGURE 8.6: Spectral and autocorrelation data for the parabolic amplifier. The autocorrelation width of $\sim$ 5 ps corresponds to a pulse duration of 3.8 ps using the deconvolution factor for a parabolic pulse (1.31).

pigtailed 915 nm diode ($\sim$20 W). The input end of the fibre was tapered [146, 147, 148] and spliced to approximately 40 cm of passive single-mode fibre (Nufern PM980) to maintain fundamental mode operation, and the oscillator was isolated from the amplifier. A 0.5 mm long endcap was spliced onto the output of the amplifier to expand the mode and prevent optical damage to the fibre facet. The amplifier was operated in the parabolic regime [149], and had an output power of 4.2 W for pulses with a bandwidth of 45 nm at the -10 dB level and chirped pulse duration of 3.8 ps FWHM assuming a parabolic intensity profile, as shown in figure 8.6. The amplifier output was linearly polarized with 13 dB extinction. A telescope followed the amplifier to expand and collimate the beam, allowing for an improved launch efficiency of approximately 45% into the ANDi PCF. The measured dispersion curve for this fibre is shown in figure 8.7. A polarizing isolator positioned before this fibre prevented back reflections into the amplifier and also functioned as a variable attenuator so that the launched pulse energy could be varied without altering the spectrum or temporal profile of the seed pulses.

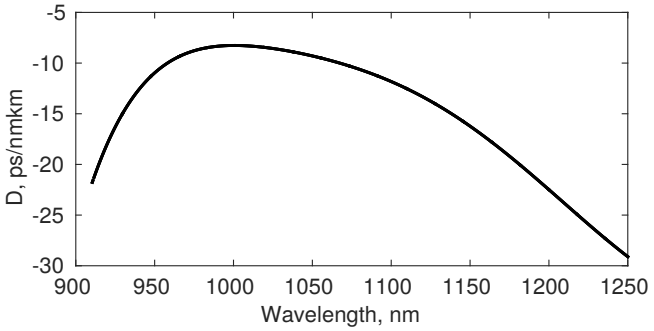

FIGURE 8.7: Measured dispersion profile for the ANDi fibre.

A half waveplate was used before the PCF to launch the pulses along the desired polarization axis of the fibre [150], and a polarizer (aligned using a rotation mount to match the angle of one of the fibre birefringence axes) was used at the fibre output to remove any light which had become depolarized in the PCF. This removed spectral modulation from the recorded data which would otherwise result from polarization mode

beating at the detector and also removed polarization instabilities [150].

The setup for the pulse duration experiment is also shown in figure 8.5 and is largely the same as that used for the pulse energy scaling experiments, with the addition of a compressor before the ANDi fibre. This allowed for different pulse durations between 380 fs and 3.4 ps to be tested. It should be noted that only the 15.4 m length of ANDi PCF was used for this experiment, and that the amplifier and compressor combination was set to provide net normal dispersion for the chirped pulses and approximately zero dispersion for the shortest pulses. This maintained a positive chirp for all pulse durations tested. A negative pulse chirp would not only lead to temporal compression within the ANDi fibre, but would also have resulted in spectral compression through SPM which would further complicate the supercontinuum dynamics [58].

Technical noise was reduced in the experiments by maintaining short beam paths and using stable mirror mounts and translation stages. Thermal drift was not observed for any of the experiments conducted as the ANDi PCF was mounted in a large aluminium V-groove which acted as a heat sink. All fluctuations in the DFT signal observed in the experimental data presented in subsections 8.4.1 and 8.4.2 are therefore attributed to the nonlinear propagation dynamics. The oscilloscope was also computer interfaced for fast data acquisition to reduce the effect of long-term drift in the MOPA output which, although not observed, would also effect the SCG dynamics. 500 single-shot spectra were saved as a data set for each SCG pump pulse energy and duration.

The dispersive Fourier transform (DFT) technique [151, 152] was used for fast and continuous recording of single shot spectral measurements. This process involves using a highly dispersive optical element after the SCG process to separate the frequency components in time so that they may be resolved by a fast photodiode and oscilloscope. The time axis of the oscilloscope trace is later interpolated onto wavelength in a process outlined in subsection 8.3.2 below. The dispersive element was formed of a 500 m length of SMF (Corning HI1060) and a 22 GHz photodiode (Agilent A3440C) was used with a 55 GHz oscilloscope (Agilent Infiniium DCA86100A) to detect the dispersed pulses. Using a 1 GHz photodiode to trigger the oscilloscope caused significant timing jitter, which clearly distorted statistical parameters in the data analysis. However, using a 32 GHz photodiode (Agilent A3440D) for the trigger minimized timing jitter, enabling accurate statistics to be calculated from the data. The trigger pulses were picked off from the main beam at the input to the PCF. Using this setup, the timing jitter was $<$3.75 ps RMS with $<$0.5 ps standard deviation, calculated using a statistics function on the oscilloscope which measured the time point corresponding to the 50% value on the signal leading edge for over 10,000 samples. The corresponding maximum wavelength domain values for this jitter are 0.11 nm and 15 pm, and were calculated once the time-to-wavelength mapping procedure was completed.

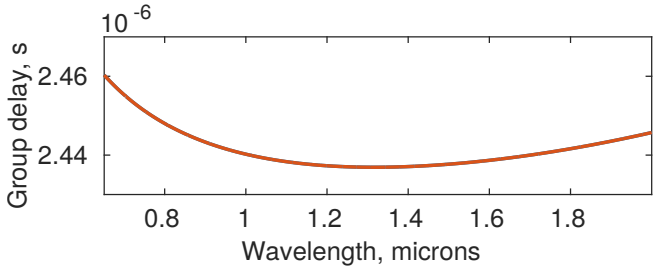

FIGURE 8.8: Group delay for 500 m of HI1060 calculated using equation 2.10 in chapter 2.

8.3.2 Data analysis procedure

The frequency to time mapping was performed by calculating the group delay of the HI1060 as a function of wavelength and interpolating the photodiode signal onto a wavelength axis using this function. The Sellmeier equation, shown in equation 8.2, was used to calculate the group delay using the method outlined in section 2.1. The Sellmeier coefficients for silica were used for the cladding [153], and an offset of 2×10^{-3} was used for the core refractive index (determined from the specification sheet). The resulting group delay for this length of HI1060 is shown in figure 8.8, and shows that the zero dispersion wavelength at approximately 1300 nm corresponds to a minimum. The DFT technique therefore imposed a technical limit to the maximum pulse energy which could be used with this setup, above which the SCG bandwidth extended beyond the zero-dispersion wavelength of HI1060 which led to a degeneracy in the wavelength to time mapping. In practice, maximum pulse energies of 13 nJ and 4 nJ were used with the 1.4 and 15.4 m ANDi PCFs, respectively.

$$n^2(\lambda) = 1 + \lambda^2 \left[\frac{B_1}{\lambda^2 - C_1} + \frac{B_2}{\lambda^2 - C_2} + \frac{B_3}{\lambda^2 - C_3} \right] \tag{8.2}$$

Interpolating the oscilloscope time-domain traces using the group delay function and then converting the frequency axis to wavelength transformed the single-shot photodiode traces into single-shot spectra. The ensemble average of the oscilloscope traces was then compared with those taken with an optical spectrum analyser to ensure that the conversion from time to wavelength was done correctly. The wavelength resolution of this setup was ∼0.3 nm [152].

Given that the photodiode records optical intensity rather than the field, the data values are real and analysis using the complex first order degree of coherence is inappropriate [60]. The shot-to-shot spectral stability was instead quantified statistically using the (second order) coefficient of variation (C_v), the (third order) skew (γ), and

the (fourth order) kurtosis (κ), defined as follows [79]:

$$\left.\begin{aligned} C_v(\lambda) &= \sigma(\lambda)/\langle I_i(\lambda)\rangle, \\ \gamma(\lambda) &= \left\langle [I_i(\lambda) - \langle I_i(\lambda)\rangle]^3 \right\rangle / \sigma^3(\lambda), \\ \kappa(\lambda) &= \left(\left\langle [I_i(\lambda) - \langle I_i(\lambda)\rangle]^4 \right\rangle / \sigma^4(\lambda) \right) - 3. \end{aligned}\right\} \tag{8.3}$$

where angular brackets denote the mean of the power spectral density taken over the ensemble, and $\sigma(\lambda) = \sqrt{\sum_{i=1}^{N} [I_i(\lambda) - \langle I(\lambda)\rangle]^2}$ is the standard deviation as a function of wavelength over an ensemble of N spectra. C_v characterizes the ratio of the noise to the signal, γ quantifies the asymmetry of the distribution about the mean value, and κ quantifies the 'peakedness' of the distribution, or the presence of long tails.

8.4 Results and discussion

8.4.1 Pulse energy scaling

The left hand side of figure 8.9 shows the 500 single-shot spectra obtained experimentally using the 1.4 m length of ANDi fibre overlaid to show the spread of results for four different pump pulse energies, each of which had the same duration of 3.8 ps. The coefficient of variation, skew, and kurtosis are given on the right of the figure for the lowest and highest pump pulse energies. The grey traces represent the individual spectra and the black trace represents the average spectrum over the ensemble.

As the pulse energy is increased from 0.5 nJ to 9.4 nJ the main spectral band between 1–1.1 μm is seen to broaden through SPM, as the spectrum becomes wider in comparison to the pump spectrum shown in figure 8.6 and a distinct Raman peak develops outside of the main pulse bandwidth. This corresponds to a reduction in relative amplitude for wavelengths between 1035 nm and 1080 nm as power is removed from this spectral band through Raman depletion. Increasing the pulse energy provides more initial broadening through SPM, which slows as the dispersion lengthens the pulse in the time domain. Due to the longer pulse duration the Raman effect becomes dominant as was seen in figure 8.4. The most severe Raman depletion is seen for the longer wavelengths of the pulse, which is predicted in the numerical simulations and shown in the experimental data at wavelengths around 1090 nm. The peak at 1140 nm develops at a wavelength separation of approximately 52 nm, which corresponds to 13.2 THz displacement from the red-shifted peak at 1090 nm, as is expected from the Raman gain spectrum.

The Raman peak data shows strong shot-to-shot fluctuations in power spectral density, which have a span of ∼18 dB for the highest pulse energy. This starts first with the appearance of the Stokes band and near the centre of the spectrum at pulse energies

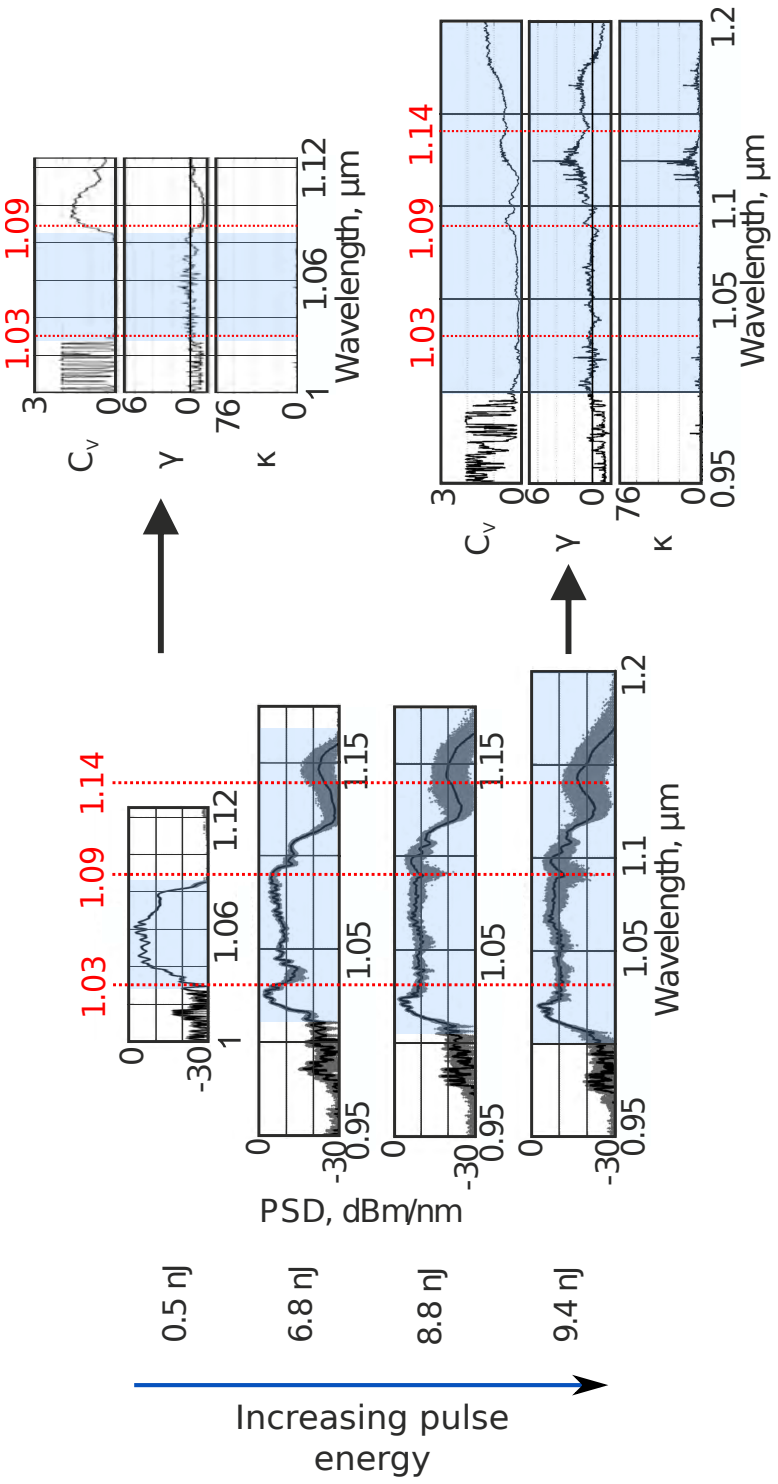

FIGURE 8.9: Left: DFT spectra for the supercontinuum generation in the 1.4 m length of ANDi fibre, pumped using 3.8 ps pulses with different energies. Right: Statistical analysis of the single-shot spectra for the lowest and highest pulse energies used. The regions where there was sufficient pulse power for the photodiode to detect are shaded blue, and all signal beyond this region is the result of electrical noise from the oscilloscope and photodiode. The red dotted lines mark the wavelengths referred to in the text, and are labelled above the plots.

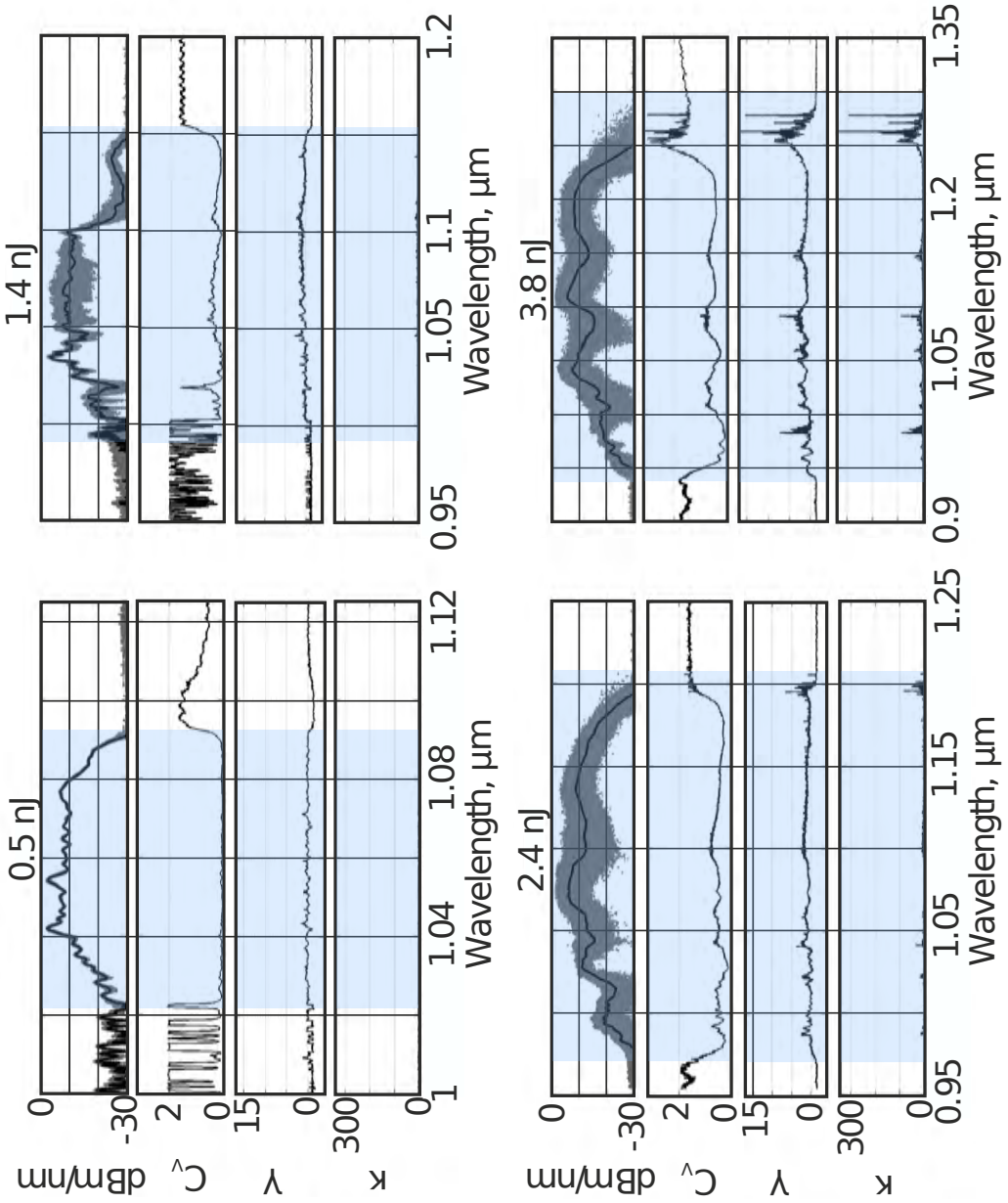

FIGURE 8.10: DFT data for the 15.4 m length of ANDi fibre, showing how the spectra vary with pump pulse energy. The wavelength axes of each plot have been scaled so that they occupy the same space on the page. Again, the blue shading indicates the region where the optical power was significant enough to register above the noise of the photodiode and oscilloscope.

between 6.8–8.8 nJ, moving to the longer wavelength end of the main spectral band for pulse energies greater than 8.8 nJ. These dynamics match those shown in the simulations in section 8.2.

The C_v for the 0.5 nJ data shows little variation within the detectable supercontinuum bandwidth. Variation beyond 1080 nm and below 1030 nm is the result of the poor signal-to-noise resulting from the low amplitude optical signal and electrical noise of the photodiode and oscilloscope at these wavelengths. This argument applies to all

out-of-band calculated statistical parameters. There is a clear difference in C_v for the 9.4 nJ data, which shows an increase in variation with wavelength, due to the increase in the spread of shot-to-shot spectral power density at each wavelength involved in the Raman scattering.

For all data sets taken the skew is net positive for increasing pulse energy, indicating that the spectral components have a long tail in their distribution about the mean spectral power density, specifically showing a large variation from the mean to higher intensities for the Raman components. This variation is most noticeable in the longer wavelength components of the spectrum. The kurtosis is also seen to increase drastically around the 1140 nm Raman peak, indicating a large increase in the peakedness of the spectral power density for this wavelength band relative to a Gaussian distribution.

Figure 8.10 shows the spectra and statistics for four pump pulse energies used with the 15.4 m length of ANDi PCF. The statistics for each pulse energy are listed below their single-shot and ensemble averaged spectra, which are shown in the top row of each figure. In comparison to the data taken using the 1.4 m length of fibre, these spectra detail the complete destruction of the spectral stability, again developing as a result of Raman scattering, and the same mechanism of decoherence is observed as the pulse energy is increased.

By observing the gradual decoherence of the signal using a short length of ANDi fibre and the complete decoherence with the longer length, the spectral characteristics are shown to be highly sensitive to quantum noise at the input. The decoherence process is the same as that seen for the simulated data.

8.4.2 Pulse duration scaling

The pulse energy used for this experiment was held constant at 2 nJ, but the duration was adjusted from 0.38–3.4 ps using a grating-based compressor before the ANDi fibre. The longer pulses have reduced peak power compared to the shorter pulses, and therefore the longer length was required to observe the onset of Raman scattering. Only the 15.4 m length of fibre was used. Figure 8.11 shows the spectra recorded for four different pulse durations. The dynamics are approximately as expected with shorter, high peak power pulses producing the broadest spectra with the least instability. The long-wavelength components of the shortest driving pulses show excellent stability and very little modulation, indicating that wavebreaking is the dominant broadening procedure. It should be noted that an equivalent stable short-wavelength band is not seen in this data set due to a sudden cut-off in photodiode response at approximately 0.95 μm. The spectral modulations at the central wavelengths for the shortest pulse duration (between 1050–1150 nm) are also the result of Raman scattering as the length of ANDi fibre used

for this experiment allowed for this effect to contribute significantly even for the shortest pulse durations. Otherwise, the spectral shape is flat with low modulation, as expected.

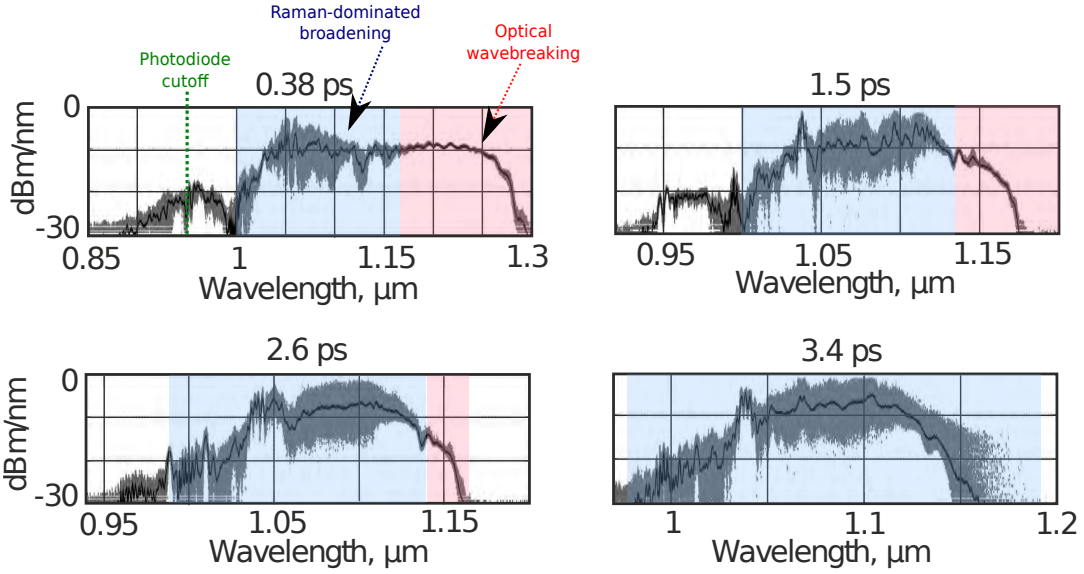

FIGURE 8.11: DFT data for the supercontinuum generation in the 15.4 m length of ANDi fibre, showing how the spectra vary with pump pulse duration. The photodiode cutoff is marked in green in the first plot. The colour-shaded areas mark the regions of the spectra which undergo Raman-dominated broadening (light blue), or optical wavebreaking (red). As the pulse duration is extended optical wavebreaking is suppressed, and Raman broadening can begin to dominate, resulting in spectral decoherence.

As the pulse duration is increased the wavebreaking length extends beyond the fibre length, suppressing this broadening process. The fluctuations in power spectral density begin to increase as Raman scattering dominates the spectral broadening, starting with the centre of the spectrum and resulting in strong modulations at the long-wavelength part of the spectrum for the 3.4 ps pump pulse. The spectral decoherence for the 3.4 ps pump pulse is almost complete, with stability at only the highest amplitude blue-shifted spectral peak. As seen with the pulse energy scaling data, the instability grows from the centre of the spectrum before extending to the longer and shorter wavelengths.

As expected, the increased duration of the SCG pump pulses is accompanied by an increase in the statistical variation parameters. This is shown in figure 8.12. The top row shows the autocorrelations of three driving pulses, and the corresponding estimated FWHM pulse durations are given above each one. The second row shows the pump pulse spectrum (blue dashed) and the mean photodiode trace (red) of the DFT ensemble spectra. The third row shows the coefficient of variation and the fourth row shows the kurtosis. As the duration is increased, both C_v and κ develop modulations at longer wavelengths. The reduced signal-to-noise due to Raman depletion in the pulse central wavelengths and Raman gain at longer wavelengths is reflected by the variation of C_v with pulse duration, with the highest noise fraction developing for the long-wavelength

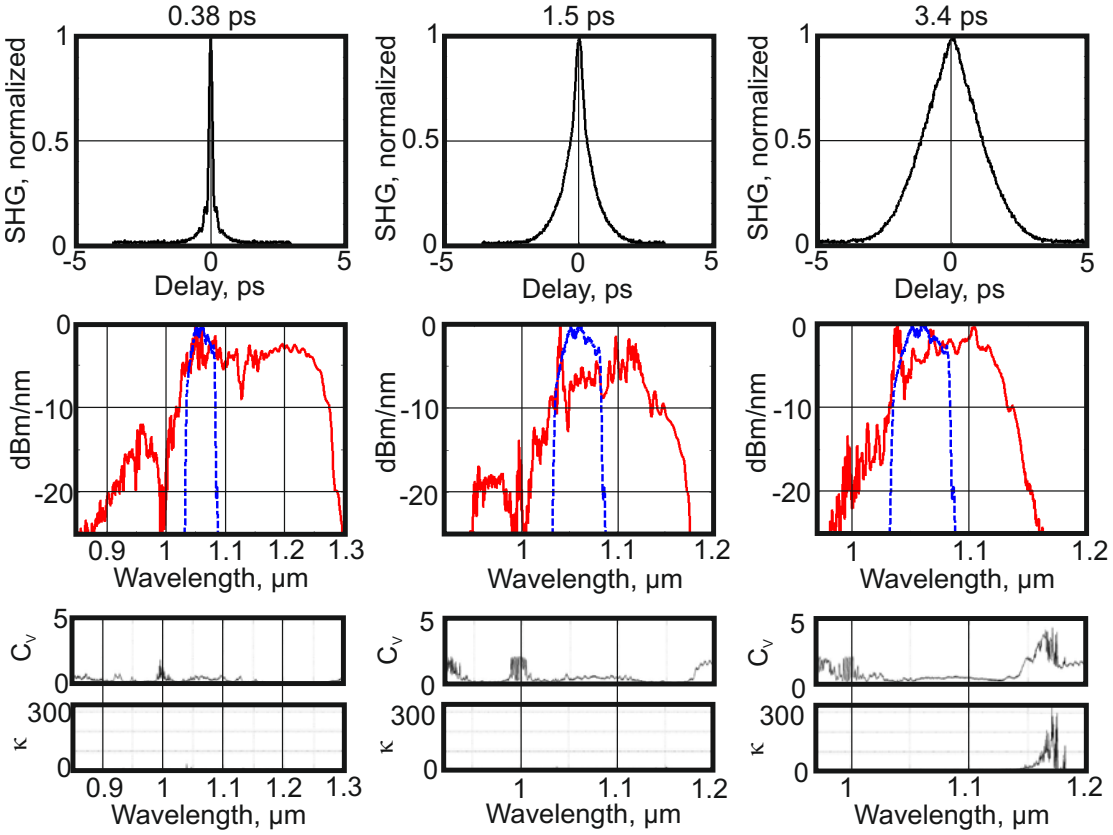

FIGURE 8.12: Experimental dispersive Fourier transform data for three pulse durations. Top row: Autocorrelation data. Middle row: ensemble average of the spectral traces (solid red lines). Bottom row: C_v and κ. The blue dashed traces in the spectral plots show the pump pulse spectrum. The vertical grid lines of the spectral and statistical data are separated by 100 nm in each column to give an impression of the spectral broadening.

components of the SCG driven by the longest pulses, where the Raman peak develops from noise. Likewise, the increased weighting of the long-wavelength tails developed through Raman scattering is indicated by κ as the pulse duration is increased.

8.5 Summary

This work represents the first demonstration of Raman dominated spectral broadening during supercontinuum generation on a microstructured fibre with all-normal dispersion profile. Simulations and experimental data clearly indicate how Raman amplified quantum noise degrades the spectral coherence. This is of practical interest for those developing the next generation of pump sources for supercontinuum generation suitable for time resolved spectroscopy and metrology measurements, both of which rely on broadband sources with excellent coherence. Propagation simulations of transform limited supercontinuum pump pulses were presented in section 8.2, and were initially

used to described the wavebreaking process, which was shown to result in broadband single-pulse signals with well-defined phase profiles and excellent coherence. Following this, simulations showed that coherence begins to degrade with the onset of Raman scattering when seeded by quantum noise. It was found that this effect is suppressed by the wavebreaking process for shorter pulse durations as the corresponding wavebreaking length is shorter than the fibre length at which Raman gain would take effect, allowing for constant and coherent seeding of wavelengths which would otherwise experience exponential gain through Raman scattering. Decoherence in ANDi fibres therefore results from competition between SPM and optical wavebreaking, and noise-seeded Raman scattering.

Experimentally obtained ensembles of single shot spectra obtained using the dispersive Fourier transform method confirm the proposed decoherence mechanism. When using picosecond seed pulses, complete destruction of the spectral stability was seen, and statistics were calculated as a function of wavelength for ensembles of 500 independently generated spectra to quantify the ratio of noise to signal, the skew, and the kurtosis over each ensemble. It was found that as noise-seeded Raman scattering becomes the dominant broadening process the statistics increase rapidly and stability in the shot-to-shot spectral power density is lost, starting with the first Stokes peak and the long-wavelength side of the pump pulse spectrum, mirroring the decoherence process seen in the simulations. Reducing the pulse duration restores the high coherence levels associated with the first reported work on ANDi fibre supercontinuum.

Part IV

Conclusions

Chapter 9

Summary and future work

The main objectives of the work presented in this thesis were to develop a stable ultrafast fibre CPA system, to demonstrate its use as a high-harmonic source, and to characterize the extreme ultraviolet which it produced. Prior to this work, a previous fibre CPA system had been developed and was capable of generating XUV, but was never characterized. This source was also not repetition rate scalable and showed occasional Q-switching instability due predominantly to a mismatch between the signal wavelength and the gain peak in the final amplifier. A new seed laser at a shorter wavelength of 1045 nm was therefore required so that the amplification chain could be optimized for stability and improved performance, as well as allowing for average power and repetition rate scaling. The first part of this thesis work was focussed on developing the seed laser for the optimized CPA system.

Due to the low noise characteristics in comparison with other cavity types a breathing-pulse ring cavity was used. The output had the correct power level in the desired wavelength band and demonstrated excellent compressibility and good amplitude noise and timing jitter. During the oscillator development, unusual cavity dynamics were also observed for this stable modelocking state, and pulses with different central wavelengths could be selected from the cavity at different positions. A detailed vectorial simulation of the cavity has fully explained this observation, and indicated that a controlled overdrive of the nonlinear polarization evolution switch acting in conjunction with the cavity dispersion was responsible. The simulated cavity was capable of self-starting from noise-like conditions after approximately 75 roundtrips, and demonstrated both single-pulse modelocking and the multi-wavelength dynamics observed in the experiment with simple changes to the polarization state of the circulated pulses. A good match between experiment and simulation was achieved for both the wavelength and time domains when simulating a single pass of the cavity fibre section with idealized input conditions. Comparison with other reports of multi-wavelength modelocking in fibre lasers indicates

that this multi-wavelength cavity design is capable of shorter pulses with broader bandwidths, but also that this detailed investigation into the cavity dynamics is the first performed for multi-wavelength modelocked fibre oscillators.

Using the single-wavelength output of the oscillator as a seed, a new fibre CPA system was constructed at the new design wavelength of 1045 nm. The existing amplifiers were rebuilt and the gain, dispersion, and nonlinearity were optimized for the best OSNR and shortest autocorrelation durations for minimal pedestal. The stretcher and compressor were realigned for the new wavelength (numerical work by Dr. Jonathan Price, lab work carried out by Dr. Price and myself), and the majority of the gain block was fiberized for improved stability. Additional improvements were found by water cooling the remaining free-space signal launches at the end of the amplifier chain. Autocorrelation and FROG data show that the majority of the 100 μJ pulse energy is concentrated in the central pulse peak, which had a flat phase profile. The peak power of 240 MW was limited by nonlinearity and the accepted maximum level of ASE from the final amplifier, rather than energy storage. The long-term and shot-to-shot stability were excellent, and the pulses had diffraction limited beam quality, indicating that the source was suitable for high-harmonic generation.

Further additions to the fibre CPA system could include adaptive pulse spectral shaping to overcome the small-scale nonlinear distortion seen at 100 μJ pulse energy, and to potentially allow for further pulse energy scaling by compensating for phase distortions from SPM. In addition, including a newer gain fibre in the final amplifier would allow the repetition rate and average power to be scaled, and would improve the current low efficiency (11%) which has come about due to photodarkening damage.

Having described the laser used to drive the high-harmonic experiments, part II included a new method for characterizing high-harmonic light suitable for use with the fibre CPA system, which produces XUV with a larger divergence than can be accommodated by existing characterization techniques. A pre-existing spatially resolved spectrometry method was adapted to include radius of curvature measurements, and involved analysing the near-field diffraction pattern produced by a grid of square apertures. Spectral content was inferred from the diffraction pattern produced by each square in the array, and the radii of curvature in the x- and y-directions were calculated from the magnification of the grid period as projected onto an x-ray CCD. The method is simple to implement and requires no alignment, samples the majority of the XUV beam thus making good use of the generated flux, has no moving parts, and is suitable for use with a wide range of XUV sources which differ in frequency content and divergence. As all spatial and spectral information can be obtained from a single exposure, this method is also suitable for single-shot use with high-flux sources.

A capillary high-harmonic source pumped by a Ti:Sapphire laser system (in the Ultrafast X-Ray Lab, Optoelectronics Research Centre) was used as a test-bed system for

the characterization method whilst it was under development. Under the assumption that the radii of curvature were equal for each harmonic detected, the spatial distributions of each harmonic were back-propagated using ASM and the XUV distributions at the exit of the capillary were calculated, demonstrating the characterization technique in a diagnostic setting. It was also noted that the technique is not generally applicable to sources which are likely to produce a poor XUV wavefront. As such, work is currently underway to extend the technique further by incorporating a Shack-Hartmann wavefront sensing algorithm [129], which will allow for single exposure analysis of the spatial and spectral profile of arbitrary beams.

The fibre CPA system was then demonstrated as a high-harmonic source using Xe as a target gas. The vacuum system which housed the focussing lens, gas cell, XUV photodiode and x-ray CCD was described. The XUV signal was optimized by iteratively adjusting gas cell pressure and the relative position of the focus and the gas cell. The tunnel ionization volume at the focus was optimized to increase the number of Xe atoms in the generation region for a given gas pressure, and was done by designing a telescopic focal arrangement. The spatially resolved intensity profiles of harmonic wavelengths 38.7–55 nm were shown as calculated by the single exposure spectrometry algorithm. The peak wavelength was 45.4 nm and the radii of curvature measured 11.3 and 11.4 cm in the x- and y-directions, respectively, as expected from the experimental parameters.

The XUV flux was estimated using the photodiode conversion efficiency and the specifications of the low-noise amplifier to convert the maximum photodiode voltage into photon number. The XUV spectrum was then normalized to this value and the relative amplitudes of each harmonic and their corresponding photon energies were taken into account to calculate an XUV integrated average power of approximately 400 nW. This corresponds to a conversion efficiency of 240 nW of XUV per Watt of input infrared, which is approximately twice as high as that shown in other reports of XUV generation with fibre CPA sources, and represents a state of the art generation efficiency for fibre CPA systems which do not use coherent combination of parallel fibre amplifiers.

It was suggested that a high free electron density in the generation volume was the limiting factor for the XUV flux due to the effect of free electron dispersion on the phase-matching constraint. Ionization rate calculations shown in chapter 5 indicate that this effect was dominant for the fibre CPA system. Including both a coherently combined final amplifier stage and nonlinear compression has been shown to drastically improve the conversion efficiency by maintaining $\sim$100 μJ pulse energy and reducing the duration to $<$30 fs, allowing for much larger generation regions to be used with reduced free electron density. Incorporating these methods to scale the diffraction limited output from the stable, single mode flexible fibre system presented in this thesis will provide a route towards a high efficiency source of XUV for applications in femto-chemistry, imaging, and lithography.

Additionally, the decoherence mechanism affecting optical signals propagating in the normal dispersion regime was explored through simulation and experiment. It was found numerically that competing wavebreaking and Raman scattering processes strongly determine the noise sensitivity and resulting coherence of optical signals depending on pulse duration, bandwidth, and noise amplitude. This was reproduced experimentally using the dispersive Fourier transform technique for a statistical analysis of ensembles of single-shot supercontinua generated by scaling the pulse energy and duration independently. It was found that spectral instability, the coefficient of variation, skew, and kurtosis increased as the Raman effect became dominant, coinciding with the suppression of SPM and wavebreaking by pumping the supercontinuum with longer pulses. This demonstration not only represents the first experimental observation of cascaded Raman scattering in the ANDi regime when pumped with picosecond and femtosecond pulses, but also constitutes the first conclusive analysis of the nonlinear dynamics which cause decoherence in normal dispersion fibres. Due to the pulse-preserving nature of the wavebreaking process, coherent octave-spanning SCG sources using all-normal dispersion fibres are useful for time-resolved spectroscopy and optical metrology, for example. This investigation into the limitations of the coherence and pulse stability is therefore of direct practical interest to members of these research communities.

Appendix A

Publications

A.1 Journal Papers

1. **J. S. Feehan**, T. J. Butcher, J. H. V. Price, W. S. Brocklesby, J. G. Frey, D. J. Richardson, "Single-mode Yb-fiber laser system producing 100 μJ, 350 fs pulses in a diffraction limited beam for high-harmonic generation", in progress

2. **J. S. Feehan**, J. H. V. Price, W. S. Brocklesby, F. Ö. Ilday, D. J. Richardson, "Multi-wavelength passively modelocked Yb-fiber oscillator producing 47 fs pulses", in progress

3. A. M. Heidt, **J. S. Feehan**, et al., "Mechanisms of supercontinuum decoherence in normal dispersion fibers", in progress

4. **J. S. Feehan**, P. N. Anderson, H. M. Watts, J. H. V. Price, P. Horak, R. S. Minns, W. S. Brocklesby, J. G. Frey, "Spatial beam profiling and spectrally resolved source reconstruction of high harmonic XUV radiation using near-field diffraction", in progress

5. L. Xu, **J. S. Feehan**, L. Shen, A. C. Peacock, D. P. Shepherd, D. J. Richardson, J. H. V. Price, "Yb-fiber amplifier pumped idler-resonant PPLN optical parametric oscillator producing 90 femtosecond pulses with high beam quality", Applied Physics B, 117(4), pp. 987-993 (2014)

6. A. M. Heidt, J. H. V. Price, C. Baskiotis, **J. S. Feehan**, Z. Li, S.-U. Alam, D. J. Richardson, "Mid-infrared ZBLAN fiber supercontinuum source using picosecond diode-pumping at 2 microns", Optics Express, 21(20), pp.24281-24287 (2013)

7. C. R. Head, H. Y. Chan, **J. S. Feehan**, D. P. Shepherd, S.-U. Alam, A. C. Tropper, J. H. V. Price, K. G. Wilcox, "Supercontinuum Generation with Gigahertz

Repetition Rate Femtosecond-Pulse Fiber-Amplified VECSELs", IEEE Photonics Technology Letters, 25(5), pp.464-467 (2013)

A.2 Conference Papers

1. **J. S. Feehan**, H. M. Watts, P. Anderson, T. J. Butcher, J. H. V. Price, R. S. Minns, P. Horak, W. S. Brocklesby, J. G. Frey, "Single exposure wavefront curvature estimation of high harmonic radiation by diffraction from a regular array", CLEO 2014 San Jose, CA, 8-13 Jun. 2014, STh3E.4

2. C. R. Head, H. Y Chan, **J. S. Feehan**, D. P. Shepherd, S.-U. Alam, A. C. Tropper, J. H. V. Price, K. G. Wilcox, "Supercontinuum Generation with Femtosecond Pulse Fibre Amplified VECSELs", SPIE Photonics West, San Francisco, 2-7 Feb. 2013, 8606-08

A.3 Summer Schools

1. **J. S. Feehan**, J. H. V. Price, W. S. Brocklesby, J. G. Frey, D. J. Richardson, "Ytterbium Fiber CPA System for High Harmonic Generation", Conference on Short Wavelength Imaging and Spectroscopy Sources (SWISS), University of Bern, 2012 (Poster Presentation)

Appendix B

Ionization rate and ion fraction calculations

B.1 ADK rate calculation

ADK is a function written in the MATLAB programming language for calculating the tunnel ionization rate of a gas as a function of the electric field strength of an optical pulse under the single active electron approximation. The function argument requires the following input variables: Ip_eV (The ionization potential of the gas species in electron Volts), Z (the charge of the atomic or ionic core, in a.u.), l (the azimuthal quantum number), m (magnetic quantum number), E_field (the driving laser field in S.I.), dt (the resolution of the time grid), and t_range (the extent of the time grid).

```
function [ADK_rate] = ADK(Ip_eV, Z, l, m, E_field,dt,t_range)
constants % Load physical constants

% E-Field:
E_real = real(E_field);
E_real = E_real./5.14220826e11; % electric field in au

% Atom/ion parameters:
Ip_Hart = Ip_eV/27.211;          % Ip in Hartrees
nstar = sqrt(Ip_Hart/Ip_eV);
lstar = nstar-1;

% Calculating the ionization rate
term1 = sqrt(3.*abs(E_real)./(pi*(2*Ip_Hart)^(3/2)));
Cnl2 = (2^(2*nstar))/(nstar*gamma(nstar+lstar+1)*gamma(nstar-lstar));
flm = ((2*l+1)*(factorial(l+m)))/(2^m * factorial(m)*(factorial(l-m)));
exponent = (2*Z/(sqrt(2*Ip_Hart)))-m-1;
term2 = Ip_Hart.*((2*(2*Ip_Hart)^(3/2))./abs(E_real)).^(exponent);
term3 = exp(-2*(2*Ip_Hart)^(3/2)./(3.*abs(E_real)));

% ADK rate equation
ADK_rate = term1.*Cnl2.*flm.*term2.*term3;
end
```

B.2 Ion fraction calculation

Below is the script used to calculate the relevant ion fractions used in the design of the fibre CPA high-harmonic source. The NIST Atomic Spectra Database was referred to for all of the quantum numbers used. The script defines a pulse with a given peak intensity before calling the ADK function in Appendix B.1.

```
clear, clc
constants

% Laser parameters
RR = 16.67e3;           % Laser rep rate
P_ave =1.7;             % Average power in Watts
spot = 5e-6;            % Spot size in m
delta_t = 330e-15;      % Pulse duration in s
lambda = 1045e-9;       % Wavelength in m
omega=2*pi*3e8/lambda; % Angular frequency, rads/s
period=lambda/3e8;      % Period, s

% Calculation parameters:
dt = 1e-5*delta_t;
t_range = -4*delta_t:dt:4*delta_t;

% Field definition
Ep = P_ave/RR;
P0 = sqrt(2/pi)*sqrt(2*log(2))*Ep/delta_t;
I0 = P0/(pi*spot^2);
field = sqrt(2*I0/(c*epsilon_0));
wave1=exp(1i*(t_range*omega));
env=exp(-2*log(2)*(t_range/delta_t).^2);
E = field.*wave1.*env;
E_real = real(E);

W_ADK = ADK(12.13,1,0,0,E,dt,t_range);
W_ADK2 = ADK(21.21,2,1,0,E,dt,t_range);

% Allocate memory
N0 = zeros(1,size(t_range,2)); % Neutral population
N1 = zeros(1,size(t_range,2)); % Singly ionized population
N2 = zeros(1,size(t_range,2)); % Doubly ionized population

% Initial conditions
N0(1) = 1; % 100% of initial population in the ground state
N1(1) = 0; % 0% of the initial population in singly ionized state
N2(1) = 0; % 0% of the initial population in doubly ionized state

% Euler integration
for ii = 2:length(t_range)
   N0(ii) = N0(ii-1)- N0(ii-1)*dt*1e15*(W_ADK(ii-1));
   N1(ii) = 1 - N0(ii-1) - N2(ii-1);
   N2(ii) = N2(ii-1) + N1(ii-1)*dt*1e15*W_ADK2(ii-1);
end
```

Appendix C

Oscillator noise: D. von der Linde analysis

This Appendix introduces the noise analysis used for to calculate the timing and amplitude fluctuations in the output from the multi-wavelength oscillator in chapter 3. For a more detailed anaylsis, see ref. [86].

The output intensity of a perfectly modelocked laser, F_0, may be expressed as the summation of an infinite number of identical pulses, $f(t)$, separated a multiple n of the roundtrip time, T:

$$F_0(t) = \sum_{n=0}^{\infty} f(t + nT) \tag{C.1}$$

By introducing randomly generated amplitude and temporal noise terms ($A(t)$ and $B(t)$, respectively) and making the approximation that $f(t_n + \Delta t_n) \approx f(t_n) + \dot{f}(t_n)\Delta t_n$, one can write:

$$F(t) = F_0(t) + F_0(t)A(t) + \dot{F}_0(t)TB(t) \tag{C.2}$$

where $TB(t) = \Delta t_n$. The power spectral density of the laser may then be retrieved by taking the Fourier transform of the autocorrelation function to give:

$$P_f(\omega) = (\Delta\omega)^2 |f(\omega)|^2 \sum_{n=0}^{\infty} \Big[\delta(\omega_n) + P_A(\omega_n) + (2\pi n)^2 P_B(\omega_n)\Big] \tag{C.3}$$

where P_A and P_A are the power spectra of $A(t)$ and $B(t)$, respectively. $\Delta\omega = 2\pi f_r$ is the angular roundtrip frequency, and determines the spacing between the frequency bands of the spectrum. $f(\omega)$ is the Fourier transform of the amplitude profile of the ideal pulses, and n is an integer running from minus to plus infinity.

Equation C.3 therefore represents the summation of individual identical frequency bands, separated by the roundtrip frequency of the cavity and individually modified by

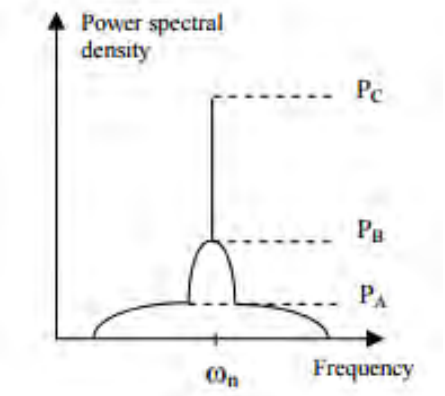

FIGURE C.1: Effect of amplitude (P_A) and timing (P_B) jitter on the n^{th} RF harmonic of the pulse train from a modelocked laser.

randomly generated functions corresponding to the power spectra of the amplitude and temporal noise terms of the non-ideal modelocked laser as determined by functions A and B. From this equation, it is seen that the timing jitter term is proportional to the square of the harmonic number, n. This allows for the amplitude noise and temporal jitter terms to be distinguished from one-another.

Figure C.1 (adapted from ref. [154]) demonstrates the effect that the amplitude noise and temporal jitter has on the spectrum of the n^{th} harmonic. The root mean square (RMS) intensity fluctuations and temporal jitter may be calculated using the following:

$$\left(\frac{\Delta E}{E}\right)^2 = \int_{-\infty}^{\infty} P_A(\omega) d\omega \tag{C.4}$$

$$\left(\frac{\Delta t}{T}\right)^2 = \int_{-\infty}^{\infty} P_B(\omega) d\omega \tag{C.5}$$

These integrals may be approximated by taking the product of the FWHM peak width and the maximum power in the n^{th} harmonic to give:

$$\int_{-\infty}^{\infty} P(\omega) d\omega \approx 2\pi \Delta f P(\omega_n) \tag{C.6}$$

If Δf_{res} is the resolution bandwidth of the RF analyser in use, then the following may be used for the amplitude noise:

$$\frac{\Delta E}{E} = \sqrt{\frac{P_A}{P_C}\bigg|_{n=0} \frac{\Delta f_A}{\Delta f_{\text{res}}}} \tag{C.7}$$

The amplitude noise can be neglected when calculating the jitter term as it is significantly smaller. Therefore, the timing jitter can be calculated using the following:

$$\frac{\Delta t}{T} = \frac{1}{2\pi n} \sqrt{\frac{P_B}{P_C}\bigg|_{n} \frac{\Delta f_A}{\Delta f_{\text{res}}}} \tag{C.8}$$

Appendix D

RK4IP propagators

D.1 Scalar propagator

An example RK4IP function is given below, written in Python. The function simulates pulse propagation in optical fibre for the fundamental spatial mode, neglecting polarization effects. The function includes the CQEM adaptive step sizing algorithm to maintain a user-defined error tolerance for each longitudinal step, and operates when no gain parameters are defined. The function argument requires the following variables: inputfield (the starting field for the simulations, time domain), linearoperator (the argument for the linear operator, including dispersion, loss, and, gain), gamma (nonlinear parameter), dz (initial step size), L (fibre length), tolerance (error tolerance for CQEM feedback), omega (angular frequency vector), omega_c (central angular frequency), dt (temporal step size), fR (Raman fraction of the nonlinear polarization), Raman (Raman response function, frequency domain). In addition, five other arguments may be given to define the fibre gain profile. *args[0] is a string used to define the gain shape ('Linear', 'Quadratic', 'Lorentzian'), *args[1] is the small signal gain coefficient, *args[2] is the saturation energy, *args[3] is given by $(2\pi c/\lambda_c) - (2\pi c/\lambda_{\text{gain peak}})$ and has units of rad Hz, and *args[4] is the FWHM bandwidth of the gain profile in rad Hz. The function outputs an array with shape $(1, 2^N)$ in the frequency domain.

```
from __future__ import division
from numpy import *
from numpy.random import randn
import scipy.constants as const
import sys

def RK4IP(inputfield, linearoperator, gamma, dz, L, tol, omega, omega_c, dt, fR, Raman
    , *args):
```

```
# Define gain parameters depending on *args
if len(args)>0:
    if len(args)>=1 and len(args)<5:
        sys.exit() # Break if *args not fully defined
    elif args[0] is 'Linear':
        g=args[1]*exp(-sum(abs(inputfield)**2)*dt/args[2])
        linearoperator=linearoperator+g*1/2
    elif args[0] is 'Quadratic':
        g=args[1]*exp(-sum(abs(inputfield)**2)*dt/args[2])
        linearoperator.real=g*(0.5-((omega-args[3])**2)/(2*args[4]**2))
        linearoperator.real[linearoperator.real<0]=0
    elif args[0] is 'Lorentzian':
        g=args[1]*exp(-sum(abs(inputfield)**2)*dt/args[2])
        linearoperator=linearoperator+(g/pi)*((args[4]/2)/sqrt((omega-args[3])
**2+(args[4]/2)**2))
else: g=0

# Definitions for Raman ASE term
f_c=omega_c/(2*pi)                  # Central frequency
UH=zeros(len(Raman))                # Allocate memory
UH[(len(Raman)-1)/2:len(Raman)]=1   # Heaviside step function
kT=const.k*300                      # Thermal energy
Boltz=(exp(const.hbar*abs(omega+omega_c)/(kT))-1)**(-1)
ASE=(2*fR*const.hbar*omega_c/gamma)*abs(Raman.imag)*(Boltz+UH)

# Definitions before loop
propagedlength=0          # Setting up loop condition
uu1=inputfield            # Time domain definition
ufft=fft.fft(inputfield) # Frequency domain definition

# Begin the loop
while propagedlength<L:

    # Redefine the gain for each step
    if len(args)>0:
        linearoperator.real=linearoperator.real/g
        g=args[1]*exp(-sum(abs(uu1)**2)*dt/args[2])
        linearoperator.real=g*linearoperator.real

    # First step of CQEM
    PhotonN=(sum((abs(ufft)**2/(omega+omega_c))))

    # Raman ASE term
    ASE_term=sqrt(fft.ifft(ASE))*randn(len(Raman))

    halfstep=exp(linearoperator*dz/2)
    uip=halfstep*ufft    # Transfer to interaction picture

    # Scalar RK4IP algorithm:
```

```
        k1=1j*gamma*dz*(1+omega/omega_c)*fft.fft(uu1*(1-fR)*(abs(uu1)**2)+fR*uu1*dt*
    fft.ifft(Raman*(fft.fft(abs(uu1)**2)))+1j*uu1*ASE_term)
        k1=halfstep*k1
        uu2=fft.ifft(uip+k1/2)
        k2=1j*gamma*dz*(1+omega/omega_c)*fft.fft(uu2*(1-fR)*(abs(uu2)**2)+fR*uu2*dt*
    fft.ifft(Raman*(fft.fft(abs(uu2)**2)))+1j*uu2*ASE_term)
        uu3=fft.ifft(uip+k2/2)
        k3=1j*gamma*dz*(1+omega/omega_c)*fft.fft(uu3*(1-fR)*(abs(uu3)**2)+fR*uu3*dt*
    fft.ifft(Raman*(fft.fft(abs(uu3)**2)))+1j*uu3*ASE_term)
        uu4=fft.ifft(halfstep*(uip + k3))
        k4=1j*gamma*dz*(1+omega/omega_c)*fft.fft(uu4*(1-fR)*(abs(uu4)**2)+fR*uu4*dt*
    fft.ifft(Raman*(fft.fft(abs(uu4)**2)))+1j*uu4*ASE_term)
        uaux=halfstep*(uip+k1/6+k2/3+k3/3)+k4/6

        propagedlength=propagedlength+dz # Advance the loop condition

        # Remaining steps of CQEM and step size correction
        if len(args)==0:
            error=abs(sum((abs(uaux)**2)/(omega+omega_c))-PhotonN)/PhotonN
            if error>2*tol:
                propagedlength=propagedlength-dz
                dz=dz/2
            elif error>tol:
                ufft=uaux
                dz=dz/(2**0.2)
            elif error<0.1*tol:
                ufft=uaux
                dz=dz*(2**0.2)
            else:
                ufft=uaux
        else: ufft=uaux    # Advanced freq. domain
        uu1=fft.ifft(ufft) # Advanced time domain

    return ufft    # Output the field in the frequency domain
```

D.2 Vector propagator

RK4IP_XPM is a function similar to RK4IP but has a nonlinear operator which includes cross-phase modulation (XPM) between orthogonal polarization components propagating along the fibre. This function includes an approximation of gain dynamics in the same manner as RK4IP, as well as the adaptive step sizing when gain is not in use. Although all of the variables are assigned the same names, both inputfield (time domain) and linearoperator are expected to be arrays of shape (2, 2^N), where the first index corresponds to polarization axis and the second the frequency or time grid. The function outputs an array with shape (2, 2^N) in the frequency domain.

```
from __future__ import division
from numpy import *
from numpy.random import randn
import scipy.constants as const
import sys

def RK4IP_XPM(inputfield, linearoperator, gamma, dz, L, tol, omega, omega_c, dt, fR,
    Raman, *args):

    # Define gain parameters depending on *args
    if len(args)>0:
        if len(args)>=1 and len(args)<5:
            sys.exit() # Break if *args not fully defined
        elif args[0] is 'Linear':
            g=args[1]*exp(-sum(abs(inputfield)**2)*dt/args[2])
            linearoperator=linearoperator+g*1/2
        elif args[0] is 'Quadratic':
            g=args[1]*exp(-sum(abs(inputfield)**2)*dt/args[2])
            linearoperator.real=g*(0.5-((omega-args[3])**2)/(2*args[4]**2))
            linearoperator.real[linearoperator.real<0]=0
        elif args[0] is 'Lorentzian':
            g=args[1]*exp(-sum(abs(inputfield)**2)*dt/args[2])
            linearoperator=linearoperator+(g/pi)*((args[4]/2)/sqrt((omega-args[3])
    **2+(args[4]/2)**2))
    else: g=0

    # Definitions for Raman ASE term
    f_c=omega_c/(2*pi)                  # Central frequency
    UH=zeros(len(Raman))                # Allocate memory
    UH[(len(Raman)-1)/2:len(Raman)]=1   # Heaviside step function
    kT=const.k*300                      # Thermal energy
    Boltz=(exp(const.hbar*abs(omega+omega_c)/(kT))-1)**(-1)
    ASE=(2*fR*const.hbar*omega_c/gamma)*abs(Raman.imag)*(Boltz+UH)

    # Definitions before loop
    propagedlength=0          # Setting up loop condition
    uu1=inputfield            # Time domain definition
```

```
ufft=fft.fft(inputfield) # Frequency domain definition

# Begin the loop
while propagedlength<L:

    # Redefine the gain for each step
    if len(args)>0:
        linearoperator.real=linearoperator.real/g
        g=args[1]*exp(-sum(abs(uu1)**2)*dt/args[2])
        linearoperator.real=g*linearoperator.real

    # First step of CQEM
    PhotonN=(sum((abs(ufft)**2/(omega+omega_c))))

    # Raman ASE term
    ASE_term=sqrt(fft.ifft(ASE))*randn(len(Raman))

    halfstep=exp(linearoperator*dz/2)
    uip=halfstep*ufft  # Transfer to interaction picture

    # Vector RK4IP algorithm:
    k1=1j*gamma*dz*(1+omega/omega_c)*fft.fft(uu1*(1-fR)*(abs(uu1)**2+(2/3)*abs(uu1
[::-1,:])**2)+fR*uu1*dt*fft.ifft(Raman*(fft.fft(abs(uu1)**2)))+1j*uu1*ASE_term)
    k1=halfstep*k1
    uu2=fft.ifft(uip+k1/2)
    k2=1j*gamma*dz*(1+omega/omega_c)*fft.fft(uu2*(1-fR)*(abs(uu2)**2+(2/3)*abs(uu2
[::-1,:])**2)+fR*uu2*dt*fft.ifft(Raman*(fft.fft(abs(uu2)**2)))+1j*uu2*ASE_term)
    uu3=fft.ifft(uip+k2/2)
    k3=1j*gamma*dz*(1+omega/omega_c)*fft.fft(uu3*(1-fR)*(abs(uu3)**2+(2/3)*abs(uu3
[::-1,:])**2)+fR*uu3*dt*fft.ifft(Raman*(fft.fft(abs(uu3)**2)))+1j*uu3*ASE_term)
    uu4=fft.ifft(halfstep*(uip+k3))
    k4=1j*gamma*dz*(1+omega/omega_c)*fft.fft(uu4*(1-fR)*(abs(uu4)**2+(2/3)*abs(uu4
[::-1,:])**2)+fR*uu4*dt*fft.ifft(Raman*(fft.fft(abs(uu4)**2)))+1j*uu4*ASE_term)
    uaux=halfstep*(uip+k1/6+k2/3+k3/3)+k4/6

    propagedlength=propagedlength+dz # Advance the loop condition

    # Remaining steps of CQEM and step size correction
    if len(args)==0:
        error=abs(sum((abs(uaux)**2)/(omega+omega_c))-PhotonN)/PhotonN
        if error>2*tol:
            propagedlength=propagedlength-dz
            dz=dz/2
        elif error>tol:
            ufft=uaux
            dz=dz/(2**0.2)
        elif error<0.1*tol:
            ufft=uaux
            dz=dz*(2**0.2)
        else:
```

```
            ufft=uaux
        else: ufft=uaux     # Advanced freq. domain
        uu1=fft.ifft(ufft) # Advanced time domain

    return ufft     # Output the field in the frequency domain
```

Appendix E

The angular spectrum method

E.1 Derivation

The following includes a derivation of the angular spectrum method for simulating the near-field diffraction pattern created by monochromatic radiation scattered from an object or aperture. This method, and the MATLAB script in Appendix E.2, feature in chapter 6, which covers the single exposure approach to determining the spatial characteristics of XUV beams.

Assuming the object is illuminated with monochromatic radiation of wavelength λ, the field distribution in the plane of the grid is defined in terms of its Fourier components as:

$$U(x,y,0) = \iint_{-\infty}^{\infty} \tilde{U}(u,\nu,0) e^{i2\pi(ux+\nu y)} du d\nu \tag{E.1}$$

where u, ν are the spatial frequencies in x and y, respectively. Changing coordinates from spatial frequencies to direction cosines α and β expresses the field as a superposition of plane waves with different direction cosines:

$$U(x,y,0) = \frac{1}{\lambda^2} \int_{-a}^{a} \int_{-b}^{b} \tilde{U}\left(\frac{\alpha}{\lambda}, \frac{\beta}{\lambda}, 0\right) e^{ik(\alpha x+\beta y)} d\alpha d\beta \tag{E.2}$$

where $|a|$ and $|b|$ are the direction cosines corresponding to the plane wave components which propagate with the largest angle to the normal of the object. When simulating the diffraction, $|a|$ and $|b|$ are ultimately determined by the angular acceptance bandwidth of the screen at longitudinal position z. The field distribution at the screen is given by:

$$U(x,y,z) = \frac{1}{\lambda^2} \int_{-a}^{a} \int_{-b}^{b} \tilde{U}\left(\frac{\alpha}{\lambda}, \frac{\beta}{\lambda}, z\right) e^{ik(\alpha x+\beta y)} d\alpha d\beta \tag{E.3}$$

$\tilde{U}(\alpha/\lambda, \beta/\lambda, z)$ is unknown, but can be calculated by propagating the integrand of equation E.3 using the Helmholtz equation, $(\nabla^2 + k^2)U = 0$:

$$\frac{\partial^2 \tilde{U}}{\partial z^2} = -k^2 \tilde{U}(1 - \alpha^2 - \beta^2) \tag{E.4}$$

$$\tilde{U}\left(\frac{\alpha}{\lambda}, \frac{\beta}{\lambda}, z\right) = \tilde{U}\left(\frac{\alpha}{\lambda}, \frac{\beta}{\lambda}, 0\right) e^{-ikz\sqrt{1-\alpha^2-\beta^2}} \tag{E.5}$$

Substituting equation E.5 in the place of the integrand in equation E.3 gives the field distribution at the screen as a function of the field distribution in the plane of the object:

$$U(x, y, z) = \frac{1}{\lambda^2} \int_{-a}^{a} \int_{-b}^{b} \tilde{U}\left(\frac{\alpha}{\lambda}, \frac{\beta}{\lambda}, 0\right) e^{-ikz\sqrt{1-\alpha^2-\beta^2}} e^{ik(\alpha x + \beta y)} d\alpha d\beta \tag{E.6}$$

A MATLAB function for solving this equation is given in section E.2, and was used for all of the diffraction simulations presented in chapter 6.

E.2 ASM field distribution propagator

ASM is a function written in the MATLAB programming language for calculating two-dimensional electric field distributions after propagation over a distance, z. The function is valid for near-field propagation only. The function argument requires variables Field (the input amplitude distribution), Phase (the input transverse phase distribution), Wavelength (the wavelength of the monochromatic radiation), z (propagation distance), N (size of the Fourier grid), and x_range (the physical size of the screen).

```
function [Output_Field] = ASM(Field, Phase, Wavelength, z, N, x_range)

k = 2*pi/Wavelength; % Wavenumber
dx = x_range/(N-1);  % Spacing of the Fourier grid (m)

phi = exp(1i * k .* Phase); % Transverse phase profile

transmission = phi .* Field;

% FFT of field:
transmission = fftshift(fft2(fftshift(transmission))); % Fourier space
kX = (2 * pi /dx) * ((1:N )/N - (N/2+1)/N);            % k-space scaling
[kx, ky] = meshgrid(kX, kX);                           % k-space grid

% Phase argument for the propagation
mu2 = k^2 - (kx.^2 + ky.^2);
mu = sqrt(mu2);

% Propagation phase definition
H = exp(1i * z * mu);

% Propagation step
transmission = H .* transmission;

% Output field calculation
Output_Field = fftshift(ifft2(fftshift(transmission)));
end
```

Bibliography

[1] T. H. Maiman. "Stimulated optical radiation in ruby". *Nature*, 187:493–494, 1960.

[2] P. A. Franken, A. E. Hill, C. W. Peters, and G. Weinreich. "Generation of optical harmonics". *Physical Review Letters*, 7(1):118–120, 1961.

[3] P. H. Bucksbaum. "The future of attosecond spectroscopy". *Science*, 317(5839):766–769, 2007.

[4] X. Xie, K. Doblhoff-Dier, S. Roither, M. S. Schöffler, D. Kartashov, H. Xu, T. Rathje, G. G. Paulus, A. Baltuška, S. Gräfe, and M. Kitzler. "Attosecond-recollision-controlled selective fragmentation of polyatomic molecules". *Physical Review Letters*, 109:243001, 2012.

[5] B. Mills, C. F. Chau, E. T. F. Rogers, J. Grant-Jacob, S. L. Stebbings, M. Praeger, A. M. de Paula, C. A. Froud, R. T. Chapman, T. J. Butcher, J. J. Baumberg, W. S. Brocklesby, and J. G. Frey. "Direct measurement of the complex refractive index in the extreme ultraviolet spectral region using diffraction from a nanosphere array". *Applied Physics Letters*, 93(23):231103, 2008.

[6] H. H. Solak, C. David, J. Gobrecht, V. Golovkina, F. Cerrina, S. O. Kim, and P. F. Nealey. "Sub-50 nm period patterns with EUV interference lithography". *Microelectronic Engineering*, 68:56–62, 2003.

[7] H.-S. Kim, W. Li, S. Danylyuk, W. S. Brocklesby, M. C. Marconi, and L. Juschkin. "Fractional Talbot lithography with extreme ultraviolet light". *Optics Letters*, 39(24):6969–6972, 2014.

[8] M. D. Seaberg, D. E. Adams, E. L. Townsend, D. A. Raymondson, W. F. Schlotter, Y. Liu, C. S. Menoni, L. Rong, C. Chen, J. Miao, H. C. Kapteyn, and M. M. Murnane. "Ultrahigh 22 nm resolution coherent diffractive imaging using a desktop 13 nm high harmonic source". *Optics Express*, 19(23):22470–22479, 2011.

[9] M. Ferray, A. L'Huillier, X. F. Li, L. A. Lompré, G. Mainfray, and C. Manus. "Multiple-harmonic conversion of 1064 nm radiation in rare gases". *Journal of Physics B*, 31(21), 1988.

[10] P. Agostini and L. F. DiMauro. "The physics of attosecond light pulses". *Reports on Progress in Physics*, 67(6):813–855, 2004.

[11] N. Dudovitch, O. Simirnova, J. Levesque, Y. Mairesse, M. Y. U. Ivanov, D. M. Villeneuve, and P. B. Corkum. "Controlling the birth of attosecond light pulses". *Nature Physics*, 2:781–786, 2006.

[12] T. Pfeifer, C. Spielmann, and G. Gerber. "Femtosecond x-ray science". *Reports on Progress in Physics*, 69(2):443, 2006.

[13] R. L. Fork, C. H. Cruz, P. C. Becker, and C. V. Shank. "Compression of optical pulses to six femtoseconds by using cubic phase compensation". *Optics Letters*, 12(7):483–485, 1987.

[14] D. J. Richardson, J. Nilsson, and W. A. Clarkson. "High power fiber lasers: current status and future perspectives". *Journal of the Optical Society of America B*, 27(11):B63–B92, 2010.

[15] Y. Jeong, J. Sahu, D. N. Payne, and J. Nilsson. "Ytterbium-doped large-core fiber laser with 1.36 kW continuous-wave output power". *Optics Express*, 12(25):6088–6092, 2004.

[16] T. Eidam, J. Rothhardt, F. Stutzki, F. Jansen, S. Hädrich, H. Carstens, C. Jauregui, J. Limpert, and A. Tünnermann. "Fiber chirped-pulse amplification system emitting 3.8 GW peak power". *Optics Express*, 19(1):255–260, 2011.

[17] F. Röser, D. Schimpf, O. Schmidt, B. Ortaç, K. Rademaker, J. Limpert, and A. Tünnermann. "90 W average power 100 μJ energy femtosecond fiber chirped-pulse amplification system". *Optics Letters*, 32(15):2230–2232, 2007.

[18] F. Röser, T. Eidam, J. Rothhardt, O. Schmidt, D. N. Schimpf, J. Limpert, and A. Tünnermann. "Millijoule pulse energy high repetition rate femtosecond fiber chirped-pulse amplification system". *Optics Letters*, 32(24):3495–3497, 2007.

[19] A. Klenke, S. Breitkopf, M. Kienel, T. Gottschall, T. Eidam, S. Hädrich, J. Rothhardt, J. Limpert, and A. Tünnermann. "530 W, 1.3 mJ, four-channel coherently combined femtosecond fiber chirped-pulse amplification system". *Optics Letters*, 38(13):2283–2285, 2013.

[20] E. Seise, A. Klenke, S. Breitkopf, J. Limpert, and A. Tünnermann. "88 W 0.5 mJ femtosecond laser pulses from two coherently combined fiber amplifiers". *Optics Letters*, 36(19):3858–3860, 2011.

[21] S. Hädrich, M. Krebs, F. Tavella, A. Willner, J. Limpert, and A. Tünnermann. "Generation of μw level plateau harmonics at high repeptition rate". *Optics Express*, 20(19):19374–19383, 2011.

[22] S. Hädrich, A. Klenke, S. Demmler, A. Hoffmann, T. Gotschall, T. Eidam, M. Krebs, J. Limpert, and A. Tünnermann. "High photon flux table-top coherent extreme-ultraviolet source". *Nature Photonics*, 8:779–783, 2014.

[23] M. Zürch, J. Rothhardt, S. Hädrich, S. Demmler, M. Krebs, J. Limpert, A. Tünnermann, A. Guggenmos, U. Kleineberg, and C. Spielmann. "Real-time and sub-wavelength ultrafast coherent diffraction imaging in the extreme ultraviolet". *Scientific Reports*, 4:7356, 2014.

[24] J. Rothhardt, S. Hädrich, A. Klenke, S. Demmler, A. Hoffmann, T. Gotschall, T. Eidam, M. Krebs, J. Limpert, and A. Tünnermann. "53 W average power few-cycle fiber laser system generating soft x rays up to the water window". *Optics Letters*, 39(17):5224–5227, 2014.

[25] B. L. Henke, E. M. Gullikson, and J. C. Davis. "X-ray interactions: Photoabsorption, scattering, transmission, and reflection at E = 50-30,000 eV, Z = 1-92". *Atomic Data and Nuclear Data Tables*, 54(2):181–342, 1993.

[26] S. Hädrich, H. Carstens, J. Rothhardt, J. Limpert, and A. Tünnermann. "Multi-gigawatt ultrashort pulses at high repetition rate and average power from two-stage nonlinear compression". *Optics Express*, 19(8):1099–1101, 2011.

[27] B. Ward, C. Robin, and I. Dajani. "Origin of thermal modal instabilities in large mode area fiber amplifiers". *Optics Express*, 20(10):11407–11422, 2012.

[28] H.-J. Otto, F. Stutzki, F. Jansen, T. Eidam, C. Jauregui, J. Limpert, and A. Tünnermann. "Temporal dynamics of mode instabilities in high-power fiber lasers and amplifiers". *Optics Express*, 20(14):15710–15722, 2012.

[29] F. He. *"The development of high power fibre chirped pulse amplification systems"*. PhD thesis, University of Southampton, 2009.

[30] F. He, H. S. S. Hung, J. H. V. Price, N. K. Daga, N. Naz, J. Prawiharjo, D. C. Hanna, D. P. Shepherd, D. J. Richardson, J. W. Dawson, C. W. Siders, and C. P. Barty. "High energy femtosecond fiber chirped pulse amplification system with adaptive phase control". *Optics Express*, 16(8):5813–5821, 2008.

[31] T. J. Butcher. *"Methods for increased energy and flux in high harmonic generation"*. PhD thesis, University of Southampton, 2012.

[32] F. He, J. H. V. Price, A. Malinowski, A. Piper, M. Ibsen, D. J. Richardson, J. W. Dawson, C. W. Siders, J. A. Britten, and C. P. J. Barty. "High average power, high energy, femto-second fiber chirped pulse amplification system". In *Conference on Lasers and Electro-Optics/Quantum Electronics and Laser Science Conference and Photonic Applications Systems Technologies*, page CMEE5. Optical Society of America, 2007.

[33] A. W. Snyder and J. Love. *"Optical waveguide theory"*. Springer, 1983.

[34] J. M. Senior. *"Optical fiber communications"*. Prentice Hall (New York), 2nd edition, 1992.

[35] D. Marcuse. "Curvature loss formula for optical fibers". *Journal of the Optical Society of America*, 66(3):216–220, 1976.

[36] J. Saijonmad and D. Yevik. "Beam-propagation analysis of loss in bent optical waveguides and fibers". *Journal of the Optical Society of America*, 73(12):1785–1791, 1983.

[37] D. Marcuse. *"Light transmission optics"*. Van Nostrand Reinhold, 2nd edition, 1982.

[38] D Gloge. "Weakly guiding fibers". *Applied Optics*, 10(10):2252–8, 1971.

[39] H. M. Pask, R. J. Carman, D. C. Hanna, A. C. Tropper, C. J. Mackechnie, P. R. Barber, and J. M. Dawes. "Ytterbium-doped silica fiber lasers: Versatile sources for the 1-1.2 μm region". *IEEE Journal of Selected Topics in Quantum Electronics*, 1(1):2–13, 1993.

[40] R. Paschotta, J. Nilsson, A. C. Tropper, and D. C. Hanna. "Ytterbium-doped fiber amplifiers". *IEEE Journal of Quantum Electronics*, 33(7):1049–1056, 1997.

[41] M. J. Weber, J. E. Lynch, D. H. Blackburn, and D. J. Cronin. "Dependence of the stimulated-emission cross-section of Yb^{3+} on host glass composition". *IEEE Journal of Quantum Electronics*, 19(10):1600–1608, 1983.

[42] H. Takebe, T. Murata, and K. Morinaga. "Compositional dependence of absorption and flourescence of Yb in oxide glasses". *Journal of the American Ceramic Society*, 79(3):681–687, 1996.

[43] D. J. Richardson, J. Nilsson, and W. A. Clarkson. "High-power fiber lasers: Current status and future perspectives". *Journal of the Optical Society of America B*, 27(11):B63–B92, 2010.

[44] E. Snitzer, H. Po, R. P. Tumminelli, and F. Hakimi. "Optical fiber lasers and amplifiers", March 21 1989. US Patent 4,815,079.

[45] J. D. Kafka. "Laser diode pumped fiber lasers with pump cavity", May 9 1989. US Patent 4,829,529.

[46] R. Maurer. "Optical waveguide light source", April 30 1974. US Patent 3,808,549.

[47] E. Snitzer, H. Po, F. Hakimi, R. P. Tumminelli, and B. C. McCollum. "Double clad, offset core Nd fiber laser". In *Optical Fiber Sensors*, volume 2, page PD5. Optical Society of America, 1988.

[48] J. C. Knight, T. A. Birks, R. F. Cregan, P. S. Russell, and J. P. de Sandro. "Large mode area photonic crystal fibre". *Electronics Letters*, 34(13):1347–1348, 1998.

[49] J. Limpert, A. Liem, M. Reich, T. Schreiber, S. Nolte, H. Zellmer, A. Tünnermann, J. Broeng, A. Petersson, and C. Jakobsen. "Low-nonlinearity single-transverse-mode ytterbium-doped photonic crystal fiber amplifier". *Optics Express*, 12(7):1313–1319, 2004.

[50] N. A. Mortensen and J. R. Folkenberg. "Low-loss criterion and effective area considerations for photonic crystal fibres". *Journal of Optics A: Pure and Applied Optics*, 5(3):163–167, 2003.

[51] B. C. Stuart, M. D. Feit, A. M. Rubenchik, B. W. Shore, and M. D. Perry. "Laser-induced damage in dielectrics with nanosecond to subpicosecond pulses". *Physical Review Letters*, 74(2248), 1995.

[52] A. V. Smith and B. T. Do. "Bulk and surface damage of silica by picosecond and nanosecond pulses at 1064 nm". *Applied Optics*, 47(26):4812–4832, 2008.

[53] P. A. Temple, W. H. Lowdermilk, and Milam D. "Carbon dioxide laser polishing of fused silica surfaces for increased laser-damage resistance at 1064 nm". *Applied Optics*, 21(18), 1982.

[54] K. S. Kim, R. H. Stolen, W. A. Reed, and K. W. Quoi. "Measurement of the nonlinear index of silica-core and dispersion-shifted fibers". *Optics Letters*, 19(4):257–259, 1994.

[55] L. G. Cohen and C. Lin. "Pulse delay measurements in the zero material dispersion wavelength region for optical fibers". *Applied Optics*, 16(12):3136, 1977.

[56] A. Sugimura and K. Daikoku. "Wavelength dispersion of optical fibers directly measured by 'difference method' in the 0.8-1.6 μm range". *Review of Scientific Instruments*, 50(3):434, 1979.

[57] L. F. Mollenauer, P. V. Mamyshev, and M. J. Neubelt. "Method for facile and accurate measurement of optical fiber dispersion maps". *Optics Letters*, 21(21):1724–1726, 1996.

[58] G. P. Agrawal. *"Nonlinear fiber optics"*. Academic Press, 4th edition, 2007.

[59] D. Milam. "Review and assessment of measured values of the nonlinear refractive-index coefficient of fused silica". *Applied Optics*, 37(3):546–550, 1998.

[60] J. M. Dudley, G. Genty, and S. Coen. "Supercontinuum generation in photonic crystal fiber". *Reviews of Modern Physics*, 78(4):1135–1184, 2006.

[61] F. DeMartini, C. H. Townes, T. K. Gustafson, and P. L. Kelley. "Self-steepening of light pulses". *Physical Review*, 164(2):312, 1967.

[62] R. H. Stolen and C. Lin. "Self-phase modulation in silica optical fibers". *Physical Review A*, 17(4):1448, 1978.

[63] V. J. Matsas, W. H. Loh, and D. J. Richardson. "Self-starting, passively mode-locked Fabry-Perot fiber soliton laser using nonlinear polarization evolution". *IEEE Photonics Technology Letters*, 5(5):492–494, 1993.

[64] M. Hofer, M. E. Fermann, F. Haberl, M. H. Ober, and A. J. Schmidt. "Mode locking with cross-phase and self-phase modulation". *Optics letters*, 16(7):502–504, 1991.

[65] V. J. Matsas, D. J. Richardson, T. P. Newson, and D. N. Payne. "Characterization of a self-starting, passively mode-locked fiber ring laser that exploits nonlinear polarization evolution". *Optics Letters*, 18(5):358–360, 1993.

[66] R. H. Stolen, J. P. Gordon, W. J. Tomlinson, and H. A. Haus. "Raman response function of silica-core fibers". *Journal of the Optical Society of America B*, 6(6):1159–1166, 1989.

[67] R. G. Smith. "Optical power handling capacity of low loss optical fibers as determined by stimulated Raman and Brillouin scattering". *Applied Optics*, 11(11), 1972.

[68] A. Galvanauskas. "Mode-scalable fiber-based chirped pulse amplification systems". *IEEE Journal of Selected Topics in Quantum Electronics*, 7(4):504–517, 2001.

[69] P. D. Drummond and J. F. Corney. "Quantum noise in optical fibers. 1. Stochastic equations". *Journal of the Optical Society of America B*, 18(2):139–152, 2001.

[70] J. Hult. "A fourth-order Runge-Kutta in the interaction picture method for simulating supercontinuum generation in optical fibers". *Journal of Lightwave Technology*, 25(12):3770–3775, 2007.

[71] A. A. Rieznik, A. M. Heidt, P. G. König, V. A. Bettachini, and D. F. Grosz. "Optimum integration procedures for supercontinuum simulation". *IEEE Photonics Journal*, 4(2):552–560, 2012.

[72] A. M. Heidt. "Efficient adaptive step size method for the simulation of supercontinuum generation in optical fibers". *Journal of Lightwave Technology*, 27(18):3984–3991, 2009.

[73] R. T. Taha and M. I. Ablowitz. "Analytical and numerical aspects of certain nonlinear evolution equations. II. Numerical, nonlinear Schrödinger equation". *Journal of Computational Physics*, 55(2):203–230, 1984.

[74] A. M. Heidt. *"Novel coherent supercontinuum light sources based on all-normal dispersion fibers"*. PhD thesis, University of Stellenbosch, 2011.

[75] P. V. Mamyshev and S. V. Chernikov. "Ultrashort-pulse propagation in optical fibers". *Optics Letters*, 15(19):1076–1078, 1990.

[76] K. Blow and D. Wood. "Theoretical description of transient stimulated Raman scattering in optical fibers". *IEEE Journal of Quantum Electronics*, 25(12):2665–2673, 1989.

[77] J. M. Dudley and S. Coen. "Coherence properties of supercontinuum spectra generated in photonic crystal and tapered optical fibers". *Optics Letters*, 27(13):1180, 2002.

[78] B. Wetzel, K. J. Blow, S. K. Turitsyn, G. Millot, L. Larger, and J. M. Dudley. "Random walks and random numbers from supercontinuum generation". *Optics Express*, 20(10):11143–11152, 2012.

[79] B. Wetzel, A. Stefani, L. Larger, P. A. Lacourt, J. M. Merolla, T. Sylvestre, A. Kudlinski, A. Mussot, G. Genty, F. Dias, and J. M. Dudley. "Real-time full bandwidth measurement of spectral noise in supercontinuum generation". *Scientific Reports*, 2, 2012.

[80] K. Tamura, E. P. Ippen, H. A. Haus, and L. E. Nelson. "77 fs pulse generation from a stretched-pulse mode-locked all-fiber ring laser". *Optics Letters*, 18(13):1080–1082, 1993.

[81] J. A. Cox, A. H. Nejadmalayeri, J. Kim, and F. X. Kärtner. "Complete characterization of quantum-limited timing jitter in passively mode-locked fiber lasers". *Optics Letters*, 35(20):3522–3524, 2010.

[82] K. Tamura, H. A. Haus, and E. P. Ippen. "Self-starting additive pulse mode-locked erbium fibre ring laser". *Electronics Letters*, 28:2226–2228, 1992.

[83] X. Liu. "Hysteresis phenomena and multipulse formation of a dissipative system in a passively mode-locked fiber laser". *Physical Review A*, 81(2):023811(1)–023811(6), 2010.

[84] D. Y. Tang, L. M. Zhao, B. Zhao, and A. Q. Liu. "Mechanism of multisoliton formation and soliton energy quantization in passively mode-locked fiber lasers". *Physical Review A*, 72(4):043816, 2005.

[85] J. W. Nicholson, J. Jaspara, W. Rudolph, and F. G. Omenetto. "Full-field characterization of femtosecond pulses by spectrum and cross-correlation measurements". *Optics Letters*, 24(23):1774–1776, 1999.

[86] D. von der Linde. "Characterization of the noise in continuously mode-locked lasers". *Applied Physics B*, 39:201–217, 1986.

[87] G. P. Agrawal. "Modulation instability induced by cross-phase modulation". *Physical Review Letters*, 59:880–883, 1987.

[88] G. P. Agrawal, P. L. Baldeck, and R. R. Alfano. "Modulation instability induced by cross-phase modulation in optical fibers". *Physical Review A*, 39:3406–3413, 1989.

[89] L. Nugent-Glandorf, T. A. Johnson, Y. Kobayashi, and S. A. Diddams. "Impact of dispersion on amplitude and frequency noise in a Yb-fiber laser comb". *Optics Letters*, 36(9):1578–1580, 2011.

[90] Z-C. Luo, A-P. Luo, W-C. Xu, H-S. Yin, J-R. Liu, Q. Ye, and Z-J. Fang. "Tunable multiwavelength passively modelocked fiber ring laser using intracavity birefringence comb filter". *IEEE Photonics Journal*, 2(4):570–577, 2010.

[91] L. Yun, X. Liu, and D. Mao. "Observation of dual-wavelength dissipative solitons in a figure-eight erbium-doped fiber laser". *Optics Express*, 20(19):20992–20997, 2012.

[92] X. Liu, D. Han, Z. Sun, C. Zend, H. Lu, D. Mao, Y. Cui, and F. Wang. "Versatlie multi-wavelength ultrafast fiber laser mode-locked by carbon nanotubes". *Scientific Reports*, 3, 2013.

[93] B. E. Lemoff and C. P. J. Barty. "Quintic-phase-limited, spatially uniform expansion and recompression of ultrashort optical pulses". *Optics Letters*, 18(19):1651–1653, 1993.

[94] F. Ö. Ilday, J. Buckley, L. Kuznetsova, and F. Wise. "Generation of 36 femtosecond pulses from a ytterbium fiber laser". *Optics Express*, 11(26):3550–3554, 2003.

[95] V. Cautaerts, D. J. Richardson, R. P. Paschotta, and D. C. Hanna. "Stretched pulse Yb^{3+}:silica fibre laser". *Optics Letters*, 22(5):316–318, 1997.

[96] J. J. Koponen, R. J. Carman, H. J. Hoffman, and S. K. T. Tammela. "Measuring photodarkening from single-mode ytterbium doped silica fibers". *Optics Express*, 14(24):11539–11544, 2006.

[97] K. Osvay and I. N. Ross. "On a pulse compressor with gratings having arbitrary orientation". *Optics Communications*, 105(3–4):271–278, 1994.

[98] A. Ruehl, A. Mercinkevicius, M. E. Fermann, and I. Hartl. "Pulse delay measurements in the zero material dispersion wavelength region for optical fibers". *Optics Letters*, 35(18):3015–3017, 2010.

[99] S. Zhou, F. Wise, and D. G. Ouzounov. "Divided-pulse amplification of ultrashort pulses". *Optics letters*, 32(7):871–873, 2007.

[100] Y. Zaouter, F. Guichard, L. Daniault, M. Hanna, F. Morin, C. Hönninger, E. Mottay, F. Druon, and P. Georges. "Femtosecond fiber chirped- and divided-pulse amplification system.". *Optics letters*, 38(2):106–108, 2013.

[101] M. Nisoli, S. de Silvestri, and O. Svelto. "Generation of high energy 10 fs pulses by a new pulse compression technique". *Applied Physics Letters*, 68(20):2793–2795, 1996.

[102] F. Emaury, C. F. Dutin, C. J. Saraceno, M. Trant, H. O. Heckl, Y. Y. Wang, C. Schriber, F. Gerome, T. Südmeyer, F. Benabid, and U. Keller. "Beam delivery and pulse compression to sub-50 fs of a modelocked thin disk laser in a gas-filled kagome-type HC-PCF fiber". *Optics Express*, 21(4):4986–4994, 2013.

[103] P. B. Corkum. "Plasma perspective on strong-field multiphoton ionization". *Physical Review Letters*, 71(13):1994–1997, 1993.

[104] M. Chini, K. Zhao, and Z. Chang. "The generation, characterization and applications of broadband isolated attosecond pulses". *Nature Photonics*, 8:178–186, 2014.

[105] M. Hentschel, R. Kienberger, C. Spielmann, G. A. Reider, N. Milosevic, T. Brabec, P. Corkum, U. Heinzmann, M. Drescher, and F. Krausz. "Attosecond metrology". *Nature*, 414(6863):509–513, 2001.

[106] J. Grant-Jacob, B. Mills, T. J. Butcher, R. T. Chapman, W. S. Brocklesby, and J. G. Frey. "Gas jet structure influence on high harmonic generation". *Optics Express*, 19(10):9801–9806, 2011.

[107] J. Gant-Jacob. *"Table-top XUV nanoscope"*. PhD thesis, University of Southampton, 2011.

[108] P. N. Anderson, T. J. Butcher, P. Horak, J. G. Frey, and W. S. Brocklesby. "Experimental demonstration of a high-flux capillary based XUV source in the high ionisation regime". *Intense Field, Short Wavelength Atomic and Molecular Processes (I-SWAMP 2011)*, 2011.

[109] P. N. Anderson, P. Horak, J. G. Frey, and W. S. Brocklesby. "High-energy laser-pulse self-compression in short gas-filled fibers". *Physical Review A*, 89(1):013819, 2014.

[110] R. T. Chapman, T. J. Butcher, P. Horak, F. Poletti, J. G. Frey, and W. S. Brocklesby. "Modal effects on pump-pulse propagation in an Ar-filled capillary". *Optics Express*, 18(12):13279–13284, 2010.

[111] T. J. Butcher, P. N. Anderson, R. T. Chapman, P. Horak, J. G. Frey, and W. S. Brocklesby. "Bright extreme-ultraviolet high-order-harmonic radiation from optimized pulse compression in short hollow waveguides". *Physical Review A*, 87(4):043822, 2013.

[112] P. Balcou, P. Salieres, A. L'Huillier, and M. Lewenstein. "Generalized phase-matching conditions for high harmonics: The role of field-gradient forces". *Physical Review A*, 55(4):3204–3210, 1997.

[113] T. Pfeifer, C. Spielmann, and G. Gerber. "Femtosecond x-ray science". *Reports on Progress in Physics*, 69(2):443–505, February 2006.

[114] M. V. Ammosov, N. B. Delone, and V. P. Krainov. "Tunnel ionization of complex atoms and of atomic ions in an alternating electromagnetic field". *Journal of Experimental and Theoretical Physics*, 64(6):1191–1194, 1986.

[115] A. Naumov, A. Zheltikov, A. Fedotov, D. Sidorov-Biryukov, A. Tarasevitch, P. Zhou, and D. von der Linde. "Ionization and absorption effects in high-order harmonic generation in gas-filled hollow fibers". *Laser and Particle Beams*, 19:75–79, 2001.

[116] F. Lindner, G. G. Paulus, H. Walther, A. Baltuška, E. Goulielmakis, M. Lezius, and F. Krausz. "Gouy phase shift for few-cycle laser pulses". *Physical Review Letters*, 92:113001, 2004.

[117] T. Popmintchev, M.-C. Chen, D. Popmintchev, P. Arpin, S. Brown, S. Alisauskas, G. Andriukaitis, T. Balciunas, O. D. Mucke, A. Pugzlys, A. Baltuska, B. Shim, S. E. Schrauth, A. Gaeta, C. Hernandez-Garcia, L. Plaja, A. Becker, A. Jaron-Becker, M. M. Murnane, and H. C. Kapteyn. "Bright coherent ultrahigh harmonics in the kev x-ray regime from mid-infrared femtosecond lasers". *Science*, 336(6086):1287–1291, 2012.

[118] A. Shiner, C. Trallero-Herrero, N. Kajumba, H.-C. Bandulet, D. Comtois, F. Légaré, M. Giguère, J.-C. Kieffer, P. Corkum, and D. Villeneuve. "Wavelength scaling of high harmonic generation efficiency". *Physical Review Letters*, 103(7):073902, 2009.

[119] E. Frumker, G. G. Paulus, H. Niikura, D. M. Villeneuve, and P. B. Corkum. "Frequency-resolved high-harmonic wavefront characterization". *Optics Letters*, 34(19):3026–3028, 2009.

[120] D. T. Lloyd, K. O'Keeffe, and S. M. Hooker. "Complete spatial characterization of an optical wavefront using a variable-separation pinhole pair". *Optics letters*, 38(7):1173–1175, 2013.

[121] D. R. Austin, T. Witting, C. A. Arrell, F. Frank, A. S. Wyatt, J. P. Marangos, J. W. G. Tisch, and I. A. Walmsley. "Lateral shearing interferometry of high-harmonic wavefronts". *Optics Letters*, 36(10):1746–1748, 2011.

[122] E. Frumker, G. G. Paulus, H. Niikura, D. M. Naumov, D. M. Villeneuve, and P. B. Corkum. "Order-dependent structure of high harmonic wavefronts". *Optics Express*, 20(13):13870–13877, 2012.

[123] M. Praeger, A. M. de Paula, C. A. Froud, E. T. F. Rogers, S. L. Stebbings, W. S. Brocklesby, J. J. Baumberg, D. C. Hanna, and J. G. Frey. "Spatially resolved soft X-ray spectrometry from single-image diffraction". *Nature Physics*, 3(3):176–179, 2007.

[124] M. Praeger. *"Development and spatio-spectral mapping of a capillary high harmonic source"*. PhD thesis, University of Southampton, 2008.

[125] M. Born and E. Wolf. *"Principles of optics: Electromagnetic theory of propagation, interference and diffraction of light"*. Pergamon Press, 4th edition, 1970.

[126] E. Hecht. *"Optics"*. Addison-Wesley Longman, 3rd edition, 1998.

[127] P. N. Anderson. *"High-order harmonic generation with self-compressed femtosecond pulses."*. PhD thesis, University of Southampton, 2015.

[128] C. Valentin, J. Gautier, J.-P. Goddet, C. Hauri, T. Marchenko, E. Papalazarou, G. Rey, S. Sebban, O. Scrick, P. Zeitoun, G. Dovillaire, X. Levecq, S. Bucourt, and M. Fajardo. "High-order harmonic wave fronts generated with astigmatic infrared laser". *Journal of the Optical Society of America B*, 25(7):161–166, 2008.

[129] B. C. Platt and R. Shack. "History and principles of Shack-Hartmann wavefront sensing". *Journal of Refractive Surgery*, 17(5):S573–S577, 2001.

[130] A. Cabasse, G. Machinet, A. Dubrouil, E. Cormier, and E. Constant. "Optimization and phase matching of fiber-laser-driven high-order harmonic generation at high repetition rate". *Optics Letters*, 37(22):4618–4620, 2012.

[131] J. S. Feehan, H. M. Watts, P. N. Anderson, T. J. Butcher, J. H. V. Price, R. S. Minns, P. Horak, W. S. Brocklesby, and J. G. Frey. "Single exposure wavefront curvature estimation of high harmonic radiation by diffraction from a regular array". In *CLEO: 2014, OSA Technical Digest (online)*, 2014.

[132] R. Keenan, C. L. S. Lewis, J. S. Wark, and E. Wolfrum. "Measurements of the XUV transmission of aluminium with a soft x-ray laser". *Journal of Physics B*, 35(20):1191–1194, 2002.

[133] The center for x-ray optics: X-ray interactions with matter. `http://henke.lbl.gov/optical_constants/`. Accessed: 18/8/2015.

[134] S. Hädrich, J. Rothhardt, M. Krebs, F. Tavella, A. Willner, J. Limpert, and A. Tünnermann. "High harmonic generation by novel fiber amplifier based sources". *Optics Express*, 18(19):20242–20250, 2010.

[135] J. Rothhardt, M. Krebs, S. Hädrich, S. Demmler, J. Limpert, and A. Tünnermann. "Absorption-limited and phase-matched high harmonic generation in the tight focusing regime". *New Journal of Physics*, 16(3):033022 1–15, 2014.

[136] R. Holzwarth, T. Udem, T. W. Hänsch, J. C. Knight, W. J. Wadsworth, and P. S. J. Russell. "Optical frequency synthesizer for precision spectroscopy". *Physical Review Letters*, 85:2264–2267, 2000.

[137] D. J. Jones, S. A. Diddams, J. K. Ranka, A. Stentz, R. S. Windeler, J. L. Hall, and S. T. Cundiff. "Carrier-envelope phase control of femtosecond mode-locked lasers and direct optical frequency synthesis". *Science*, 288(5466):635–639, 2000.

[138] A. M. Heidt. "Pulse preserving flat-top supercontinuum generation in all-normal dispersion photonic crystal fibers". *Journal of the Optical Society of America B*, 27(3):550–559, 2010.

[139] A. M. Hiedt, A. Hartung, G. W. Bosman, P. Krok, E. G. Rohwer, H. Schwoerer, and H. Bartelt. "Coherent octave spanning near-infrared and visible supercontinuum generation in all-normal dispersion photonic crystal fibers". *Optics Express*, 19(4):3775–3787, 2011.

[140] P. Li, L. Shi, and Q.-H. Mao. "Supercontinuum generated in all-normal dispersion photonic crystal fibers with picosecond pump pulses". *Chinese Physics B*, 22(7):074204, 2013.

[141] L Pan, S. Lei, and M. Qing-He. "Supercontinuum generated in all-normal dispersion photonic crystal fibers with picosecond pump pulses". *Chinese Physics B*, 22(7):074204–1–074204–6, 2013.

[142] J. H.V. Price, X. Feng, A. M. Heidt, G. Brambilla, P. Horak, F. Poletti, G. Ponzo, P. Petropoulos, M. Petrovich, J. Shi, M. Ibsen, W. H. Loh, H. N. Rutt, and D. J. Richardson. "Supercontinuum generation in non-silica fibers". *Optical Fiber Technology*, 18(5):327–344, 2012.

[143] A. M. Heidt, J. Rotthardt, A. Hartung, H. Bartelt, E. G. Rohwer, J. Limpert, and A. Tünnermann. "High quality sub-two cycle pulses from compression of supercontinuum generation in all-normal dispersion photonic crystal fiber". *Optics Express*, 19(15):13873–13879, 2011.

[144] C. Finot, B. Kibler, L. Provost, and S. Wabnitz. "Beneficial impact of wavebreaking for coherent continuum formation in normally dispersive nonlinear fibers". *Journal of the Optical Society of America B*, 28(11):1938–1948, 2008.

[145] R. W. Boyd. *"Nonlinear optics"*. Academic Press, 2nd edition, 2003.

[146] J.A. Alvarez-Chavez, A.B. Grudinin, J. Nilsson, P.W. Turner, and W.A. Clarkson. "Mode selection in high power cladding pumped fibre lasers with tapered section". In *Summaries of Papers Presented at the Conference on Lasers and Electro-Optics*, pages 247–248, 1999.

[147] K. K. Chen, S-u Alam, J. H. V. Price, J. R. Hayes, D. Lin, A. Malinowski, C. Codemard, D. Ghosh, M. Pal, S. K. Bhadra, and D. J. Richardson. "Picosecond fiber mopa pumped supercontinuum source with 39 W output power". *Optics Express*, 18(6):5426–5432, 2010.

[148] K. K. Chen, J. H. V. Price, S-u Alam, J. R. Hayes, D. Lin, A. Malinowski, and D. J. Richardson. "Polarisation maintaining 100 W Yb-fiber MOPA producing μJ pulses tunable in duration from 1 to 21 ps". *Optics Express*, 18(14):14385–14394, 2010.

[149] M. E. Fermann, V. I. Kruglov, B. C. Thomsen, J. M. Dudley, and J. D. Harvey. "Self-similar propagation and amplification of parabolic pulses in optical fibers". *Physical Review Letters*, 84:6010–6013, 2000.

[150] Y. Liu, Y. Zhao, J. Lyngsø, S. You, W. L. Wilson, H. Tu, and S. A. Boppart. "Suppressing short-term polarization noise and related spectral decoherence in all-normal dispersion fiber supercontinuum generation". *Journal of Lightwave Technology*, 33(9):1814–1820, 2015.

[151] T. Jannson. "Real-time Fourier transformation in dispersive optical fibers". *Optics Letters*, 8(4):232–234, 1983.

[152] K. Goda and B. Jalali. "Dispersive fourier transformation for fast continuous single-shot measurements". *Nature Photonics*, 7(2):102–112, 2013.

[153] M. N. Polyanskiy. Refractive index database. `http://refractiveindex.info`. Accessed: 16/9/2015.

[154] J. H. V Price. *"The development of high power, pulsed fiber laser systems and their applications"*. PhD thesis, University of Southampton, 2003.